The Application of Emerging Monitoring Technologies on Very Slow Vegetated Landslides

by

Evan Deane

A thesis submitted in partial fulfillment of the requirements for the degree of

Master of Science

in

Geotechnical Engineering

Department of Civil and Environmental Engineering

University of Alberta

Abstract

Geohazard monitoring is becoming increasingly important alongside increased expectations for the protection of the public. Technological advances in the field of remote monitoring and instrumentation has allowed for an economically efficient means of data collection. Traditional methods of instrumentation have often required expensive, time consuming, and intrusive monitoring methods using permanent instrumentation, such as slope inclinometers and shape-acceleration-arrays. These traditional methods often require site access for large borehole equipment and drilling and installation crews with advanced training.

Modern technologies can collect information over large spatial extents, and forms of data which would be impossible or extremely expensive to obtain using traditional methods. In this thesis, the use of differential global positioning systems (GPS), terrestrial light detection and ranging (LiDAR) laser scanning, and unmanned aerial vehicle (UAV) photogrammetry for improving landslide monitoring is analyzed. The use of these technologies is well proven, but there are technical limitations of these technologies regarding landslide velocity and vegetation. This thesis focuses on investigating these limitations, methods in which these limitations can be overcome, and the knowledge we were able to obtain from application of these technologies to a Very Slow (As defined by Cruden and Varnes 1996), vegetated landslide.

This work is performed with the aid of a study site, called the Chin Coulee landslide, in Southern Alberta, Canada. The Chin Coulee landslide is a large deep-seated, Very Slow, vegetated landslide, and provided a challenging testbed for the study of the limitations of these modern technologies.

It was found that differential GPS systems work well in slow moving conditions, although short-term, month-to-month data sampling would be inadequate for accurately representing landslide movement. Water conditions in and around the site, including overland erosional flow, internal groundwater flow resulting in seepage along the slope, and in the case of Chin Coulee, the reservoir elevation, are relevant to landslide movement and vary throughout the year. To fully understand landslide movement, it is recommended that at the very least, a full calendar year study be performed, with 2-3 years of study often being more appropriate for

fully understanding the mechanisms which lead to instability. As only one year of monitoring was available, it is difficult to identify the true impact events have on landslide stability.

Limit equilibrium analysis shows support for reservoir drawdown decreasing landslide stability on Chin Coulee, with up to 8% reduction in factor of safety from 1.06 to 0.98 being observed during a historical critical drawdown scenario.

Application of terrestrial LiDAR to slow-moving, vegetated landslides posed several challenges, most notably the detectable limit of movement. During slow moving conditions, without extended monitoring periods, movement will often be under the detectable level of movement, referred to as level of detection (LOD). The required duration between scans depends heavily on site and scanning conditions. Scans performed on highly vegetated sites from long distances will increase the LOD. In the case of Chin Coulee, it was not possible to bring the LOD below 50 – 70 mm. Due to the slow movement rate this LOD necessitated a monitoring window of roughly 12 months.

UAV photogrammetry was used for feature tracking of erosional channels and headscarp locations for comparison to historical information collected in 1998. Identification of increased erosion channel growth and headscarp movement was possible. A novel application of photogrammetry was the creation of a 3D model based on air photos collected in 1982 following landslide initiation. Change detection using this 3D model and a current day LiDAR scan was performed to observe the evolution of the landslide over the past 36 years. This helped to support the proposed failure mechanism for the Chin Coulee landslide. UAV-based change detection was performed using two photogrammetry models of Chin Coulee. UAV photogrammetry was limited on Chin Coulee due to the inability of photography to penetrate vegetation. The achievable LOD for this change detection was calculated at roughly 90 mm. UAV photogrammetry-based change detection appeared to show exaggerated movement in some regions, suggesting model inaccuracy.

Identification of the limitations of these modern technologies is an important step for adoption into the field of geotechnical engineering. Due to these limitations these technologies are not yet suitable for all conditions and purposes but provide strong monitoring options when viable.

Acknowledgments

I'd like to extend a thank you to my supervisors Dr. Michael Hendry and Dr. Renato Macciotta for all their support and constructive feedback throughout my thesis research. Everyone in the Railway Ground Hazard Research Program, Canadian Rail Research Laboratory, and Geotechnical Lab (Lucas Duerksen) at the University of Alberta in some way helped with the creation of this thesis, and I am grateful for all of you.

I would also like to acknowledge everyone who directly helped with my field work:

- Adam Woods, from the University of Alberta. You are not just my colleague, and fellow Master of Science student, you are a true friend. You made the long drives out to site considerably better.
- Jorge Rodriguez, from the University of Alberta. You are an amazing resource. Probably half of the knowledge I obtained during this research came from you. I can't express how grateful I am, I consider you an honorary advisor.
- Hasmik Manandyan, from the University of Alberta. Your help with setting up the Geocube system was so appreciated, as well as our chats on campus about the struggles of being a student.
- Hanh Hong, from Klohn Crippen Berger. Thank you for your help setting up the Geocube system and monitoring it while you worked at Klohn Crippen Berger.
- Chris Grapel, from Klohn Crippen Berger. Thank you for providing the opportunity to work on this project, without you, there truly wouldn't have been this research. I'd also like to thank you for your writing (and life) advice.
- Roger Skirrow, from Alberta Transportation. Among others from Alberta Transportation who humored my numerous requests for historical road construction documentation, thank you.
- Everyone else who helped me along the way. If I listed everyone, I'd run out of room on this page but know that I am grateful.

Finally, I'd like to thank my friends and family who supported me through the good times and the (inevitable) bad times during my research. Thank you.

Table of Contents

Abstract ..... **ii**

Acknowledgments ..... **iv**

Table of Contents ..... **v**

List of Tables ..... **ix**

List of Figures ..... **x**

Glossary of Terms ..... **xv**

1.0 Introduction **1**

1.1 Research Objectives 3

1.2 Research Methodology 4

1.3 Expected Contribution 4

2.0 Literature Review **6**

2.1 Use of Differential GPS in Landslide Monitoring 6

2.1.1 Differential GPS Accuracy *9*

2.1.2 Differential GPS Combined Systems *9*

2.2 Use of LiDAR in Landslide Monitoring 11

2.2.1 LiDAR Data Density *13*

2.2.2 LiDAR and Vegetation *14*

2.3 Use of UAV in Landslide Monitoring 15

2.3.1 UAV Flight Parameters and Error *17*

2.3.2 UAV Ground Control Points *18*

2.3.3 UAV Landslide Monitoring *18*

2.4 Analysis of Point Clouds for Change Detection 20

2.5 10-Mile Slide 22

3.0 The Chin Coulee Landslide 24

3.1 Location 24

3.2 Landslide Characteristics 25

3.3 Geology of the Area 27

3.4 Material Properties 28

3.5 Climate and Groundwater 30

3.6 Chin Coulee History 32

4.0 Use of Differential GPS at the Chin Coulee Landslide 35

4.1 Geocube System Description 35

4.2 GPS System Site Deployment 35

4.2.1 Installation Methodology 36

4.2.2 Connectivity 39

4.3 Differential GPS Data Processing 39

4.3.1 Methods and Software 39

4.3.2 Results Samples 41

4.4 Differential GPS Advantages and Limitations 44

4.4.1 Differential GPS Noise Issues 44

4.4.2 Differential GPS Installation Method Observations and Recommendations 53

4.4.3 Minimum Campaign Duration for Differential GPS 54

4.5 Differential GPS – Summary of Use on Very Slow, Vegetated Landslides 56

5.0 Use of TLS LiDAR at the Chin Coulee Landslide 58

5.1 LiDAR System Description 58

5.2 LiDAR System Site Deployment 59

5.3 LiDAR Data Processing 61

5.3.1 Methods and Software 61

5.3.2 Results 62

5.4 TLS LiDAR Advantages and Limitations 65

5.4.1 LiDAR Level of Detection Issues 65

5.4.2 LiDAR Bare Earth Model Generation Issues in Vegetated Conditions 66

5.5 LiDAR – Summary of Use on Very Slow, Vegetated Landslides 67

6.0 Use of Historical Air Photos and UAV Photogrammetry at the Chin Coulee Landslide . 69

6.1 Historical Air Photo Photogrammetry 69

6.1.1 Air Photo Photogrammetry Methods and Results Sample 70

6.1.2 Air Photo Photogrammetry Advantages and Limitations 71

6.1.3 Air Photo Photogrammetry Interpretation 73

6.2 UAV Photogrammetry 73

6.2.1 UAV System Deployment 74

6.2.2 UAV Photogrammetry Data Processing 77

6.2.3 UAV Photogrammetry Advantages and Limitations 85

6.2.4 UAV Photogrammetry – Summary of Use on Very Slow, Vegetated Landslides 86

7.0 Comparison of Results from Monitoring Methods 88

7.1 Correlation and Consistency Analysis 92

8.0 Development and Kinematics of the Chin Coulee Landslide 96

8.1 Air Photo History of the Chin Coulee Region 96

8.2 Landslide Initiation and Contributing Factors 102

8.3 Landslide Failure Mechanism 104

8.4 Temporal Variation of Landslide Velocity 107

8.4.1 The Use of Slide 7.0 Analysis for Assessment of Landslide Driving Processes 109

8.5 Summary of Insights 118

9.0 Conclusions 120

9.1 Differential GPS 120

9.2 LiDAR Change Detection 121

9.3 UAV and Air Photo Change Detection 121

9.4 Kinematics of the Chin Coulee Landslide 122

10.0 Recommendations 124

References 125

List of Tables

Table 2-1: LiDAR specification comparisons (Teledyne Optech 2019; RIEGL Laser Measurement Systems 2019; Leica Camera AG 2019) 12
Table 2-2: UAV camera quality and range comparisons (SZ DJI Technology Co. 2019; Yuneec International 2019) 16
Table 3-1: Clay Till and Clay Fill soil properties on Chin Coulee (AMEC FW 2015) 29
Table 5-1: Summary of LiDAR scans 61
Table 6-1: Historical air photo year and resolution 69
Table 6-2: Summary of UAV flights 76
Table 6-3: Pix4DMapper processing options 77
Table 6-4: Quality report for Pix4DCapture generated models on August 23, 2018 Chin Coulee flight 78
Table 6-5: Quality report for Pix4DCapture generated models on July 30, 2019 Chin Coulee flight 79
Table 7-1: GPS, LiDAR, and UAV change detection results comparison for movement from August 23, 2018 to July 30 2019 90
Table 7-2: LiDAR and UAV movement by region from August 23, 2018 to July 30, 2019 92
Table 8-1: Clay Till gradation from borehole 2015-01 at depth of 14.0 m (AMEC FW 2015) 111
Table 8-2: Soil properties used in subsequent Slide 7.0 analyses 114
Table 8-3: Chin Coulee reservoir drawdown analysis - Results summary 117

List of Figures

Figure 2-1: Depiction of carrier phase GPS enhancement in RTK systems (NovAtel Inc. 2015 – With permission) 8
Figure 2-2: Displacement relationships for GPS units installed on the Super-Suaze earthflow (After Malet et al. 2002) 9
Figure 2-3: Cumulative displacement for various GPS units on 10-Mile slide (Rodriguez et al. 2018 – With permission) 11
Figure 2-4: Gallenzerkogel landslide in Austria (Eker et al. 2018 – With permission) 19
Figure 2-5: Conceptual drawing of C2C distance calculation (Lague et al. 2013 – With permission) 21
Figure 2-6: Conceptual drawing of M3C2 distance calculation (Lague et al. 2013 – With permission) 22
Figure 2-7: 10-Mile Slide location (Rodriguez et al. 2018 – With permission) 23
Figure 3-1: Location of the Chin Coulee landslide with respect to the province of Alberta (base imagery from ESRI 2018) 24
Figure 3-2: Historical air photo of the Chin Coulee landslide from 2012 (Alberta Air Photo Library 2012) 25
Figure 3-3: Current landslide extents and locations of slope inclinometers and piezometers (Green are currently functional, red are non-functional) (Base imagery from UAV flight conducted on August 23, 2018) 26
Figure 3-4: Chin Coulee stratigraphy along section A-A from Figure 3-3 28
Figure 3-5: Location of three weather stations averaged for weather data on-site (Google Earth 2015) 31
Figure 3-6: Slope inclinometer GA98-2 - Cumulative deflection in A direction (Downslope) (Modified from AMEC 2014) 33
Figure 3-7: Cumulative displacement at 8 m depth in slope inclinometer GA98-2 (Modified from AMEC FW 2015) 34
Figure 4-1: GPS unit locations on Chin Coulee landslide (Modified from Deane E. 2019) 36
Figure 4-2: Chin Coulee GPS deck screw pile installation (Hong 2018) 37

Figure 4-3: 10-Mile Slide GPS unit final setup (Rodriguez 2017) 37
Figure 4-4: Solar panel, GPS unit, and battery box setup on Chin Coulee (Hong 2018) 38
Figure 4-5: GPS battery box and batteries on Chin Coulee (Hong 2018) 38
Figure 4-6: Headscarp GPS unit at Chin Coulee after external antenna relocation and raised GPS unit 39
Figure 4-7: Cumulative horizontal displacement vectors of Geocubes (July 11, 2018 - July 30, 2019) (Base imagery ESRI 2019) 42
Figure 4-8: Cumulative vertical displacement vectors of Geocubes (July 11, 2018 - July 30, 2019) (Base imagery ESRI 2019) 42
Figure 4-9: Modified cumulative horizontal displacement of Geocubes (July 11, 2018 - July 30, 2019) 43
Figure 4-10: Modified cumulative vertical displacement of Geocubes (July 11, 2018 - July 30, 2019) 44
Figure 4-11: Geocube 151 (A) and 172 (B) on Chin Coulee and Geocube 46 (C) on 10-Mile 47
Figure 4-12: Geocube 46 on 10-Mile - Unadjusted data 48
Figure 4-13: Vandalism to Geocube on Chin Coulee. GPS and solar panel unscrewed and damaged 49
Figure 4-14: Geocube 154 on Chin Coulee before discontinuity removal (A) and after discontinuity removal (B) 50
Figure 4-15: Modified cumulative horizontal displacement of Chin Coulee Geocubes without discontinuity removal (July 11, 2018 – July 30, 2019) 51
Figure 4-16: Geocube horizontal displacement vectors on Chin Coulee from July 11, 2018 to April 6, 2019 before discontinuity removal (Base imagery from ESRI, 2019) 52
Figure 4-17: Geocube horizontal displacement vectors on Chin Coulee from July 11, 2018 to April 6, 2019 after discontinuity removal (Base imagery from ESRI, 2019) 52
Figure 4-18: Horizontal movement of Geocubes within the active region 56
Figure 5-1: ILRIS-LR LiDAR scanner used on Chin Coulee (Location 1) 59
Figure 5-2: LiDAR scan locations on Chin Coulee (Deane E., 2019) (Base imagery from Google Earth 2019) 60

Figure 5-3: Average TLS LiDAR scanning angle profile on Chin Coulee 60
Figure 5-4: LiDAR change detection on Chin Coulee between July 10, 2018 and August 23, 2018 (Only points above the LOD) 63
Figure 5-5: Level of detection on Chin Coulee LiDAR change detection between July 10, 2018 and August 23, 2018 63
Figure 5-6: LiDAR change detection on Chin Coulee between July 10, 2018 and October 13, 2018 indicating scan issues 64
Figure 5-7: LiDAR change detection on Chin Coulee between August 23, 2018 and July 29, 2019 showing detected movement 64
Figure 5-8: Level of detection on Chin Coulee LiDAR change detection between August 23, 2018 and July 29, 2019 65
Figure 6-1: 1982 photogrammetry model generated in Pix4D (Pix4D 2019) 70
Figure 6-2: 1982 photogrammetry model – July 29, 2019 LiDAR scan M3C2 change detection . 71
Figure 6-3: 1945 photogrammetry model generated in Pix4D showing unrealistically flat profile 72
Figure 6-4: Typical horst and graben structure common within sensitive clays (Geertsema, et al. 2018 – With permission) 73
Figure 6-5: Pix4DCapture flight plan ui for Chin Coulee (Pix4D 2019) 74
Figure 6-6: Pix4DCapture flight parameters on Chin Coulee (Pix4D 2019) 75
Figure 6-7: Typical ground control points and check point layout on Chin Coulee (Base imagery from ESRI 2019) 76
Figure 6-8: UAV photogrammetry model from August 23, 2018 flight on Chin Coulee 80
Figure 6-9: UAV photogrammetry model from July 30, 2019 flight on Chin Coulee 81
Figure 6-10: Ground classified UAV photogrammetry model from August 23, 2018 flight on Chin Coulee 82
Figure 6-11: M3C2 change detection completed between August 23, 2018 and July 30, 2019 (A), level of detection (B) 83
Figure 6-12: UAV-based qualitative change detection on Chin Coulee (1998 extents based on Golder and Associates 1998) 84

Figure 7-1: Pictorial comparison of M3C2 displacement vs GPS displacement 89
Figure 7-2: Technology results correlation and consistency analysis..... 93
Figure 8-1: 1945 Historical air photo showing original Highway 36 alignment within the now-filled Chin Coulee reservoir (modified from Alberta Air photo Library 1945)..... 98
Figure 8-2: 1960 Historical air photo indicating Highway 36 realignment and slope failure near the toe(modified from Alberta Air photo Library 1960)..... 98
Figure 8-3: 1970 Historical air photo indicating Highway 36 realignment, regrading and potential infilling near the headscarp (modified from Alberta Air Photo Library 1970) 99
Figure 8-4: 1982 Historical air photo indicating initiation of landslide movement (modified from Alberta Air photo Library 1982) 100
Figure 8-5: 1993 Historical air photo indicating significant advancement of landslide extents (modified from Alberta Air photo Library 1993)..... 100
Figure 8-6: 1999 Historical air photo indicating headscarp retrogression (modified from Alberta Air photo Library 1999)..... 101
Figure 8-7: Chin Coulee site history and antecedent precipitation from 1955 through 2019 ... 103
Figure 8-8: Geocube cross-sectional displacements (Base imagery from ESRI, 2019)..... 105
Figure 8-9: LiDAR change detection on Chin Coulee between August 23, 2018 and July 29, 2019 showing region definitions 106
Figure 8-10: UAV change detection on Chin Coulee between August 23, 2018 and July 29, 2019 showing region definitions 107
Figure 8-11: Geocube horizontal displacement in-depth analysis 108
Figure 8-12: Chin Lake average reservoir elevation from 1994 to 2019 (Saint Mary's River Irrigation District 2019)..... 109
Figure 8-13: Chin Coulee piezometers and standpipes (After Golder and Associates 1998; AMEC FW 2015)..... 112
Figure 8-14: Initial (Steady State) (A) and final (Transient) (B) reservoir states for permeability sensitivity analysis..... 113
Figure 8-15: Chin Coulee Clay Till permeability sensitivity analysis (5 meter drawdown over 55 days)..... 114

Figure 8-16: Chin Coulee 2018 drawdown stability analysis 116

Figure 8-17: Chin Coulee 2019 drawdown stability analysis 116

Figure 8-18: Chin Coulee critical drawdown stability analysis 117

Glossary of Terms

GPS – Global Positioning System

LiDAR – Light Detection and Ranging

UAV – Unmanned Aerial Vehicle

LOD – Level of Detection

InSAR – Interferometric Synthetic Aperture Radar

RTK – Real-time Kinematic

DEM – Digital Elevation Model

CSF – Cloth Simulation Filtering

SfM – Structure-from-Motion

GCP – Ground Control Point

RMS – Root Mean Square (Error)

C2C – Cloud to Cloud

M3C2 – Multiscale Model to Model Cloud Comparison

ROI – Regions of Interest

ICP – Iterative Closest Point

CP – Check Point

1.0 Introduction

As the affordability and accessibility of more modern technologies improves, their use in landslide and rockfall monitoring has become increasingly popular. The use of technologies such as terrestrial light detection and ranging (LiDAR) laser scanning, terrestrial and satellite-based interferometric synthetic aperture radar (InSAR), unmanned aerial vehicle (UAV) photogrammetry, and various global positioning system (GPS) technologies have opened up new means of data collection and analysis that was previously impossible with historical instrumentation methods (Jaboyedoff et al. 2012; Lato et al. 2016; Herrera et al. 2017; Fey and Wichmann 2017).

These modern technologies are not without limitations. This thesis focuses on presenting some of these limitations for Very slow and vegetated landslides, two conditions which push the limits of these technologies. Three of the above-mentioned technologies will be discussed: Terrestrial LiDAR, UAV photogrammetry, and differential GPS.

Vegetation has been shown to disrupt the functionality of LiDAR and UAV photogrammetry, reducing the practicality of photogrammetry and reducing the accuracy of LiDAR and UAV-based change detection (Jaboyedoff et al. 2012).

Slow movement presents a challenge for these technologies and processes as there is a minimum increment of movement that can be reliably detected between measurements (Fiani and Siani 2005; Teza et al. 2007; Abellán et al. 2009). This limit is commonly referred to as the level of detection (LOD). Landslide surface conditions and rates of displacement control how long the monitoring campaign must be, due to the minimum level of movement necessary in order to obtain movement above the LOD.

The Chin Coulee landslide, located in Southern Alberta, was selected for this research as it is both Very Slow and several large regions are covered in dense grass vegetation that obscures the surface. The Chin Coulee landslide has been monitored continuously since 1998 by Alberta Transportation and recorded slope inclinometer movement levels have been shown to be extremely low (AMEC 2004; AMEC FW 2015). Ground cover on site is primarily mid-height

prairie grasses. Headscarp and toe regions consist of tall prairie grasses and dense shrubbery. Data collected from Chin Coulee was compared to data previously collected from 10-Mile slide, located near Lillooet, British Columbia (Rodriguez et al. 2018). The 10-Mile slide is a light to non-vegetated, fast-moving landslide. The comparison with the data collected from this site was used to highlight problems that present in vegetated and Very Slow landslide conditions.

This thesis is presented in eight chapters. The content within each chapter is as follows:

Chapter 1: Introduction to the research, including the research objectives, research methodology, and expected contributions to the geotechnical community.

Chapter 2: A literature review, focusing on the use of GPS, LiDAR, and UAVs in landslide monitoring, an overview of the use of point clouds for change detection, as well as a brief review of 10-Mile slide.

Chapter 3: An introduction to the Chin Coulee site, landslide morphology and characteristics, geology, materials, climate, and history.

Chapter 4: A discussion regarding the installation and use of a differential GPS system on Chin Coulee, outlining some of the advantages and disadvantages of its application in Very Slow and vegetated conditions and methods for overcoming these disadvantages, advice regarding installation procedures, and result samples from the GPS units.

Chapter 5: A discussion regarding the use of a TLS LiDAR system on Chin Coulee for change detection outlining some of the advantages and disadvantages of its application in Very Slow and vegetated conditions. The means in which LiDAR data was collected and processed is outlined, and sample results are given.

Chapter 6: A discussion regarding the use of historical air photo and UAV photogrammetry on Chin Coulee outlining some of the advantages and disadvantages of photogrammetry in Very Slow and vegetated conditions. The methodology in which UAV based photogrammetry is performed is outlined, and a process for replicating air photo based photogrammetry is given.

Chapter 7: A correlation and consistency analysis comparing and interpreting the results of the three monitoring methods and a discussion regarding dissimilarity.

Chapter 8: An analysis of landslide initiation informed by air photo interpretation, analysis of the mechanism of failure based on the results obtained from each of the above technologies outlined in Chapters 4 through 6, and stability modelling to investigate the impact reservoir elevation has on landslide factor of safety.

1.1 Research Objectives

The objective of this research was focused on testing, understanding, and overcoming the limitations of UAV photogrammetry, GPS, and LiDAR change detection in Very Slow, vegetated landslide monitoring.

For this thesis, the following research objectives were identified and completed:

1) A literature review, with a focus on the use of differential GPS, LiDAR, and UAV photogrammetry for landslide monitoring and interpretation.
2) Development of a field research study site on the Chin Coulee landslide including installation of a differential GPS system and collection of 1 year of LiDAR, UAV, and GPS data.
3) Evaluation of the limitations of low-cost differential GPS for Very Slow natural soil slope landslide interpretation with a specific focus on GPS noise reduction, monitoring campaign duration related issues, and installation methodology.
4) Evaluation of the limitations of LiDAR monitoring for Very Slow natural soil slope landslide interpretation with a specific focus on bare earth model and monitoring campaign duration related issues.
5) Evaluation of the limitations of UAV monitoring and photogrammetry for Very Slow natural soil slope landslide interpretation with a specific focus on bare earth model related issues and change detection.
6) Quantification of the influence the Chin Coulee reservoir has on landslide stability.

1.2 Research Methodology

The research methodology used to achieve these research objectives is the following:

1) A review of available historical documentation for the Chin Coulee landslide including numerous reports submitted to Alberta Transportation from 1998 through the present. These reports document the history of engineering works and monitoring completed as well as historical information regarding the landslide. Historical air photos obtained from the Alberta Air Photo Library were analyzed for information regarding historical landslide evolution and triggering mechanisms.
2) A differential GPS system was installed on Chin Coulee landslide and LiDAR scanning and UAV flights were periodically conducted throughout 2018 and 2019 to obtain spatial information.
3) Processing and analysis of the GPS, LiDAR, and UAV data was completed by the author to allow for interpretation of results. An analysis of the quality of the collected data was completed with 10-Mile slide used for comparison.
4) Creation of a limit equilibrium method model using the software program Slide 7.0 along with geological and topological information to create numerous models to quantify the influence of reservoir elevation on landslide stability.

1.3 Expected Contribution

This research focuses on understanding the limitations of differential GPS, UAV photogrammetry, and LiDAR technologies. Understanding conditions in which these technologies are appropriate is important as industry implementation and adoption of these technologies increases. By applying these technologies to the Chin Coulee landslide, we can push the limitations of these technologies and observe and document issues which arise due to vegetation and Very Slow conditions. This allows future practitioners to have a better understanding of whether a technology will work on their site, what issues they should expect to arise, and what methods they can use to improve their results. Better understanding of these technologies is important for promoting adoption into practitioner workflows and promotes technological advancement from manufacturers.

Research into the Chin Coulee landslide provides results which can be applied to other landslides within the Chin Lake reservoir and provides a discussion regarding Very Slow landslides and associated monitoring and instrumentation concerns specifically related to Very Slow conditions.

2.0 Literature Review

This chapter presents a review of the concepts behind differential GPS, LiDAR, and UAV photogrammetry in addition to other research performed using these technologies. A brief presentation and description of change detection is performed, along with an overview of 10-Mile slide.

2.1 Use of Differential GPS in Landslide Monitoring

Selective Availability, a limitation imposed by the US government on GPS which limited the accuracy of non-military GPS units (Office of the Press Secretary 2000), was removed in May 2000. The use of GPS expanded significantly in the following decade with the advent of higher resolution and more affordable GPS units and has become a staple in all engineering fields.

High accuracy GPS systems use two frequencies. The use of two frequencies reduces a significant portion of GPS error associated with signal delay through the ionosphere. This is achieved because of the known relationship between signal delay, frequency, and total electron content (The number of electrons present within a section of ionosphere) (NovAtel Inc. 2015). Observing the variation between the arrival time of both frequencies allows for a precise calculation of atmospheric properties with corrections then being applied.

According to a report published by the American National Transportation Board (Federal Aviation Administration 2017), single receiver GPS accuracy is less than ±1.891 m (95th percentile) horizontally. This accuracy level is adequate for many applications such as cellular navigation however most engineering applications require considerably more accurate measurements. GPS accuracy can be improved using a process commonly known as Real-time Kinematic (RTK). This process involves the use of a fixed base station and several mobile GPS units. By measuring the incoming signal to the fixed base station and applying mathematical procedures to align the phase of the signal, a large portion of GPS error can be removed (R. Langley 1998). This process vastly improves the relative accuracy of the mobile GPS receivers. Figure 2-1 depicts this concept, referred to as Carrier Phase Enhancement. Typical accuracies for modern RTK systems are 1 centimeter horizontally and 2 centimeters vertically for most application settings (Takasu and Yasuda 2009). Despite this large improvement to relative

accuracy, the global accuracy of the system is still equivalent to the calculated accuracy of the base station location.

RTK GPS setups are subject to several constraints. The fixed base station must be close enough to and at a similar elevation to the moving GPS units in order to accurately remove errors due to ionospheric signal delay (Ophelia-Sensors 2019). These constraints may be automatically met due to the requirement for radio communication between GPS units and the fixed-point base station in some systems. All GPS units in the system should also have a clear line of sight to the sky to minimize multipath errors and increase the number of visible satellites.

Multipath error is associated with GPS signal bouncing off a nearby object before being received by the GPS unit. This changes the distance in which the signal had to travel, which in turn changes the apparent location of the GPS device according to the GPS receiver (NovAtel Inc. 2015). Ways in which multipath error could be reducing include locating the GPS units in an open area with no trees or tall structures nearby or increasing the height of the GPS unit from the ground. Rain and snow also introduces multipath errors although these are typically temporally short events (Ophelia-Sensors 2019).

GPS technology is often used in landslide monitoring for observing movement using permanent differential GPS installations or benchmarks (Malet et al. 2002; Tagliavini et al. 2007; Wang 2011; Herrera et al. 2017; Rodriguez et al. 2018). GPS is often employed alongside additional monitoring methods to fill gaps in data or to provide a comparison of measurement methodology.

Differential GPS systems provide a means of selecting a specific location and recording continuous movement at that location with accuracy levels from 1 – 2 mm under certain conditions (Malet et al. 2002; Rodriguez et al. 2018). This allows for tracking of specific features, such as headscarp or block movement within a landslide. Differential GPS can also be combined with non-continuous monitoring tools such as LiDAR or discontinuous InSAR in order to improve monitoring and observe movement trends between scans (Malet et al. 2002; Herrera et al. 2017; Rodriguez et al. 2018).

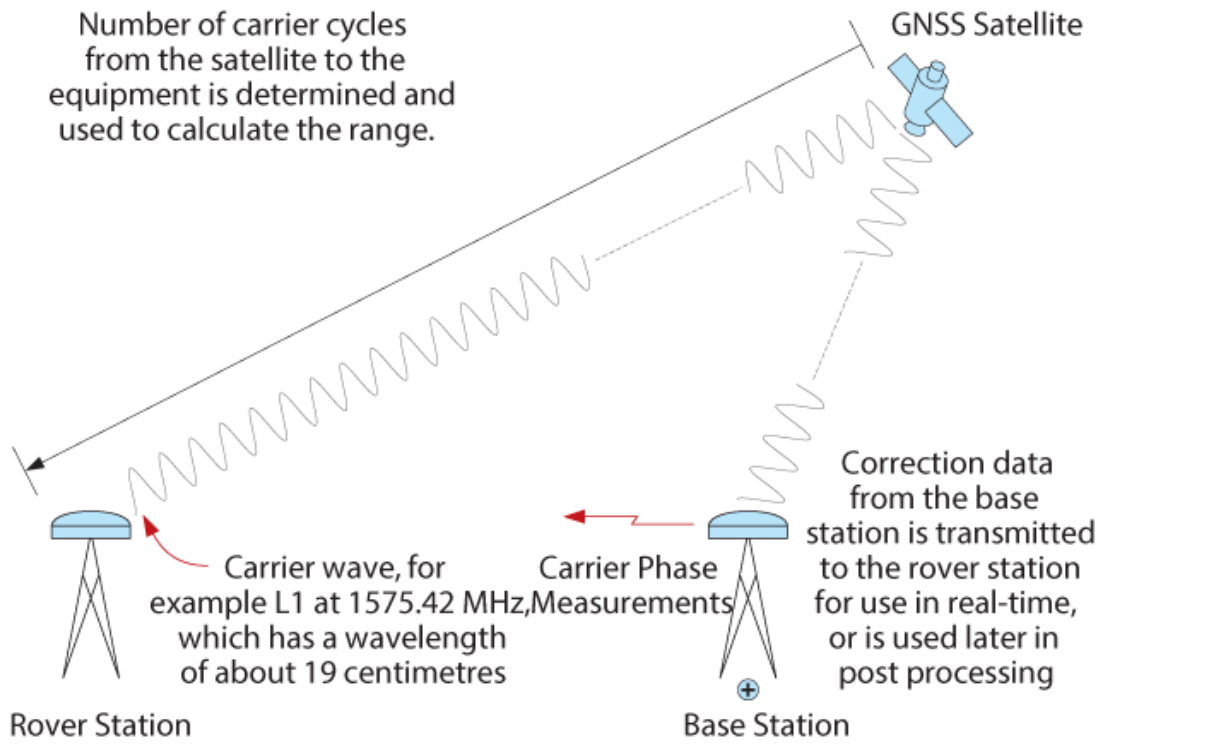

Figure 2-1: Depiction of carrier phase GPS enhancement in RTK systems (NovAtel Inc. 2015 – With permission)

The GPS system used for this research is the Geocube™ system created by Ophelia Sensors. The University of Alberta has significant experience working with this system from research on Ripley slide and 10-Mile slide. The Geocube system employs a central processing unit, referred to as a coordinator which is connected to the rest of the system through radio. This allows the GPS system to save costs by reducing redundancy. Each GPS set-up only requires a radio and a GPS, all data storage and processing is done on the central coordinator. As a side effect, each individual GPS unit has limited storage and processing capability and must be connected to the coordinator via its radio connection in order to upload data. Should this radio connection be disrupted, data may be lost during that down time.

2.1.1 Differential GPS Accuracy

Malet et al. (2002) applied a GPS system for continuous monitoring of the Super-Sauze earthflow in France. His goal was in part to determine the accuracy level of GPS based systems by comparing GPS measurements to more traditional methods including topometry and extensometry. Malet showed that when using a GPS system calibrated to observe data in a 24-hour time period a "detectability threshold" of ±3.5 mm/24-hours horizontally and ±6 mm/24-hours vertically was possible. If the system was calibrated for measurements every hour this threshold increased to ±8.5 mm/hour horizontally and ±19.5 mm/hour vertically. This shows the effect of extending the monitoring duration of GPS systems to gain increased accuracy.

Malet determined landslide horizontal displacements ranged from 15 cm to 204 cm over the course of 17 days (See Figure 2-2). It was found that topometry and other traditional forms of instrumentation showed very similar results to GPS collected data indicating that GPS was able to accurately measure displacements, with much higher periodicity than traditional measurement devices.

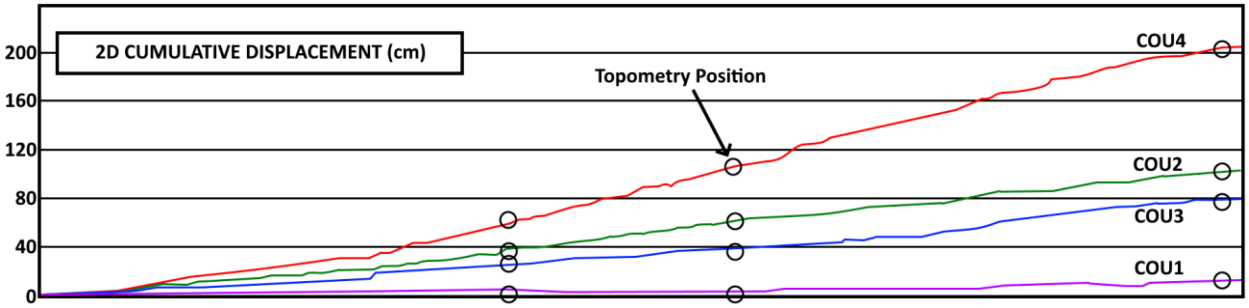

Figure 2-2: Displacement relationships for GPS units installed on the Super-Suaze earthflow (After Malet et al. 2002)

2.1.2 Differential GPS Combined Systems

Herrera et al. (2017) combined the use of InSAR and differential GPS on Petrasos peak in France, using InSAR to increase the spatial coverage of monitoring. Herrera performed periodic GPS measurements, with 19 measurements taken between May 2006 to October 2015. These

measurements were done using an RTK system with error on the order of ± 1.5 cm. Permanently installed GPS systems were not used. Herrera stated that the GPS measurements were useful in determining kinematics of the landslide and for comparison to the collected InSAR data but could not be related with rainfall. Permanent installations of GPS with more continuous monitoring would likely have allowed for a relationship between movement and precipitation to be better analyzed.

Rodriguez et al. (2018) combined the use of a differential GPS system with LiDAR on the 10-Mile slide in British Columbia. Movement levels on 10-Mile slide are quite large, in excess of 400 mm/year in some locations (Figure 2-3). This led to very discernible and smooth trends in GPS data. Achievable GPS accuracy was 1 – 2 mm with a fixed point located less than 500 m from the remaining GPS units. With 24-hour readings GPS accuracy under ideal environmental conditions can range from 1 – 2 mm with a fixed point up to 1000 meters from the remaining GPS units and 2 – 4 mm at 3000 meters (Ophelia-Sensors 2019). These numbers are based on ideal conditions and accuracy levels should be expected to be lower than this in real world application.

GPS is a well proven technology, but accuracy and spatial monitoring extents are a limitation. With GPS it is not yet possible to achieve high spatial coverage, with high accuracy, at a low cost. Installation requirements may additionally limit the effectiveness of applying a GPS system, depending on the required accuracy and site restraints (For example, distance from the fixed point to the mobile points) (Ophelia-Sensors 2019).

The applicability of GPS at extremely low movement levels poses a challenge due to the limits in accuracy. By applying this technology to Chin Coulee, we were able to test the limitations of GPS when monthly landslide movement levels are near the accuracy of the GPS unit itself.

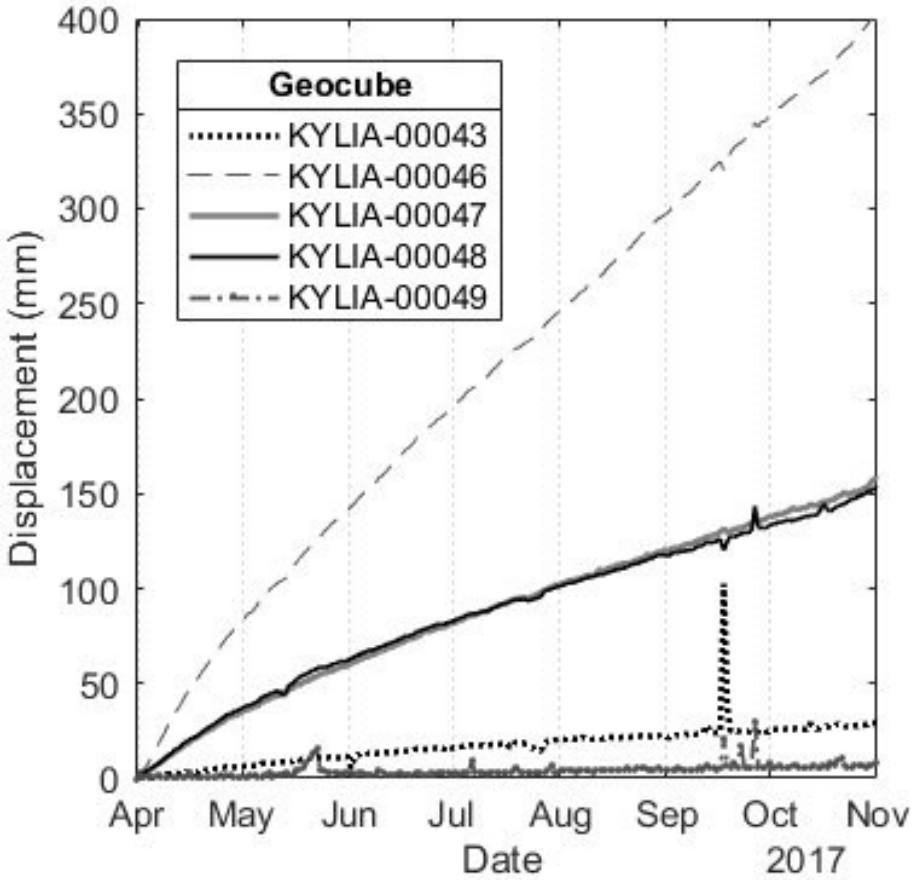

Figure 2-3: Cumulative displacement for various GPS units on 10-Mile slide (Rodriguez et al. 2018 – With permission)

2.2 Use of LiDAR in Landslide Monitoring

The laser was first invented in 1960 (Lengyel 1962) and harbored a new age of technological advancement in hundreds of fields over the following decades. Among those advancements was the initial creation of LiDAR around 1963. LiDAR's first real use was in meteorology where it was used for investigating atmospheric properties (Goyer and Watson 1963). LiDAR was later notably used in 1971 for the Apollo 15 mission to map part of the lunar surface (Sun 2013).

Two forms of LiDAR exist, time-of-flight (Or pulse) and phase-offset (Jaboyedoff et al. 2012; Lato 2010). Time-of-flight is the most practical form of LiDAR for large scale geotechnical applications (Outside of tunneling) due to range limitations with phase-offset sensors (Higgins

2004). Any reference to LiDAR hereafter will be in reference to a time-of-flight sensor. In practice, both sensors produce the same resulting point clouds.

Conceptually, LiDAR scanning is the process of emitting a laser beam with a specific wavelength, this wave impacts an object and returns to the sensor where the time for reflection is recorded. The time in which this reflection occurs indicates the distance in which the object is located (Lato 2010). In basic laser distance readers this is done only once or continuously. In more advanced and specialized LiDAR scanners this process is repeated thousands to millions of times, varying the location of the laser beam slightly so that a full "distance map" is generated (Jaboyedoff et al. 2012). Through this process a 3-dimensional map of points is created.

Specific laser properties used for LiDAR scanners vary depending on the manufacturer. For this research an Optech ILRIS-LR LiDAR scanner was used. Although not a modern-day top-of-the-line scanner, its specifications are comparable to current generation scanners.

Specifications of LiDAR scanners from various manufacturers are outlined in Table 2-1.

Table 2-1: LiDAR specification comparisons (Teledyne Optech 2019; RIEGL Laser Measurement Systems 2019; Leica Camera AG 2019)

LiDAR Scanner Model / **Property**	**Optech ILRIS LR (This Research)**	**Teledyne Optech Polaris LR**	**Riegl VZ-6000**	**Leica ScanStation P50**
Wavelength	1064 nm	1550 nm	*Not listed*	1550 nm
Range Accuracy	7 mm @ 100 m	5 mm @ 100 m	15 mm @ 150 m	3 mm + 10ppm in >1 km mode
Angular Resolution	20 µrad	12 µrad	~ 8.7 µrad	Not Specified
Beam Divergence	0.25 mrad	Not Specified	0.12 mrad	0.23 mrad

In the field of geotechnical engineering LiDAR has been used extensively in landslide monitoring, rockfall monitoring, tunnel monitoring, and mine wall monitoring (Teza et al. 2007; Lato 2010; Jaboyedoff et al. 2012; Kromer et al. 2018; Sala et al. 2019). LiDAR is useful for landslide monitoring due to the ease in which a large spatial extent can be captured with high resolution.

Change detection and digital elevation models (DEMs) are the two primary products obtained from LiDAR data collection. LiDAR change detection is based on the process of using temporally separated scans to detect variation over time (Jaboyedoff et al. 2012). Scans from separate time periods are aligned using point cloud software and the separation between point clouds is stated as the change or movement over that time frame. The accuracy and ability to acquire detected changes is subject to several factors including the point density (a function of the distance to the target and selected scan parameters), the sensor precision, and the allowed time for scanning (Jaboyedoff et al. 2012). The angle of incidence to the target also impacts point density due to the inability of the scanner to recognize distance changes and adjust scan point density (Fey and Wichmann 2017). Vegetation plays a major role in change detection due to vegetation growth being potentially misconstrued as surface movement. Vegetation can be reduced or removed through several methods within the scanner itself ("last reflection" options) and post processing (Brodu and Lague 2012).

In most situations, LiDAR scanning required a person on site to set up and operate the scanner, as opposed to InSAR scanning which can be mostly automated. This scanning procedure requires continuous costs associated with sending people to the field to collect data, while an automatic scanning system removes this cost at the expense of upfront installation costs. Continuous, near-real-time monitoring using LiDAR is not possible to the same extent as InSAR or GPS based early warning systems are capable of. Research into automated LiDAR-based early warning systems is ongoing (Grejner-Brzezinska et al. 2015).

2.2.1 LiDAR Data Density

Due to the discrete and unvegetated nature of most rockfall scenarios, LiDAR has been used to great success in bare rockfaces. Lato (2010) published works on the application of terrestrial

LiDAR for mine safety, in which rock face outcrops were measured and analyzed for potential safety concerns. Lato showed that LiDAR worked well for identification of planar features and could be further used for assessment of joint spacings and discontinuity lengths in addition to volume calculations.

Lato also showed the applicability of mobile LiDAR for rockfall safety along a transportation corridor (Lato 2010). One notable downside of the mobile LiDAR unit employed was reduced point density. The achieved point density for Lato's system ranged from 50 to 500 points/m^2. In contrast, achievable point density on Chin Coulee landslide scans was roughly 2,500 points/m^2 corresponding to a point spacing of 20 mm. Point density defines the minimum scale in which change detection can be performed, identification of smaller scale movements will not be possible with larger point spacings. In the case of Lato's mobile LiDAR data, detectable feature size was roughly 20 cm x 20 cm. A lower point density does not inherently signify worse data, less density can be useful as it reduces the potential for point error to impact results (Lato et al. 2009). Despite the reduced point density, Lato's system was highly successful due to the volume of data that was able to be collected.

2.2.2 LiDAR and Vegetation

Removal of vegetation is critical for LiDAR based change detection. Sharma et al. (2010) tested a system to remove vegetation cover from a watershed LiDAR scan for the purpose of creating a bare earth model. The method in which vegetation was reduced was based on a given slope threshold, working on the principle that a tree or shrub would result in a large and abrupt slope change that would not naturally occur in the environment. The work was successful, but it was noted that this process would not be applicable to more complex geometry such as ravines or river valleys. Due to the complex topography featured in most landslide environments the method that Sharma outlined has limited use for evaluation and removal of vegetation in landslide environments.

Advanced means of vegetation classification beyond slope measurements are required to remove vegetation from complex environments. Brodu et al. (2012) introduced CANUPO classification. CANUPO classification is a tool which uses various scales and dimensionality

observations to classify local cloud geometry. This multi-scale approach improves detection accuracy and speed over other single scale approaches (Brodu and Lague 2012). Based on visual inspection, CANUPO classification works very well in most cases and removes the majority of visually identifiable vegetation from point clouds.

The second issue for LiDAR change detection is cloud alignment. Cloud alignment can be improved simply by reducing vegetation levels, so a bare earth model can be obtained, or through the use of LiDAR ground control points (Alba et al. 2006). Cloud alignment is largely a user-based issue that can be improved with care taken during scanning and processing and mechanical means of improving the generated point clouds.

2.3 Use of UAV in Landslide Monitoring

Aerial photography has a long history of use in engineering. Linear infrastructure design has taken advantage of large data sets of historical air photos to plan road, pipeline, and powerline construction projects since air photography began (Miles 1953; Bailey 1958). In the field of geotechnical engineering, helicopter-based monitoring has been used to observe geotechnical hazards from the air (Updike 1983; Baron et al. 2013; Baczynski et al. 2017). However, helicopter-based monitoring has always been limited by expense and scheduling requirements. Light-weight UAV commercial availability began around the late 2000's although early models were expensive and less user friendly. Advancements in light-weight UAVs have led to improvements in battery life, camera resolution, and software support.

A UAV can be used for capturing close up views of hard to reach locations on site, such as a tall cliff face, or a large aerial overheard image of the site. This allows for increased safety during monitoring and reduces the amount of time needed to perform basic inspections. Viewing a site from above also provides insight into morphology or erosional changes which may be difficult to fully capture and observe from the ground. In most scenarios (within Canada), flight beyond visual line of sight with a UAV is not permitted, meaning controller range limitations are not a limiting factor for flight distance. Table 2-2 compares the price, camera quality, and reported flight range for several commercially available UAVs.

Table 2-2: UAV camera quality and range comparisons (SZ DJI Technology Co. 2019; Yuneec International 2019)

UAV Model	Price[1]	Camera Quality	Reported Range
DJI Phantom 4 (Used for this research)	Discontinued	12 MP	5 km (unobstructed)
DJI Phantom 4 V2.0	USD $1,499	20 MP	7 km (unobstructed)
DJI Mavic 2 Pro	USD $1,499	20 MP	8 km (unobstructed)
DJI Spark	USD $399	12 MP	2 km (unobstructed)
Yuneec Mantis Q	USD $499	13 MP	1.5 km (unobstructed)
Yuneec Breeze	USD $399	13 MP	Not Given

[1] Price based on manufacturer specified price as of June 28, 2019

One of the uses of UAV is the ability to capture photographs of a landslide or geohazard and using advanced photogrammetry software (Pix4DMapper, Autodesk ReCap, AdamTech, Agisoft Metashape, Regard3D) generate a 3-dimensional model. This process is also referred to as Structure-from-Motion (SfM). This procedure has become increasingly popular, including work from Niethammer et al. 2012, Danzi et al. 2013, Siebart et al. 2014, Ely et al. 2017, Cook 2017, Peppa et al. 2018, and Rodriguez et al. 2018.

UAV based photogrammetry is the process in which multiple photographs collected from a UAV are processed using computer vision algorithms to produce 3D models of the target object (Pix4D 2019). The process begins by identification of keypoints within multiple images that are believed to align and generates a point cloud based on matched points. The elevation geometry of this 3D point cloud model is determined using advanced computer vision algorithms and is outside the scope of this research (Pix4D 2019).

Accuracy of the 3D model is increased using user-measured ground control points (GCPs) which are points located within the photographs that have a known geo-location. By identifying GCPs within the photographs, the geolocation of the model can be improved, increasing the accuracy

of the final model. The improvement to the model is dependent on the accuracy of the GCP measurement (Pix4D 2019).

The goal of photogrammetry for geotechnical engineering is typically to produce a DEM, which can be used to analyze mechanisms of a landslide or rockface. In this manner, UAV can replace or supplement other spatial observation tools such as LiDAR. UAV photogrammetry can often obtain complete spatial coverage of the target rockface or landslide, unlike LiDAR in which spatial coverage can be influenced by geometry.

Aerial LiDAR scanners mounted on UAV's are also becoming more popular (Pirasteh and Li 2017; Xiong et al. 2018). As the technology improves, systems that incorporate aerial LiDAR with aerial photography to obtain colormaps will likely become a powerful tool, incorporating the advantages of both LiDAR and photogrammetry.

One notable limitation of UAV photogrammetry compared to other remote sensing methods is point accuracy (Siebert and Teizer 2014). Point accuracy obtained from UAV photogrammetry is less than that obtained from TLS LiDAR under almost all conditions.

Point spacing achievable with typical UAV flight parameters ranges from 1 – 3 cm, although this depends heavily on the quality of the camera, the height in which the photos were taken, the overlap in the photos, the number of photos, as well as the input parameters for the photogrammetry software (Siebert and Teizer 2014). Photogrammetry point accuracy depends in part on the quality and number of GCP's used and photograph quality.

As photographs do not penetrate vegetation obtaining a bare earth DEM is not possible in vegetated regions. This means that change detection cannot be accurately performed using photogrammetry models in highly vegetated regions as ground movement is undiscernible from vegetation growth. Vegetation also creates a secondary problem for photogrammetry by increasing surface roughness which reduces point accuracy (Cook 2017).

2.3.1 UAV Flight Parameters and Error

With rock faces, highly accurate bare earth DEM's can be generated solely from photogrammetry due to low levels of vegetation. Danzi et al. (2013) flew two UAV surveys of

rock faces in Italy with roughly 70% image overlap and was able to create a 3D model which allowed for observation of structural geology. Combining the results of the UAV photogrammetric model with the program DIPS, joint sets were identified, aiding in stability analysis for the rockface.

Siebart et al. (2014) published work which compared several potential improvements to the work previously conducted by Nietzel (2011) regarding UAV generated photogrammetry models. His goal was to see the impact various photographic collection methods had on photogrammetry results. Siebart showed that increasing the number of GCPs from 6 to 9 and increasing the flying altitude from 30 to 50 m, which increased the amount of overlap between photos, decreased model positional error. The average positional error of Nietzel's model was found to be ±5.6 cm, with an average height error of ±2.5 cm. In comparison, the improved Siebart 2012 model had an average positional error of ±4.9 cm and an average height error of ±1.1 cm. Siebart went on to show that UAV photogrammetry could generate a DEM of an excavation with a point density of 561 points/m^2 and point accuracy below 1 cm. This was a significant reduction in time for processing, and a significant increase in total volume accuracy compared to traditional RTK measuring.

2.3.2 UAV Ground Control Points

Placement of GCP's is not always possible due to site access, but the improvements to model accuracy that GCP's offer is invaluable. Peppa et al. (2018) created a morphology-based, pseudo-GCP generation methodology which allowed for the identification of relatively stable ground regions which would then be used as pseudo-GCPs in later UAV flights. This methodology allowed for a one-time placement of GCPs for generating the first, high-accuracy model, and no subsequent GCP's would be required for later flights. The ability to create UAV-based photogrammetry models without the need to measure GCP's allows for rapid monitoring of a site, as placing and measuring GCP's often takes longer than the flight itself.

2.3.3 UAV Landslide Monitoring

Eker et al. (2018) showed a detailed use of UAV generated photogrammetric change detection on the Gallenzerkogel landslide located in Austria. Nine GCPs and Agisoft Photoscan was used

to generate the 3D photogrammetric models. An average ground sampling distance, or photogrammetric model point density, of 0.792 cm/pixel and an average root mean square (RMS) error of 4 cm was obtained. Eker determined the movement of the landslide based on the photogrammetric models using change detection. It was shown that this method was a viable means of determining movement as an alternative to more standard approaches such as LiDAR change detection.

It should be noted that the Gallenzerkogel landslide is vegetated. Eker identified the region of most significant movement in the center of the landslide, however, it should be noted that this region is significantly less vegetated than the edges of the landslide (See Figure 2-4). Although not stated, less change may have been detected along the side of the active region due to the vegetation itself. It is important to understand the geometry and site conditions of a landslide before applying photogrammetry-based change detection.

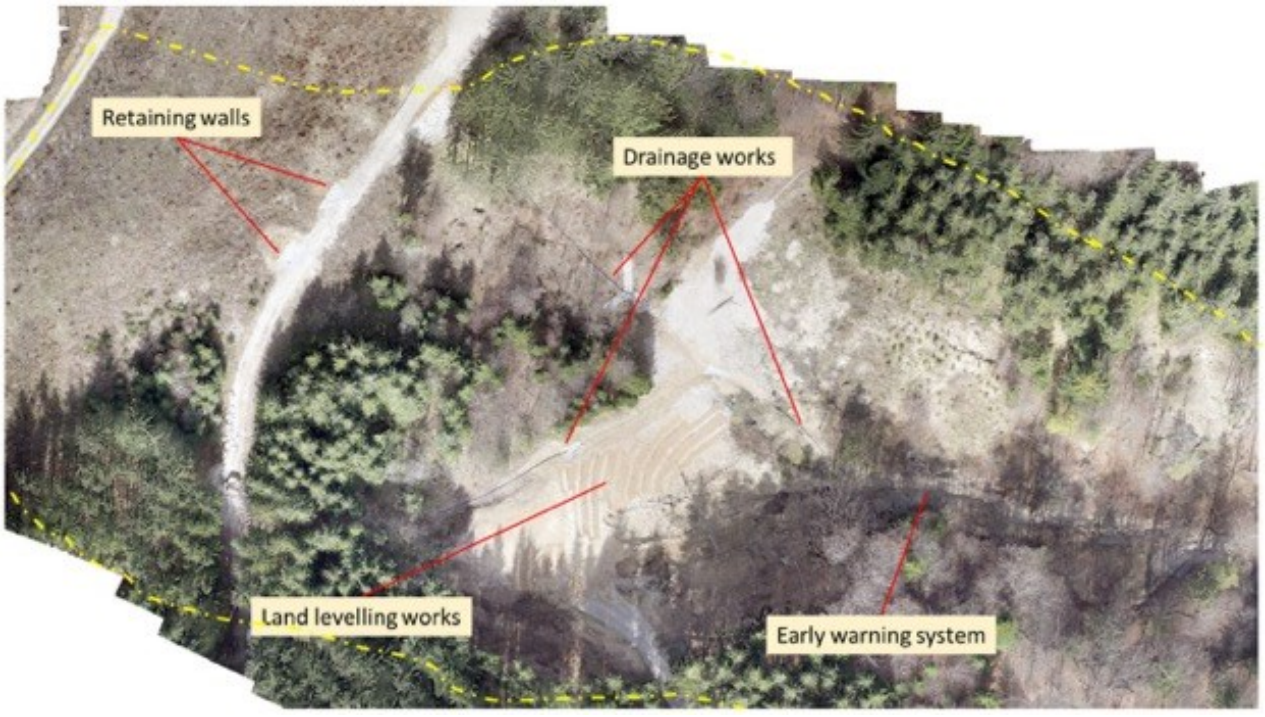

Figure 2-4: Gallenzerkogel landslide in Austria (Eker et al. 2018 – With permission)

Rodriguez (2018) also used photogrammetry-based models of the 10-mile slide near Lillooet, Canada to perform change detection. This work showed that detectable movement levels similar to LiDAR was possible with the use of UAV. Additional information regarding 10-Mile slide is available in Section 2.5.

Like LiDAR, UAV photogrammetry-based change detection is limited by level of detection (LOD). There is a finite level of accuracy available within both LiDAR and UAV photogrammetry-based point clouds, and movement below certain levels cannot be detected accurately. Vegetation is a fundamental issue with photogrammetry-based change detection as there is no way for photographs to penetrate vegetation. This limits the practicality of UAV photogrammetry-based change detection on vegetated sites such as Chin Coulee, however, given enough movement, statements about movement are possible.

2.4 Analysis of Point Clouds for Change Detection

The process of change detection for LiDAR and UAV data is performed using distance calculations, the most common being Cloud to Cloud (C2C) and Multiscale Model to Model Cloud Comparison (M3C2) (Lague et al. 2013).

C2C change detection uses the concept of “nearest neighbor” to compute the distance, or change, between clouds. This is a limiting concept because the closest point may not correctly be associated with movement. If one cloud has a large shadow (A region in which the terrain is blocked from the line of sight of the scanner resulting in missing points within the point cloud) points within that shadow on the previous scan associate with points located on the periphery of the later scan. This results in erroneously large amounts of movement being recorded. Figure 2-5A depicts the concept of C2C pictorially. C2C is also prone to problems when the surface is rough, a common problem in vegetated regions (Lague et al. 2013).

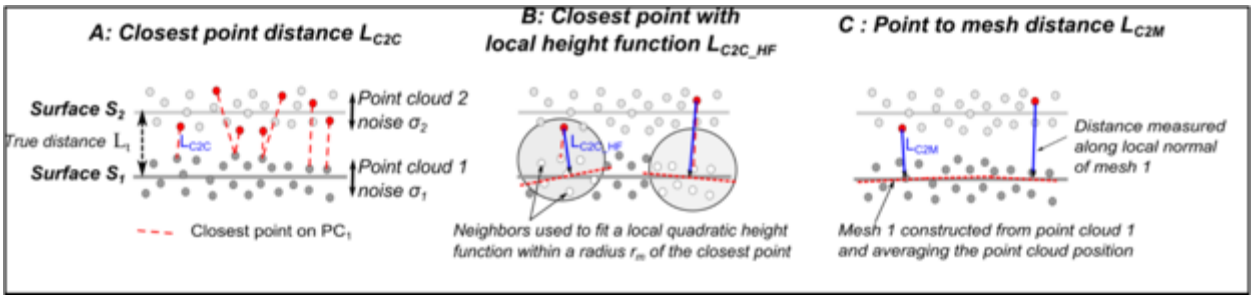

Figure 2-5: Conceptual drawing of C2C distance calculation (Lague et al. 2013 – With permission)

M3C2 was created in 2013 by Lague et al. to improve upon C2C. The M3C2 method reduces errors associated with LiDAR scanning, specifically registration error associated with aligning clouds and surface roughness related errors.

In M3C2 certain points on a cloud are denoted as “core points” and a normal vector is created for these core points. To account for surface roughness, the standard deviation of the distance from each point within a user-defined radius, to the plane defined for the normal calculation is determined (Lague et al. 2013). This allows for the roughness to be averaged out and points outside a certain standard deviation are rejected from the distance calculation. For each core point, a cylinder of predefined length is projected in the normal direction to the adjacent cloud, and an average position of the points within that cylinder is defined. The distance between the average location within both cylinders is used as the distance between clouds for that core point (Lague et al. 2013). Figure 2-6 shows the M3C2 concept pictorially, as well as indicates a potential for error.

If a normal scale that is too small is selected, surface roughness will begin to influence the distance calculated between the clouds, potentially overestimating or underestimating the distance between these clouds. By increasing the normal scale, surface roughness is smoothed and a more average distance is determined, at the cost of surficial definition (Lague et al. 2013).

The M3C2 and C2C algorithms are incorporated into the free and open source software program CloudCompare, which was used for all point cloud analysis conducted for this research (Girardeau-Montaut 2019).

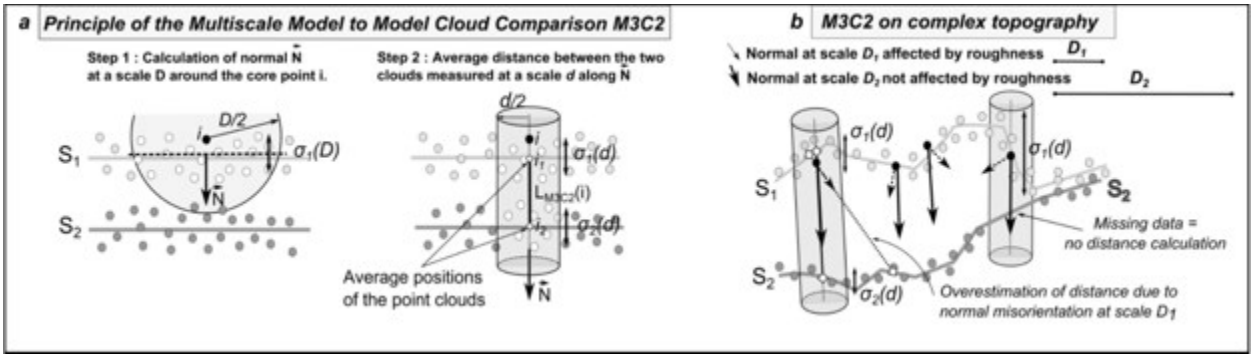

Figure 2-6: Conceptual drawing of M3C2 distance calculation (Lague et al. 2013 – With permission)

2.5 10-Mile Slide

10-Mile slide is located in interior British Columbia, Canada, North East of the town of Lillooet (See Figure 2-7). The landslide itself is a reactivated portion of a post-glacial earthflow (Rodriguez et al. 2018). 10-Mile slide is situated on an important transportation corridor with a CN secondary rail line, as well as Highway 99 passing through the landslide region.

10-Mile slide is quite active, with deformations of up to 10 mm/day in some regions (Macciotta et al. 2017). Installation of a large pile wall in 2008 below the rail line has significantly slowed movement of the rail line but deformations continue to impact the highway.

Borehole information has shown that the landslide material consists primarily of clays and silts overlying glacial till materials. The material is notably variable throughout the site due to the intense amount of movement observed on the landslide (Macciotta et al. 2017).

Slope inclinometers typically shear within weeks of installation on 10-Mile slide due to the large amount of ground movement. As a result, remote sensing technologies including LiDAR and UAV photogrammetry became a primary monitoring method, with significant amounts of LiDAR data collected by the University of Alberta and engineering consultant BGC.

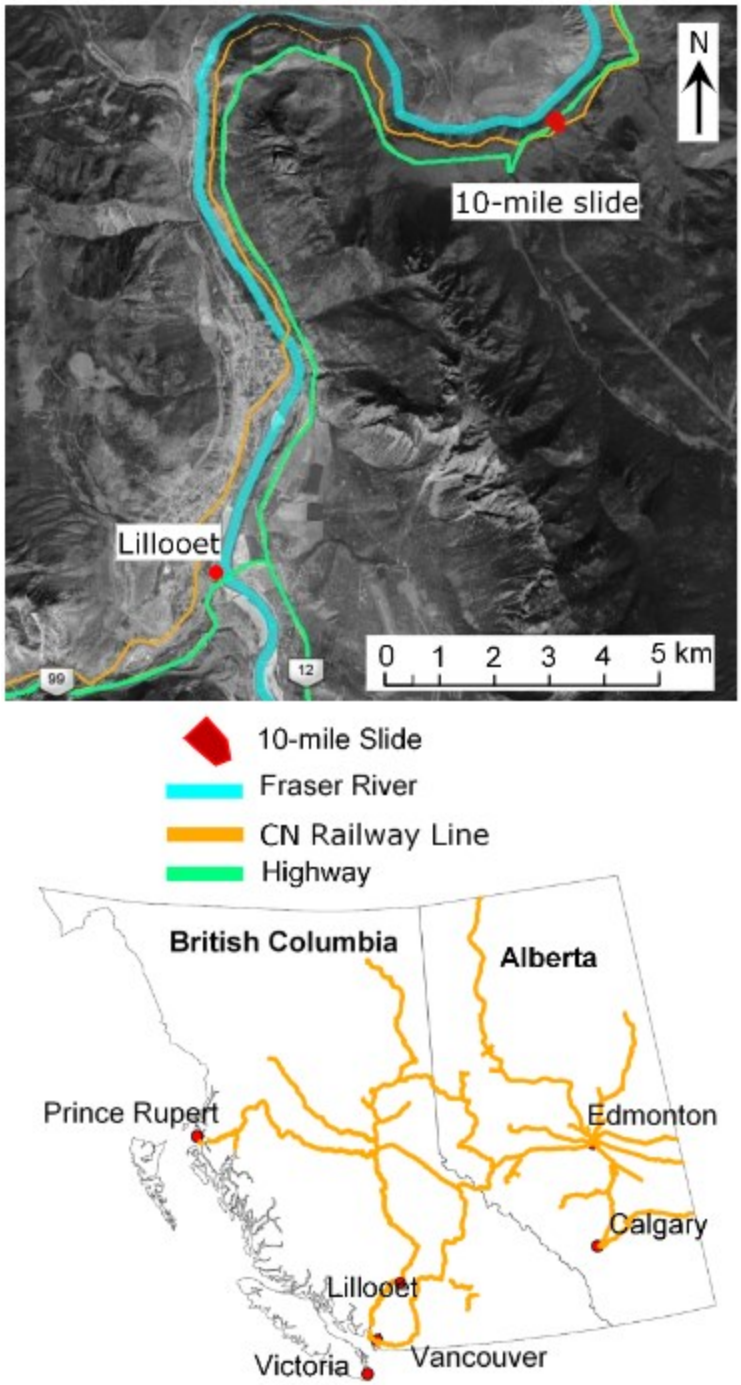

Figure 2-7: 10-Mile Slide location (Rodriguez et al. 2018 – With permission)

3.0 The Chin Coulee Landslide

This chapter introduces the Chin Coulee landslide and provides an overview of all existing information regarding location, characteristics, geology, and material properties of the Chin Coulee landslide. A history of the landslide through historical instrumentation is provided. In-depth discussion regarding landslide initiation and continued movement is in Chapter 8.

3.1 Location

The Chin Coulee landslide is situated on a northern sloped valley of Chin Lake reservoir, adjacent to Alberta Highway 36 in Southern Alberta (Figure 3-1 and Figure 3-2). Chin Lake is an important agricultural reservoir for the surrounding farmland in Warner, Lethbridge, and Taber counties. Highway 36 is a rural, two lane, paved highway with an average annual daily traffic volume of 880 vehicles/day (Government of Alberta, 2017). Highway 36 crosses Chin Lake 20 km south of Taber before cutting eastward across the northern slope and the headscarp of the Chin Coulee landslide. Figure 3-1 indicates the location of the Chin Coulee landslide within Alberta and Figure 3-2 shows a historical photograph of the landslide from 2012.

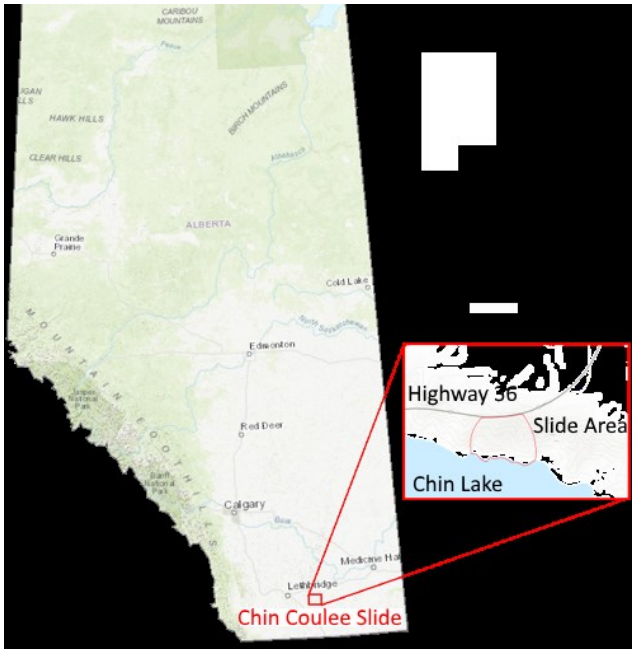

Figure 3-1: Location of the Chin Coulee landslide with respect to the province of Alberta (base imagery from ESRI 2018)

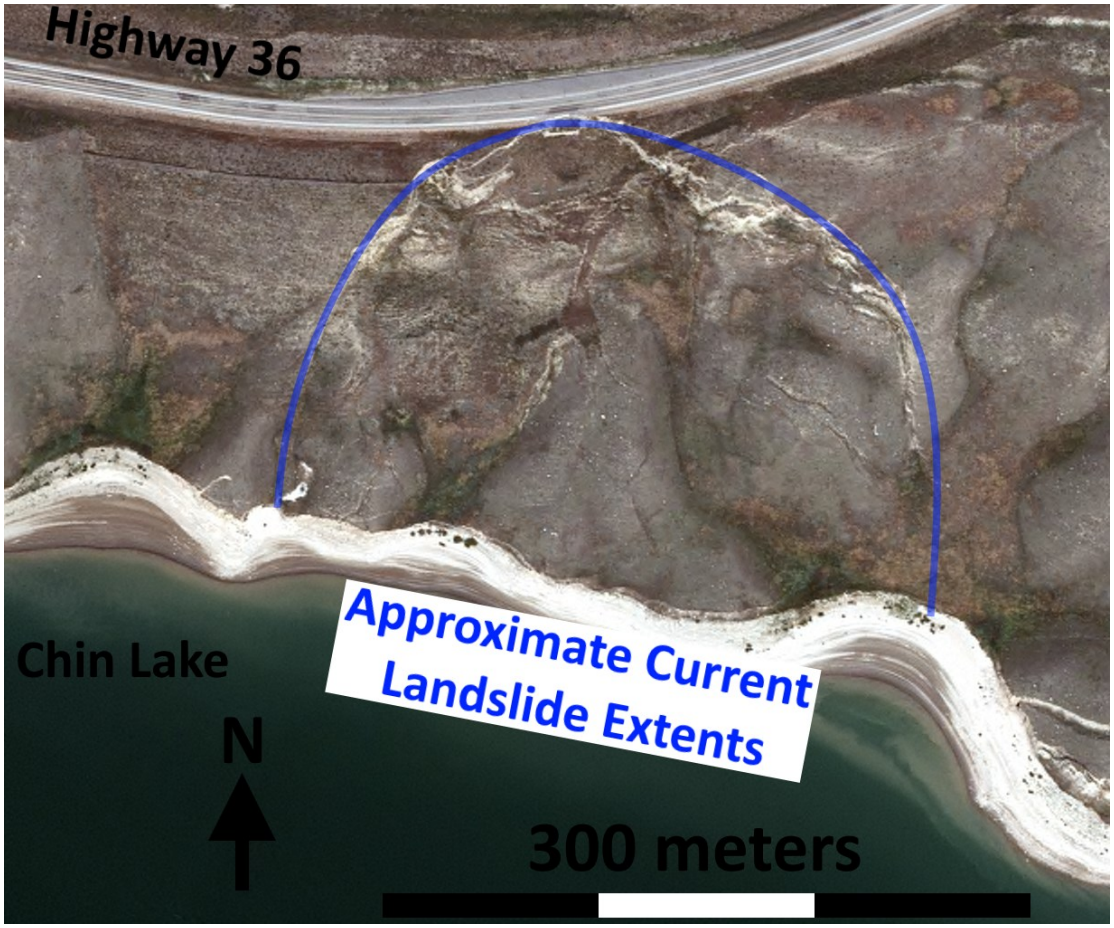

Figure 3-2: Historical air photo of the Chin Coulee landslide from 2012 (Alberta Air Photo Library 2012)

3.2 Landslide Characteristics

The Chin Coulee landslide spans a vertical distance of roughly 55 m from the current headscarp to the reservoir. The landslide tapers from approximately 350 m at the reservoir to 80 m at the headscarp. The landslide has an average slope angle of 13°, although the surface profile is significantly steeper near the headscarp than the toe (See Figure 3-4) (Golder and Associates 1998). The landslide volume is estimated to be 2 million cubic meters.

Reports conducted by Golder and Associates, AMEC, and AMEC FW suggest a maximum rate of retrogressive movement of 5 mm/year, with alternating periods of movement and dormancy

since 1998 (AMEC FW 2015). Movement rates within the active body of the landslide are believed to differ from the retrogressive displacement.

The main failure surface of the active landslide body is believed to exist within a highly fractured shale body layered with coal seams (AMEC FW 2015). This failure surface is quite deep, 32 m below ground at borehole GA98-4 and 17 m at borehole GA98-5 (Golder and Associates 1998). Plan and section views are shown in Figure 3-3 and Figure 3-4.

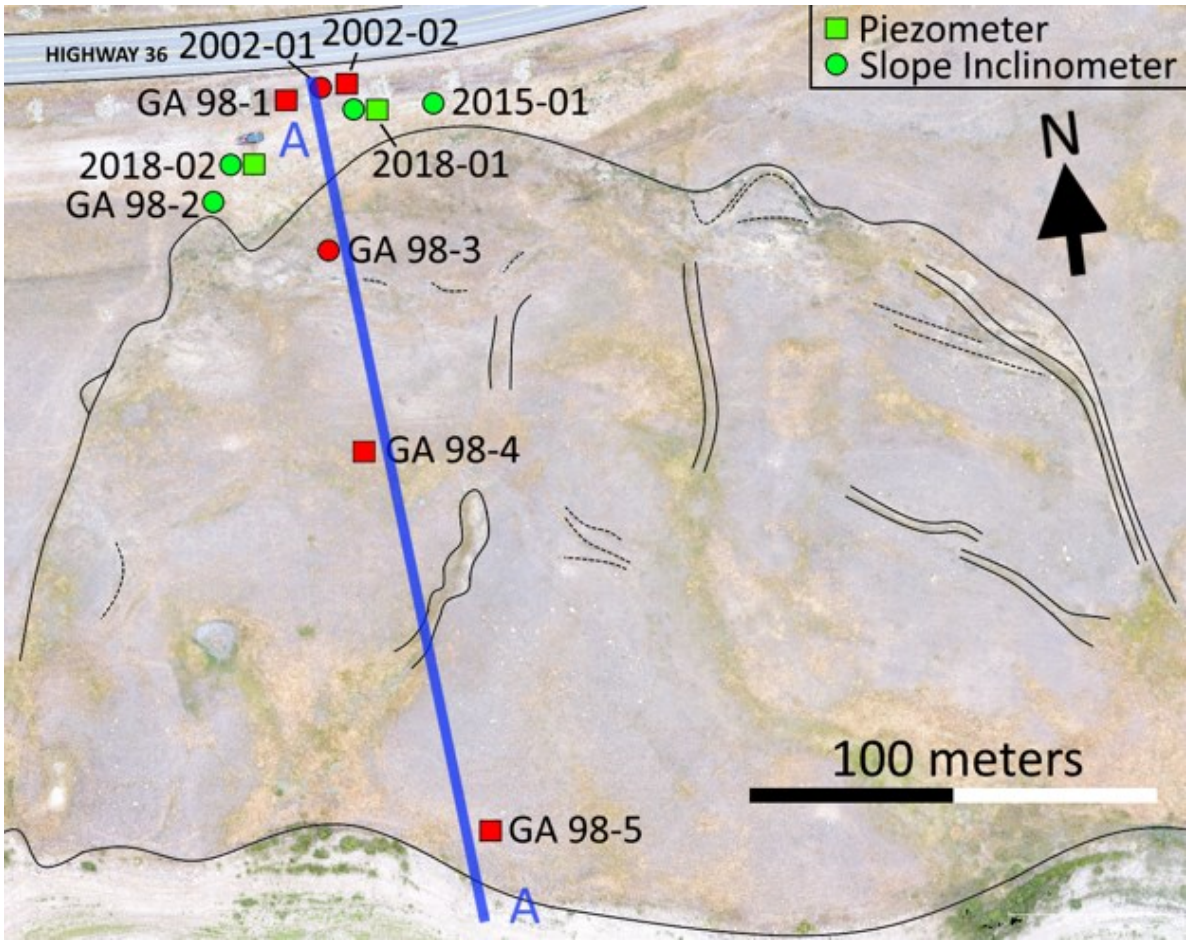

Figure 3-3: Current landslide extents and locations of slope inclinometers and piezometers (Green are currently functional, red are non-functional) (Base imagery from UAV flight conducted on August 23, 2018)

3.3 Geology of the Area

The Chin Coulee valley is a glacial meltwater channel cut into a Foremost Formation bedrock (Fenton et al. 2013; Prior et al. 2013). This formation is a stratigraphic unit of the Late Cretaceous and the basal unit of the Belly River group.

Local site geology is based on borehole logs conducted during instrumentation installations by Golder and Associates in 1998. Local bedrock is consistent with Foremost Formation bedrock and consists primarily of relatively thin and discontinuous layers of grey, low to non-plastic sandstone, grey, clayey, and calcareous siltstone, and brown and grey silty shale of medium to high plasticity, with some coal seams present in some layers. Highly fractured shales and coal seams were observed in boreholes GA98-5 and GA98-4 at depths of 17 and 32 m respectively.

Surficial material is classified as brown to grey clay till, low to medium plasticity, silty, very stiff to hard, with traces of fine gravel and sand lenses, some of which conduct water. Till layer thickness varies from 35 m at the headscarp to 20 m at the toe of the slope. In some of the boreholes, blocks of weathered bedrock were found within the clay till material, suggesting overriding. Evidence of slickensides within the till was found at a depth of 28 – 29 meters during drilling of GA98-3 (Golder and Associates 1998). The slickenside was found to be a high plastic clay.

Surficial clay fill materials are present near the headscarp, originating from infilling during highway construction and realignment. The clay fill is brown-grey, stiff to very stiff, medium plasticity, with some silt, and oxidized.

The geology of the landslide is relatively well known within cross section A-A shown in Figure 3-3 (See Figure 3-4 for a typical cross section).

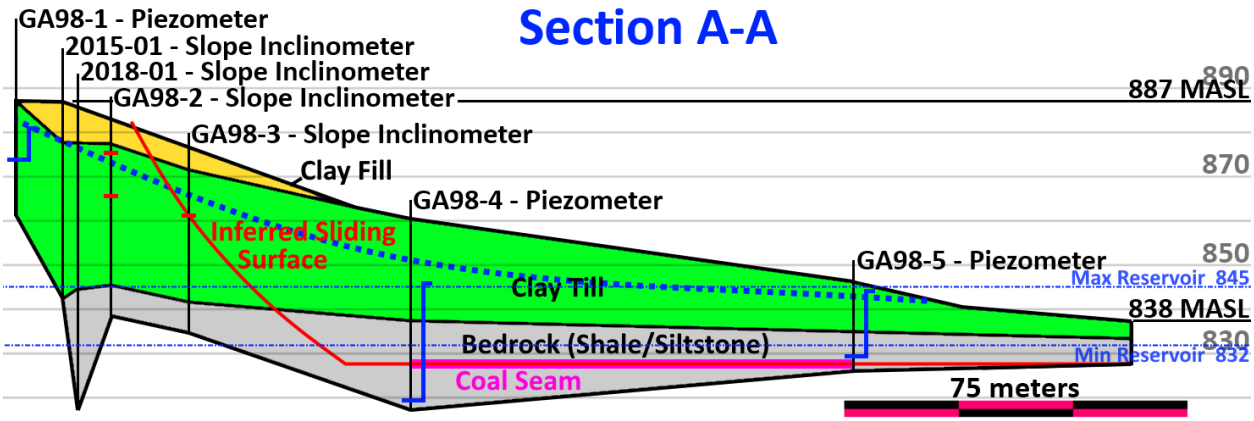

Figure 3-4: Chin Coulee stratigraphy along section A-A from Figure 3-3

3.4 Material Properties

In 2015 several material property tests were conducted on samples taken from borehole 2015-01 (See Figure 3-3). Tests were conducted on material near the surface in the clay fill, as well as the clay till material below. The tests conducted were: moisture content determinations, Atterberg Limits testing, grain size distribution determination, direct shear testing, and consolidated undrained (CU) triaxial shear strength testing. A summary of these results is shown in Table 3-1 (AMEC FW 2015).

In-situ moisture content of all tested materials were below the recorded plastic limit. As the shrinkage limit was not tested it is not possible to determine if these soils are in the solid or semi-solid state. Soils below the plastic limit will not deform plasticly, leading to a more brittle failure when loaded.

Numerous reports outlining typical clay fill and clay till properties, including laboratory testing (Ruban et al. 2004; Su 2005; Stantec Consulting Ltd. 2010) and estimations based on clay fraction content (Skempton 1985) suggest that the properties shown by AMEC FW's laboratory results are typical for clay fill and clay tills within Alberta.

Table 3-1: Clay Till and Clay Fill soil properties on Chin Coulee (AMEC FW 2015)

Characteristic	**Clay Fill**	**Clay Fill**	**Clay Till**	**Clay Till**	**Clay Till**
Depth of Sample (m)	3.2	4.6	10.0	14.0	15.2
In-situ Moisture (%)	11 – 19	-	12.8	10 – 20	10 – 20
Liquid Limit (%)	38.7	-	-	45.7	28.9
Plastic Limit (%)	21.7	-	-	21.6	16.0
Bulk Density (kg/m^3)	2097	-	2184	-	-
Clay Fraction (%)	-	26	25	-	-
CU Triaxial, Peak Friction Angle (°)	27.5	-	-	-	-
Direct Shear, Peak Friction Angle (°)	-	-	25.6	-	-
Direct Shear, Cohesion (kPa)	-	-	21.5	-	-

The soil properties determined by AMEC FW during laboratory testing are likely representative of a non-disturbed soil due to the expected depth of the failure surface being considerably deeper than the depth of sampling. Soil samples within the shear zone of the landslide would show soils at residual friction angles with little to no cohesion.

No sampling and testing was performed on the shale bedrock materials as the focus of AMEC Foster Wheeler's investigation was on the retrogression of the upper clay fill and clay tills.

Additional boreholes and laboratory tests at the depth of the failure plane within the shale material would be required to obtain definitive properties for intact and residual shales.

Numerous investigations into shales and residual shale properties in the Foremost Formation in Southern Alberta have been conducted, including reports from the Prairie Farm Rehabilitation Administration and Golder and Associates (Prairie Farm Rehabilitation Administration 1986; Golder Associates 2002). Based on these reports, cross-bedding strength of intact foremost formation shale can be estimated at 30 – 33 degrees, with 0 kPa cohesion. Residual strength parameters can range from 7 – 13 degrees, with 0 kPa cohesion.

AMEC FW completed a back analysis using an intact shale friction angle of 30 degrees and 0 kPa cohesion to estimate an 8 degree residual shale friction angle along the failure plane (AMEC FW 2015). These results match with the expected range for shale residual strength.

3.5 Climate and Groundwater

The Chin Coulee landslide is located in a semi-arid climatic region. Precipitation and weather data provided by Alberta Climate Information Services was collected from surrounding weather stations in Barnwell, Fincastle, and Wrentham (Alberta Climate Information Service 2019). The location of these three weather stations relative to the landslide is shown in Figure 3-5. Weather data was averaged to determine approximate weather conditions on the landslide itself. The site experiences average daily summer highs of 23°C and winter lows of -14°C. Monthly precipitation peaks in June, with an average monthly precipitation of 98 mm. Yearly precipitation is 360 mm on average.

Standing water within boreholes, regions of moistening soil, and piezometer information show similar water levels within the landslide. Piezometers installed in separate layers within borehole 2002-2 (See Figure 3-3) indicate relatively similar water levels, suggesting that the piezometric level does not vary significantly throughout the various layers within the slope. Based on piezometer data, it is believed that there is a single piezometric level throughout the slope.

Daily reservoir elevation information during the Spring, Summer, and Fall months was provided by Saint Mary's River Irrigation District. Data collection began in 1994 and is ongoing. This information was used to determine the maximum and minimum water elevations that could be expected to occur at the toe of the landslide for stability modelling.

Figure 3-5: Location of three weather stations averaged for weather data on-site (Google Earth 2015)

Piezometers on site indicate that the groundwater depth typically varies from an average of 2 m below ground level near the landslide toe to 6 m below ground level near the headscarp. The groundwater flow pattern is into the valley from the surrounding higher plains, with rainfall and agricultural water feeding back into the reservoir.

Historically, large amounts of movement have been associated with periods of above average precipitation (AMEC 2000). The landslide region may be located on a valley slope drainage gully, which has been blocked and infilled due to highway realignment in the mid 60's (AMEC 2004). Erosional gullies are also present on the landslide surface, indicating surface water flow. The correlation between weather and movement is discussed in further detail in Chapter 8.

3.6 Chin Coulee History

The Chin Coulee reservoir sits within a historical glacial drainage channel. Water levels through the channel were historically very low to nonexistent until the gully was dammed and filled for irrigation water storage (AMEC 2009). Highway 36 was originally located along the valley floor prior to relocation in the mid 1950's. Highway 36 was realigned again in the mid 1960's.

The Chin Coulee landslide first showed signs of movement in 1978, but Alberta Transportation only began continuous monitoring in 1998 after significant undermining of the downslope lane of Highway 36 was observed in 1997. In June of 1998 Golder and Associates installed 2 slope inclinometers near the headscarp of the landslide, GA98-3 and GA98-2, with depths of 42.0 m and 54.4 m respectively. In October 1998, GA98-3 was found sheared at a depth of roughly 15.5 m (Golder and Associates 1999). In June 2000, GA98-2 was found sheared at a depth of roughly 44.6 m (AMEC 2000). Data collection was continued in GA98-2 until the present and shows movement at depths of 8 – 9 m and 33 m (See Figure 3-6) (AMEC 2014).

In 2002 slope inclinometer SI2002-1 was installed north of Highway 36. In 2013 it became unreadable (AMEC 2014). Little movement was historically recorded in this slope inclinometer as it was outside the active extents of the landslide and not sufficiently deep to intercept the deep-seated failure plane (AMEC FW 2015).

In 2015 slope inclinometer 2015-01 was installed in the previously occupied eastbound lane to monitor slope retrogression (AMEC FW 2015). Slope inclinometer 2015-01 extends to a depth of 42 m, insufficient for identifying the deep-seated failure plane. No data has been recorded from SI2015-01 due to excessive movement in the first few meters of casing.

Recorded movements in operational slope inclinometers have been small, ranging from 0 – 5 mm/year (AMEC FW 2015). None of the existing slope inclinometers extend to a sufficient depth to capture movement along the deep-seated failure plane. Surficial damage to the highway also progresses relatively rapidly despite the low levels of movement recorded. Guardrail undermining and tension crack formation in the road surface appeared only 3 years after regrading in 2008 (AMEC 2011).

In 2018 two additional slope inclinometers extending to depths of 70.1 m were installed (KCB 2018). Limited data for these slope inclinometers was available at the time of publishing. These slope inclinometers are installed above the active zone of movement and are primarily for monitoring slope retrogression.

The value of historical instrumentation on Chin Coulee is limited due to the piecemeal nature of the data and the limited extents of the instruments. No installed slope inclinometers have been able to record movement along the expected critical slip plane of the landslide due to their installation locations and depths.

Figure 3-6 shows the trend of movement for slope inclinometer GA98-2 from September 25, 2008 to October 17, 2012. The primary shear zone in this SI is at 8 m depth and represents a shallow failure surface that has emerged from slope retrogression. AMEC plotted the cumulative displacement at this depth from 2009 to 2016, shown in Figure 3-7. More recent years indicate that displacements are very small to non-existent.

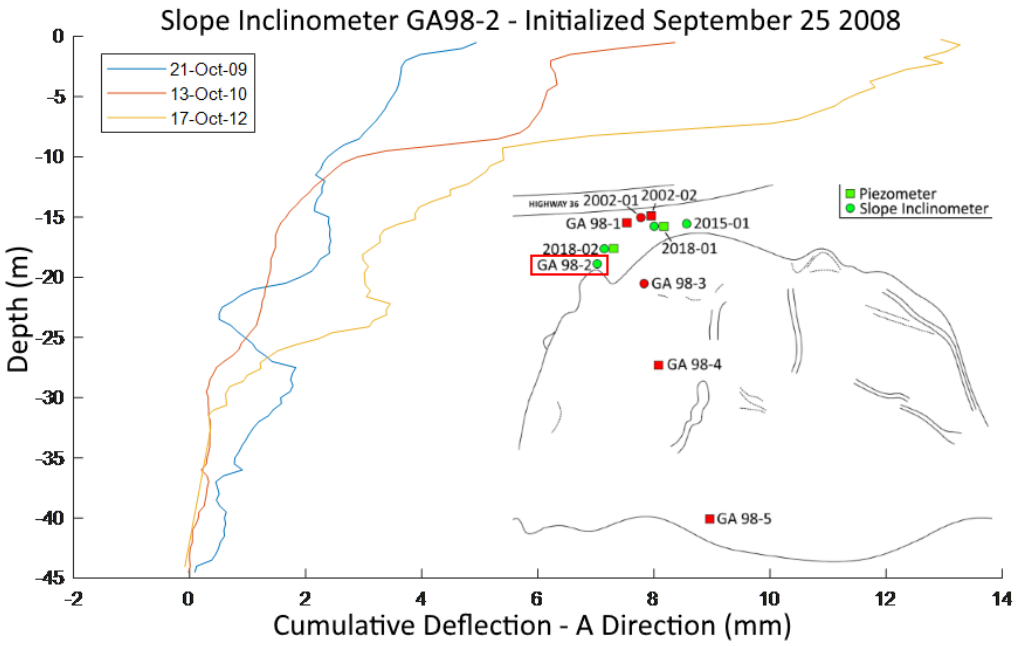

Figure 3-6: Slope inclinometer GA98-2 - Cumulative deflection in A direction (Downslope) (Modified from AMEC 2014)

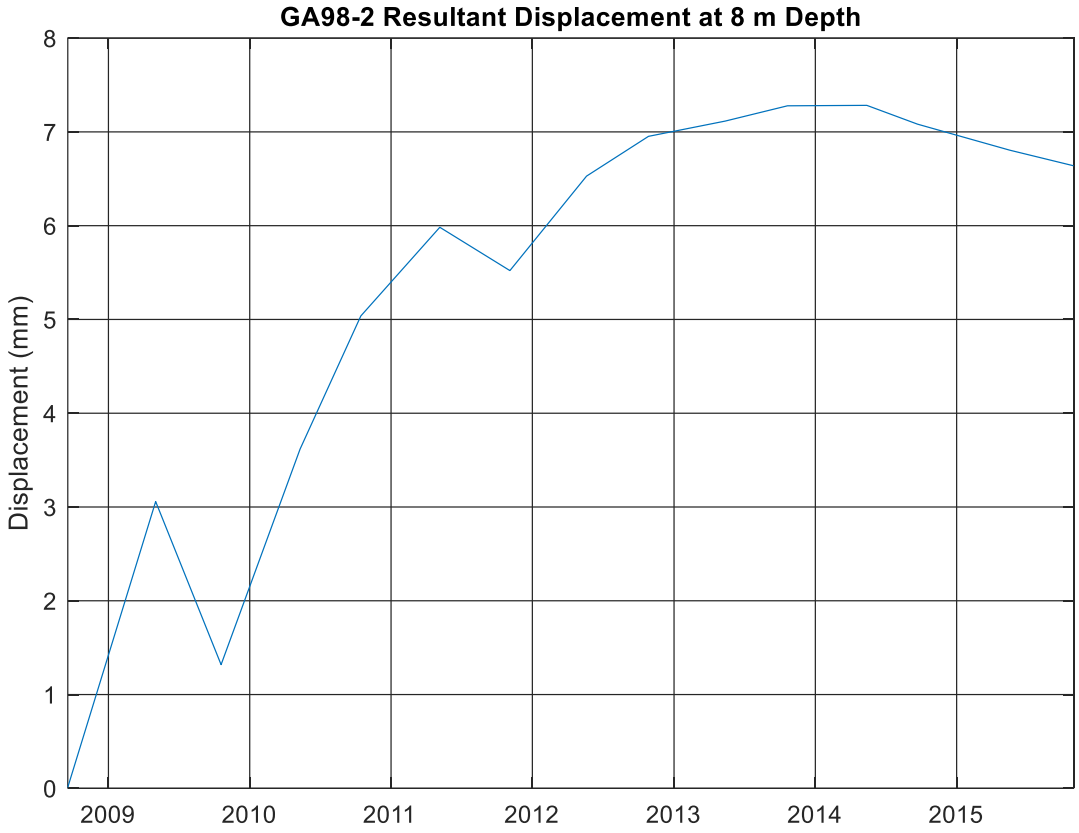

Figure 3-7: Cumulative displacement at 8 m depth in slope inclinometer GA98-2 (Modified from AMEC FW 2015)

4.0 Use of Differential GPS at the Chin Coulee Landslide

The rate of deformation within the landslide body and any related temporal trends was unknown due to the limited instrumentation on the landslide itself. The use of a GPS system allows for continuous monitoring of key locations, which complements the LiDAR data collected and allows for monitoring of any potential block movements, surficial displacements within the active landslide region, and allows for observations of temporal movement trends.

This chapter discusses the application of the differential GPS system to the Chin Coulee landslide, outlines the installation and data processing procedure of the Geocube system, and makes observations and recommendations regarding future installations of similar systems on other sites. Discussion and interpretation of results regarding landslide kinematics is performed in Chapter 8.

4.1 Geocube System Description

The GPS system selected for this project was Geocubes^{TM}, which is a differential GPS system created by Ophelia-Sensors. The Geocube system consists of several mobile GPS units which record GPS position and communicate via radio to transfer data back to a coordinator, a central processing and communication unit for the system (Ophelia-Sensors 2019). These GPS units communicate in series, if one connection is established between the coordinator and the GPS cluster, data will be transferred from every connected GPS unit.

One or more “fixed points” are used to improve GPS results, creating a differential GPS system. These fixed points are GPS units installed in a stable location and act to improve the GPS system by collecting and accounting for atmospheric and local errors in the mobile GPS units.

4.2 GPS System Site Deployment

The installation of the GPS system was originally completed in late June of 2018. The fixed point was then moved on July 11th, 2018, marking the beginning of continuous data recording on Chin Coulee landslide (See Figure 4-1).

GPS placement was selected with the intention of covering most sections of the landslide. The placement pattern is shown in Figure 4-1 with one unit located above the landslide headscarp,

two units on the right upper flank, one unit on the left upper flank, and the remaining five units placed throughout the active landslide region.

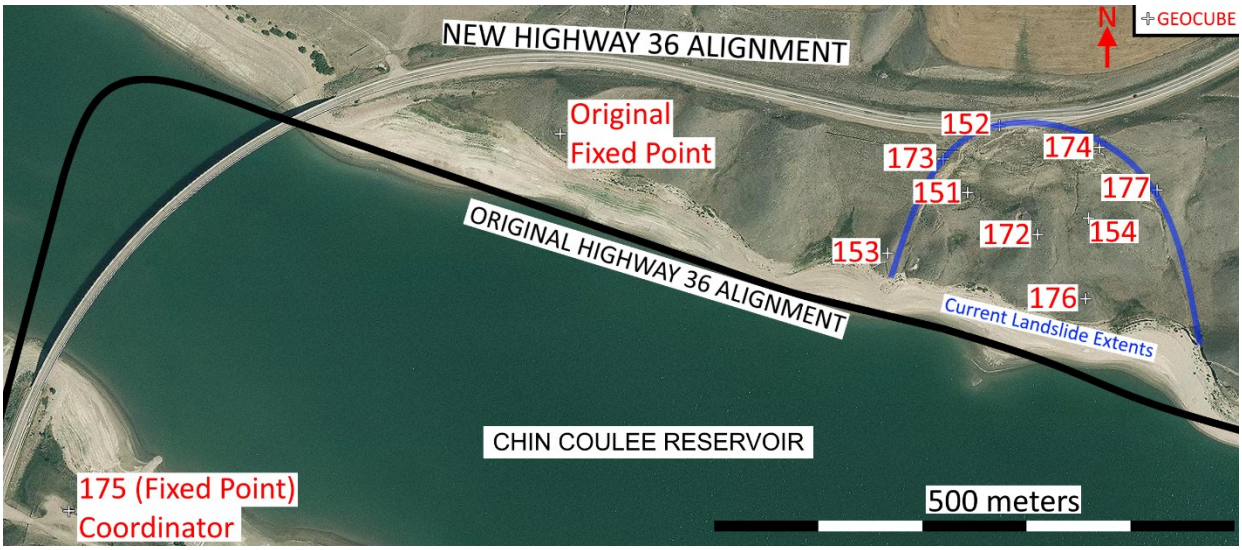

Figure 4-1: GPS unit locations on Chin Coulee landslide (Modified from Deane E. 2019)

4.2.1 Installation Methodology

GPS units were mounted on deck screw piles which were embedded by hand roughly 1 m into the ground. Figure 4-2 and Figure 4-4 shows the installation method of the deck screw piles and final setup employed on Chin Coulee. Figure 4-3 shows an installation on 10-Mile slide for comparison.

Figure 4-2: Chin Coulee GPS deck screw pile installation (Hong 2018)

Figure 4-3: 10-Mile Slide GPS unit final setup (Rodriguez 2017)

Power for the GPS was provided by a 10-Watt solar panel (See Figure 4-4). Two 12-volt, 100 Ah batteries were also installed with each GPS unit to ensure continuous power to the GPS system overnight and during overcast days (See Figure 4-5).

Figure 4-4: Solar panel, GPS unit, and battery box setup on Chin Coulee (Hong 2018)

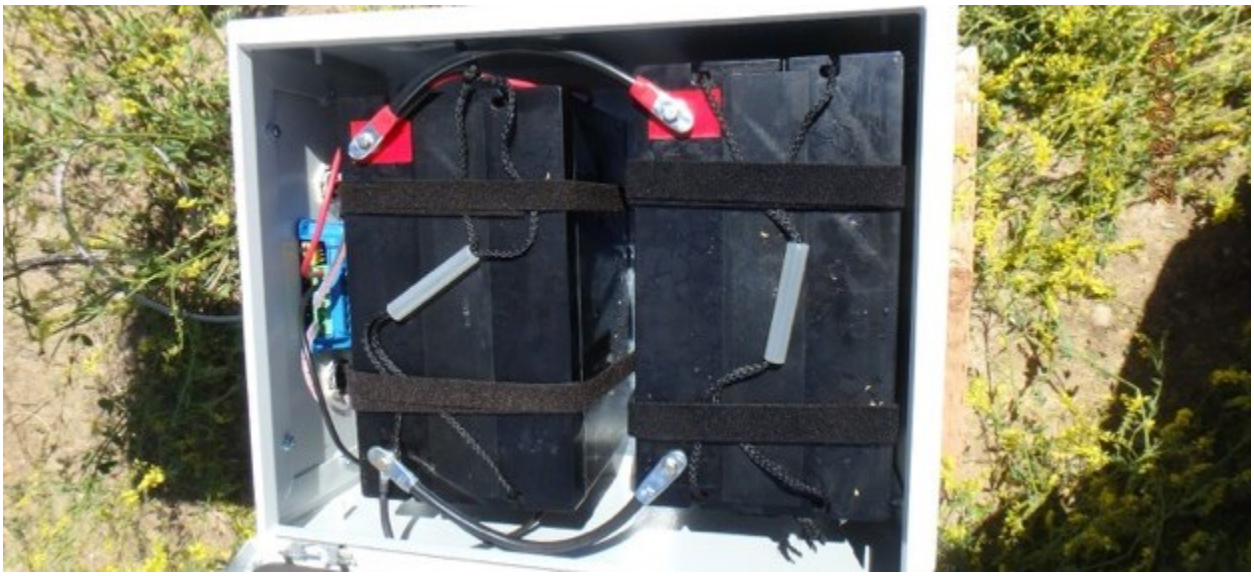

Figure 4-5: GPS battery box and batteries on Chin Coulee (Hong 2018)

4.2.2 Connectivity

To ensure radio connectivity of the system to the fixed point, external antennas were originally placed on the headscarp and the right flank of the landslide and later moved to the bottom of the landslide.

GPS unit 152 at the headscarp repeatedly lost radio signal and failed to connect to the rest of the system. This was corrected by raising the GPS unit to a height of roughly 2 m. Figure 4-6 shows the GPS installation after relocation.

Figure 4-6: Headscarp GPS unit at Chin Coulee after external antenna relocation and raised GPS unit

4.3 Differential GPS Data Processing

4.3.1 Methods and Software

Data collected by the Geocubes was stored within the coordinator which was remotely connected to via the internet to download GPS positional data. Data was downloaded in Latitude Longitude and converted to UTM to calculate displacement directions and magnitudes using MATLAB V2019a (The MathWorks Inc. 2019). The Latitude Longitude to UTM conversion was completed with the use of the MATLAB toolbox GeographicLib V1.49 (Karney 2017).

A modified cumulative horizontal displacement was calculated for each time step using the Easting and Northing values (Equation 1). This modified cumulative displacement is the Euclidian distance from the initiation point to a given time step. Negative displacement is possible, indicating movement back towards the initiation position and often suggests movement rebounding upslope, signifying erroneous results.

A modified cumulative displacement was selected due to compounding movement error. A typical cumulative displacement (Equation 2) calculates displacement over each time step separately and sums the displacement over all time steps to calculate total displacement. As GPS location changes continuously, not accounting for both "negative" and "positive" movements results in artificially inflated displacement magnitudes.

Moving averages were applied to displacement data to return more realistic data. It was found through visual inspection that a 20-day moving average returned the smoothest results while not significantly impacting the resulting trends of displacement. Further discussion regarding data noise is presented in Section 4.4.1.

24-hour standard deviation for all directional and displacement values was calculated for comparison with GPS data collected from 10-Mile slide (See Equation 3).

Equation 1: Modified cumulative displacement

$$Modified\ Cumulative\ Displacement_{t_i} = \sqrt{(X_{t_i} - X_{t_1})^2 + (Y_{t_i} - Y_{t_1})^2}$$

Where X_{t_i} = Easting at time interval i

X_{t_1} = Easting at time interval 1 (Initiation point)

Y_{t_i} = Northing at time interval i

Y_{t_1} = Northing at time interval 1 (Initiation point)

Equation 2: Standard cumulative displacement

$$Standard\ Cumulative\ Displacement_{t_i} = \sqrt{(X_{t_{i+1}} - X_{t_i})^2 + (Y_{t_{i+1}} - Y_{t_i})^2} + \sqrt{(X_{t_i} - X_{t_{i-1}})^2 + (Y_{t_i} - Y_{t_{i-1}})^2} + \cdots + \sqrt{(X_{t_2} - X_{t_1})^2 + (Y_{t_2} - Y_{t_1})^2}$$

Where X_{t_i} = Easting at time interval i

X_{t_1} = Easting at time interval 1 (Initiation point)

Y_{t_i} = Northing at time interval i

Y_{t_1} = Northing at time interval 1 (Initiation point)

Equation 3: Standard deviation of Easting, Northing, or Elevation

$$\sigma = \sqrt{\frac{\sum(X - \bar{X})^2}{n}}$$

Where σ = Standard deviation of Easting, Northing, or Elevation in 24-hours

X = Value of Easting, Northing, or Elevation

$\bar{X}$ = Mean value of Easting, Northing, or Elevation in 24-hours

n = Number of values of Easting, Northing, or Elevation in 24-hours

4.3.2 Results Samples

Horizontal and vertical displacement vector plots from initiation of the Geocube system on July 11, 2018 to July 30, 2019 are shown in Figure 4-7 and Figure 4-8. Vector color signifies the perceived expectation for movement in that direction, with green being expected and red and yellow being less expected. Plots showing 20-day moving average horizontal and vertical displacement are shown in Figure 4-9 and Figure 4-10.

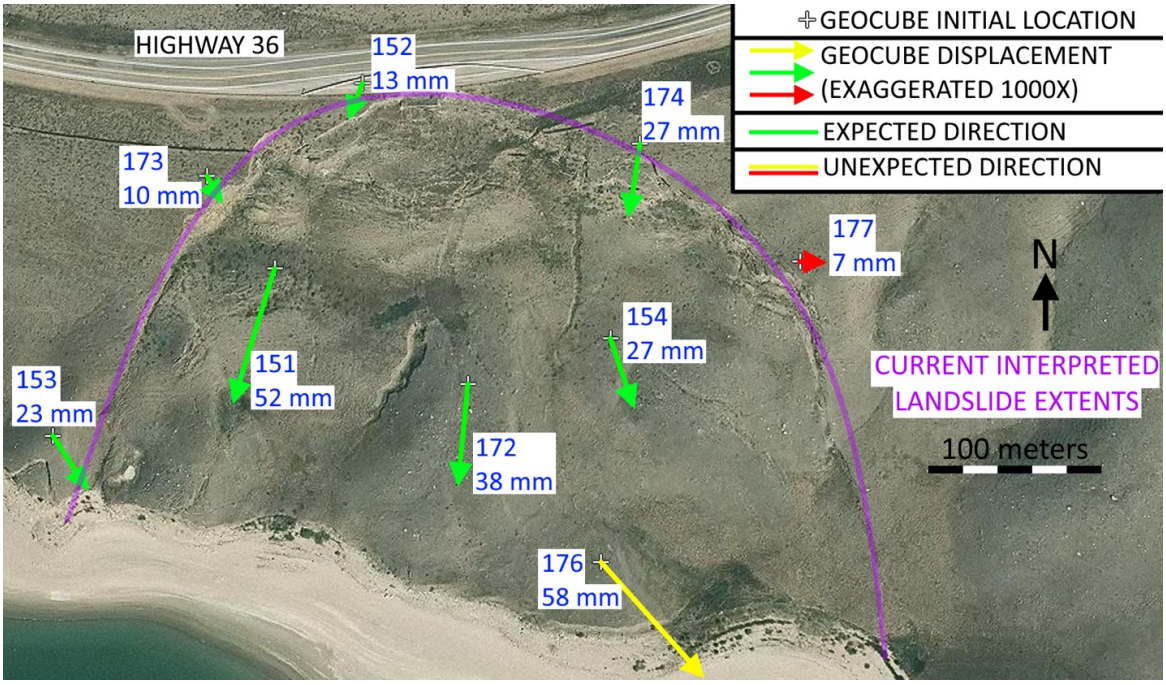

Figure 4-7: Cumulative horizontal displacement vectors of Geocubes (July 11, 2018 - July 30, 2019) (Base imagery ESRI 2019)

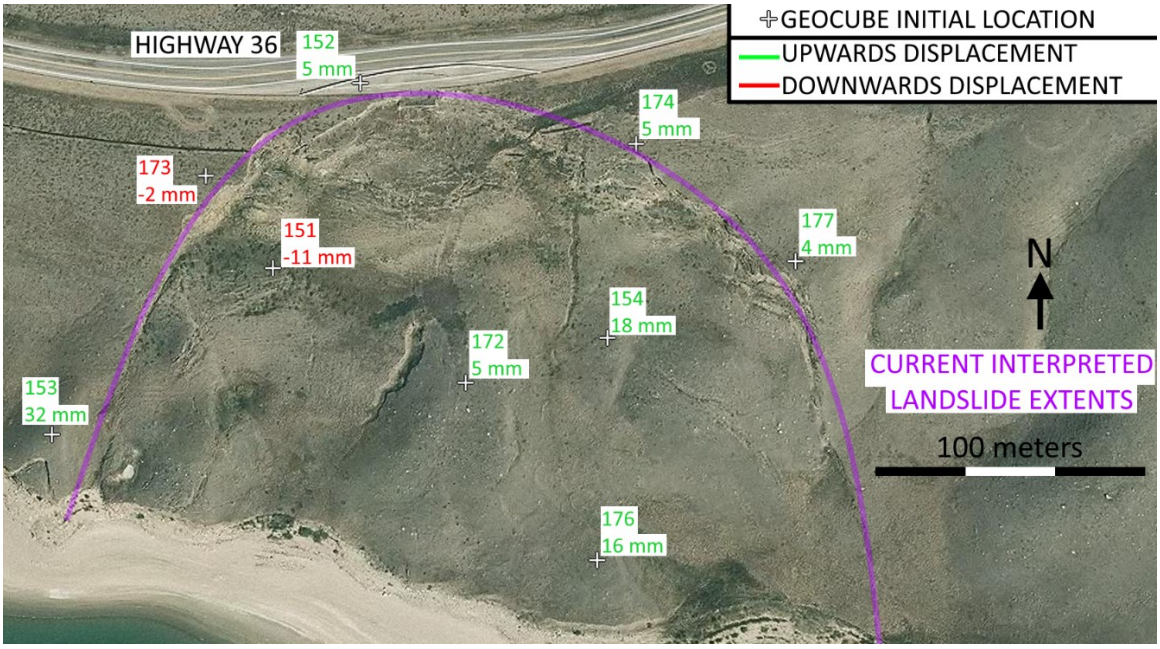

Figure 4-8: Cumulative vertical displacement vectors of Geocubes (July 11, 2018 - July 30, 2019) (Base imagery ESRI 2019)

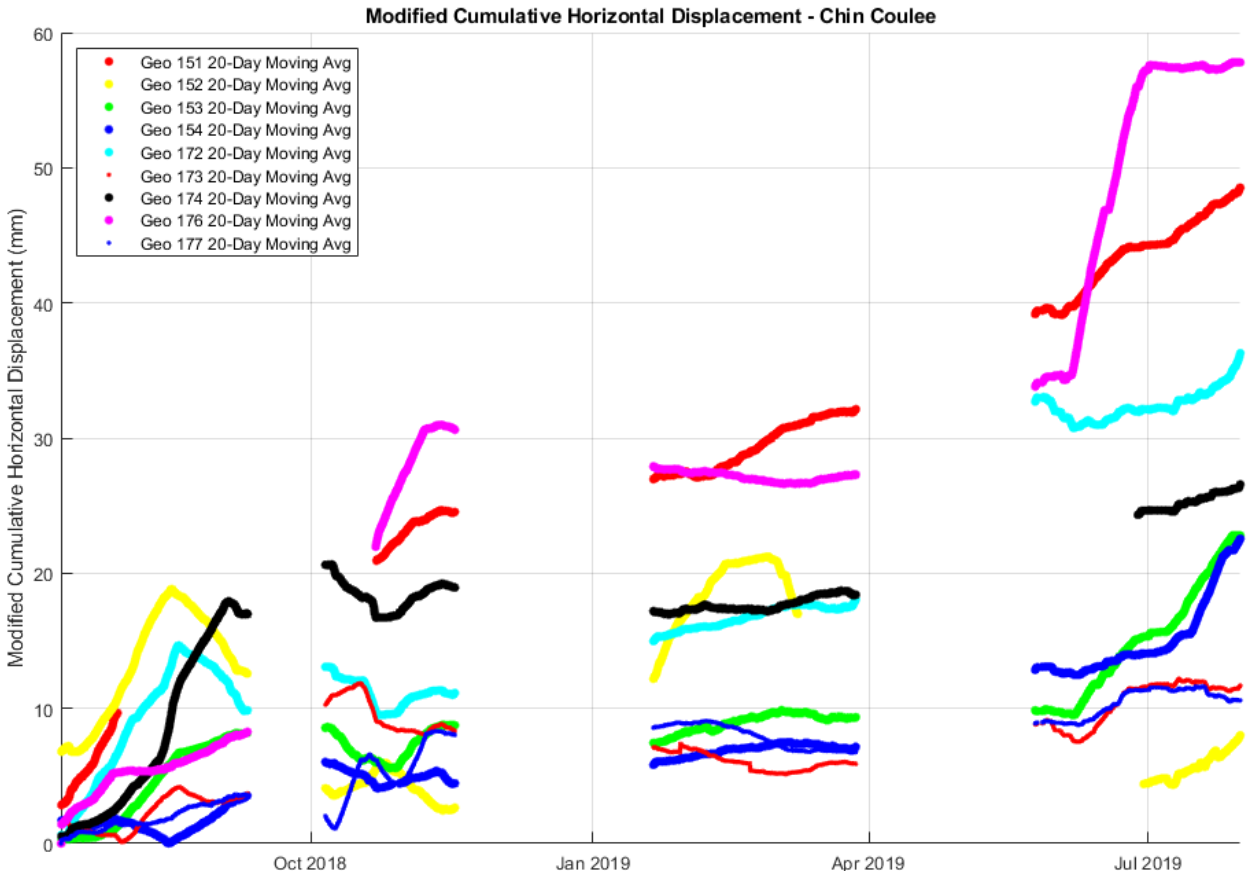

Figure 4-9: Modified cumulative horizontal displacement of Geocubes (July 11, 2018 - July 30, 2019)

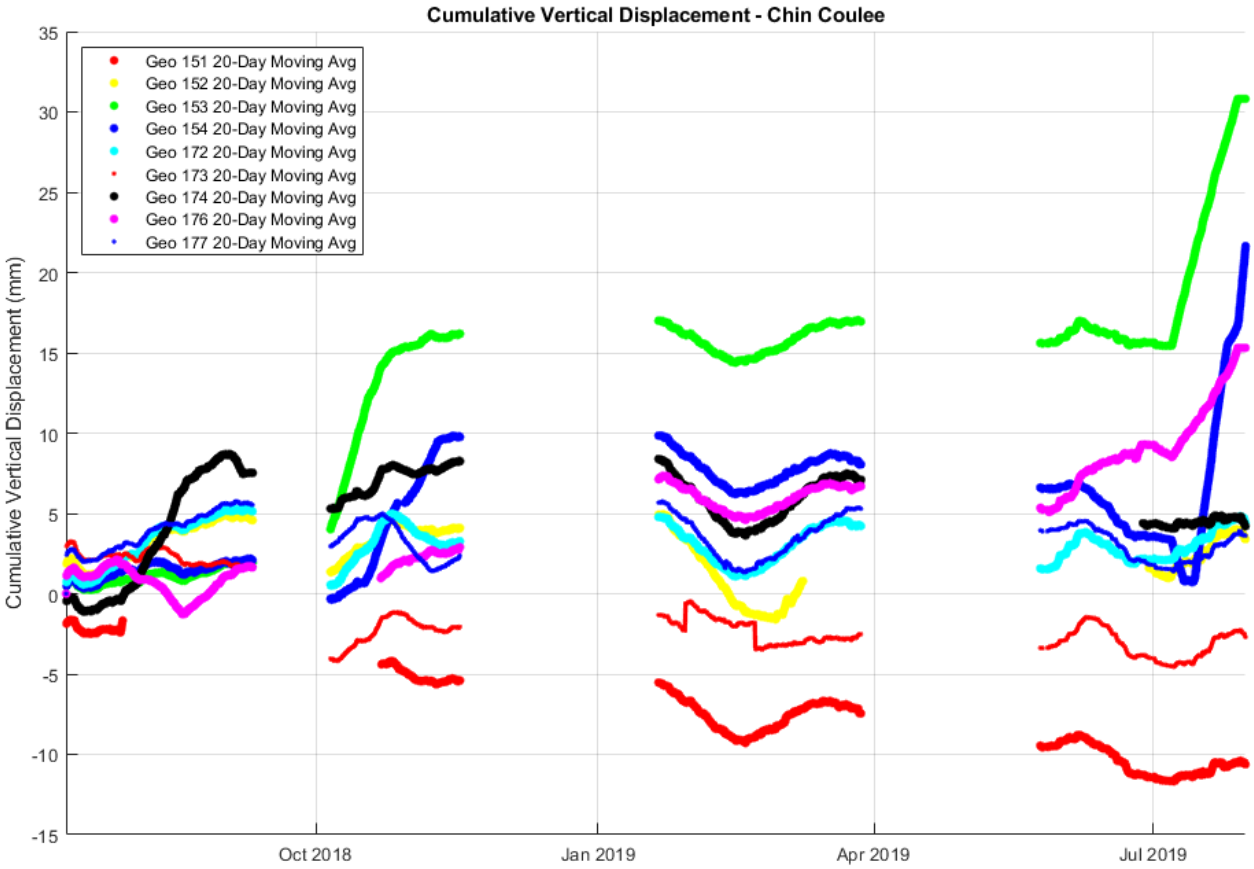

Figure 4-10: Modified cumulative vertical displacement of Geocubes (July 11, 2018 - July 30, 2019)

4.4 Differential GPS Advantages and Limitations

4.4.1 Differential GPS Noise Issues

The 24-hour daily standard deviation was used to quantify the level of error in position of GPS units. A 24-hour time period allowed for increased granularity while including small scale data fluctuations. It also allowed for a comparison to the manufacturer specified error, given as a 24-hour error.

Figure 4-11 shows the 24-hour daily standard deviation of three Geocubes on Chin Coulee and 10-Mile slide, indicated by black scatter points. The standard deviation ranges from 2 – 4 millimeters on Chin Coulee and 1 – 2 millimeters on 10-Mile. The manufacturer specified accuracy for all Geocubes is 1 – 2 millimeters over a 24-hour period (Ophelia-Sensors 2019).

The reduced accuracy on Chin Coulee is likely a result of the fixed point being located roughly 1 km from the mobile Geocubes, reducing the effectiveness of fixed-point error correction. The fixed point on 10-Mile slide was less than 500 meters to the mobile Geocubes.

The ability to discern movement trends from GPS data is a function of the standard deviation and the amount of movement that has occurred. When movement levels are significantly larger than the day-to-day fluctuations in measured location due to error, the error becomes insignificant to the overall movement trend and is unnoticeable even without data averaging. The movement trend of Geocube 46 on 10-Mile slide is visible without data averaging (Figure 4-11C). In contrast, Geocubes 151 and 172 on Chin Coulee show considerable variance when looking at raw data (Figure 4-11 in red) and still show considerable deviance with a 2-day moving average (Figure 4-11 in blue). A 20-day moving average (Figure 4-11 in green) smooths these abrupt jumps and recoils, showing a more physically realistic and possible movement pattern (see Figure 4-11A and B).

Raw GPS data from Chin Coulee is typically unreadable (See Figure 4-11A and B points in red) and averaging must be performed to analyze the data. In general, for GPS data, the level of filtering required depends on the initial quality of the raw data. The ideal level of averaging is one which makes the data readable, without removing short term movement events.

Statistically, the average 24 hour standard deviation of the raw data (Figure 4-11 in red) was calculated at 2.4 mm, with the largest standard deviation observed in Geocube 177 (2.8 mm) and the smallest standard deviation observed in Geocube 153 (1.9 mm).

The average 24 hour standard deviation of the 20-day moving average data (Figure 4-11 in green) was calculated at 0.06 mm (Ranging from 0.039 to 0.097 mm). As the 20-day moving average is the data set being used for analysis for this research, this calculated standard deviation is representative of the error present within GPS measurements for this research.

High frequency GPS systems with low noise (high precision) are not strictly necessary for long term monitoring, but are neccesary for correlating small scale movement events with other phenomena such as specific precipitation or loading events, as they allow for less required averaging. Without high recording frequency, the short term movement event would likely not

be observed due to the temporal spacing of data points. Without high precision, averaging would be required in order to observe the actual movement trend, and this averaging would smooth out any short term movement event. With long term monitoring of larger scale events, such as over the course of a month, even with aggressive data averaging, the correlation between changes in the environment and changes in the GPS data are visible.

Temporally variable 24 hour repeating patterns appear within the Chin Coulee GPS data. These patterns are likely due to changes in satellite position and coverage, as well as ionospheric changes throughout the day. Signal processing, such as a Kalman filters are a common way of improving GPS data, but require additional information regarding the incoming GPS signal not available with the Geocube system (Macgougan 2003; Langley 1997). As a result, only data averaging was applied to GPS data for this research.

Differential GPS systems are precise, but not necessarily accurate systems. For the purposes of landslide monitoring, precision is significantly more meaningful than accuracy. It is not the exact position of the GPS units which are relevant when studying displacement, only the relative position and movement of the GPS relative to itself or a fixed location. In this manner, precision defines how each measurement relates to each other for a specific GPS unit. If a system is precise, given a fixed location, each measurement should return very similar locations, however that location may not be the real position of the GPS unit. Accuracy defines the how each measurement relates to the actual real position of the GPS unit. If a system is accurate, the average location of all measurements should be very close to the real position of the GPS unit, but each individual reading will differ from each other.

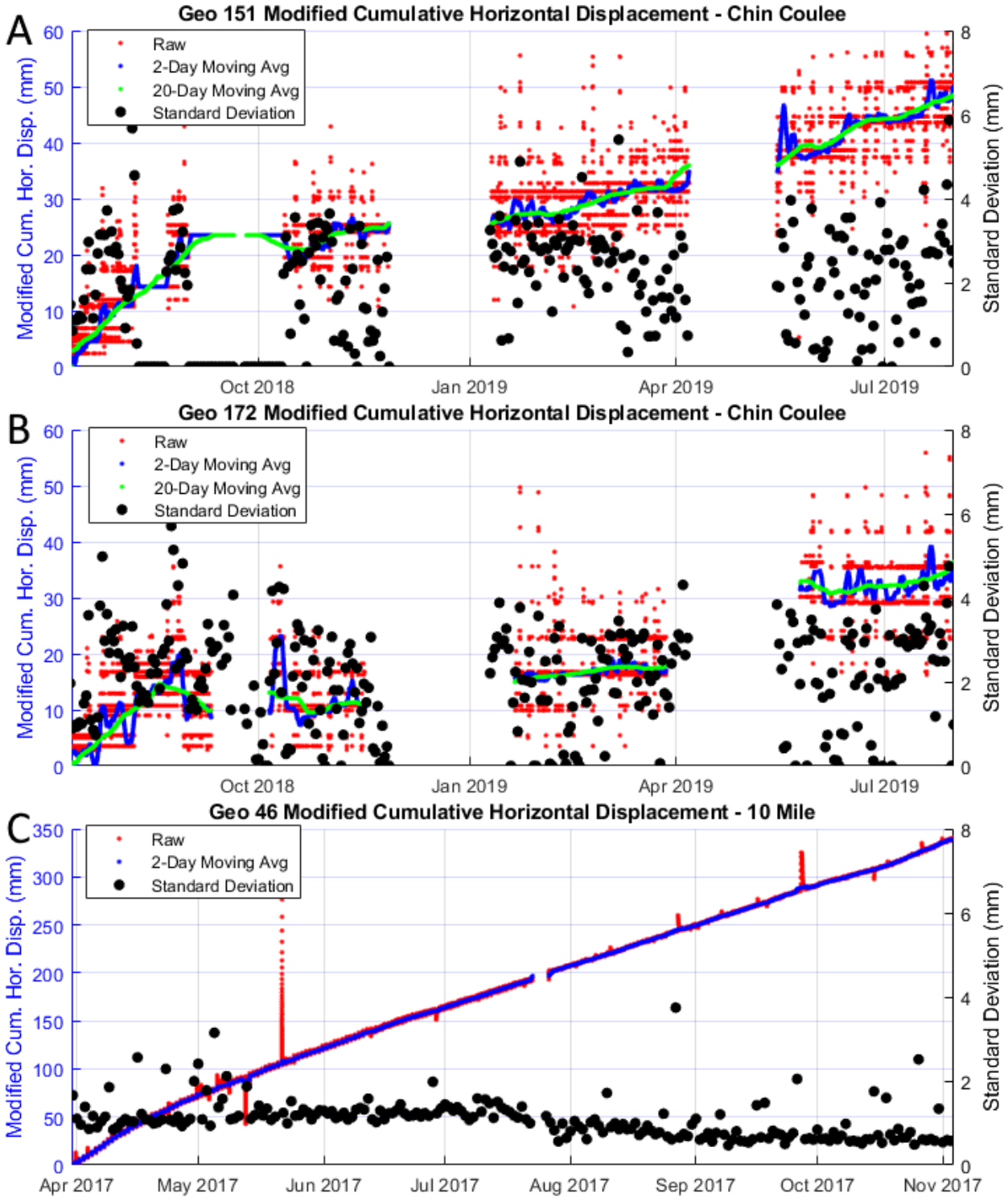

Figure 4-11: Geocube 151 (A) and 172 (B) on Chin Coulee and Geocube 46 (C) on 10-Mile

Data collected from 10-Mile GPS units consisted of multiple monitoring campaigns and had to be stitched together (See Figure 4-12 and Figure 4-11C). The exact position of the GPS unit at the end of one campaign and the beginning of the next did not align due to the error associated with determining the location of the fixed point. The Easting, Northing, and elevation from the end of one campaign was directly matched to the beginning of the following campaign to alleviate this issue.

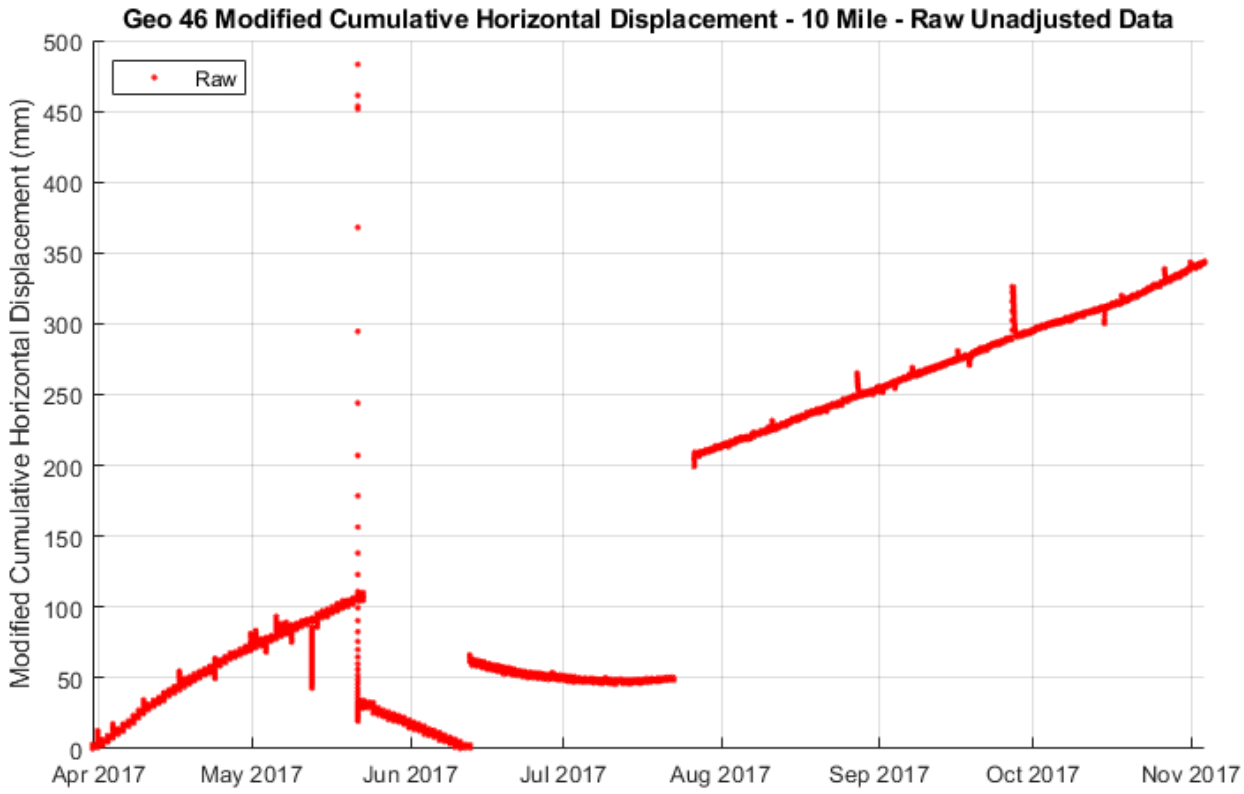

Figure 4-12: Geocube 46 on 10-Mile - Unadjusted data

Chin Coulee data consisted of only one monitoring campaign, and the fixed point remained stable throughout monitoring, so no realignment was required. However, several discontinuities that didn't appear related to ground movement were present (See Figure 4-14). This movement is not believed to be real ground movement as the displacement directions

recorded during these abrupt discontinuities often occurred uphill or in a direction opposite to the continuous movement trend.

Recorded displacement magnitudes when including discontinuities were in excess of 140 mm in some cases, which would have been detected during LiDAR scanning (See Figure 4-15 for comparison to Figure 4-9). LiDAR change detection completed throughout 2018 and 2019 did not detect movement levels of this magnitude during similar time frames.

It is possible that these movements were associated with a sudden release in small sections of the landslide, but vandalism on the site during time periods of the discontinuities suggested external interference (Figure 4-13).

discontinuities present in Geocubes 153, 154, 174, and 176 on Chin Coulee were removed. Removal of these discontinuities involved removing data from before and after the discontinuity and aligning Easting, Northing, and elevation to the same value from before and after the data deletion. Figure 4-14 shows an example of Geocube 154 data before and after discontinuity removal.

Figure 4-13: Vandalism to Geocube on Chin Coulee. GPS and solar panel unscrewed and damaged

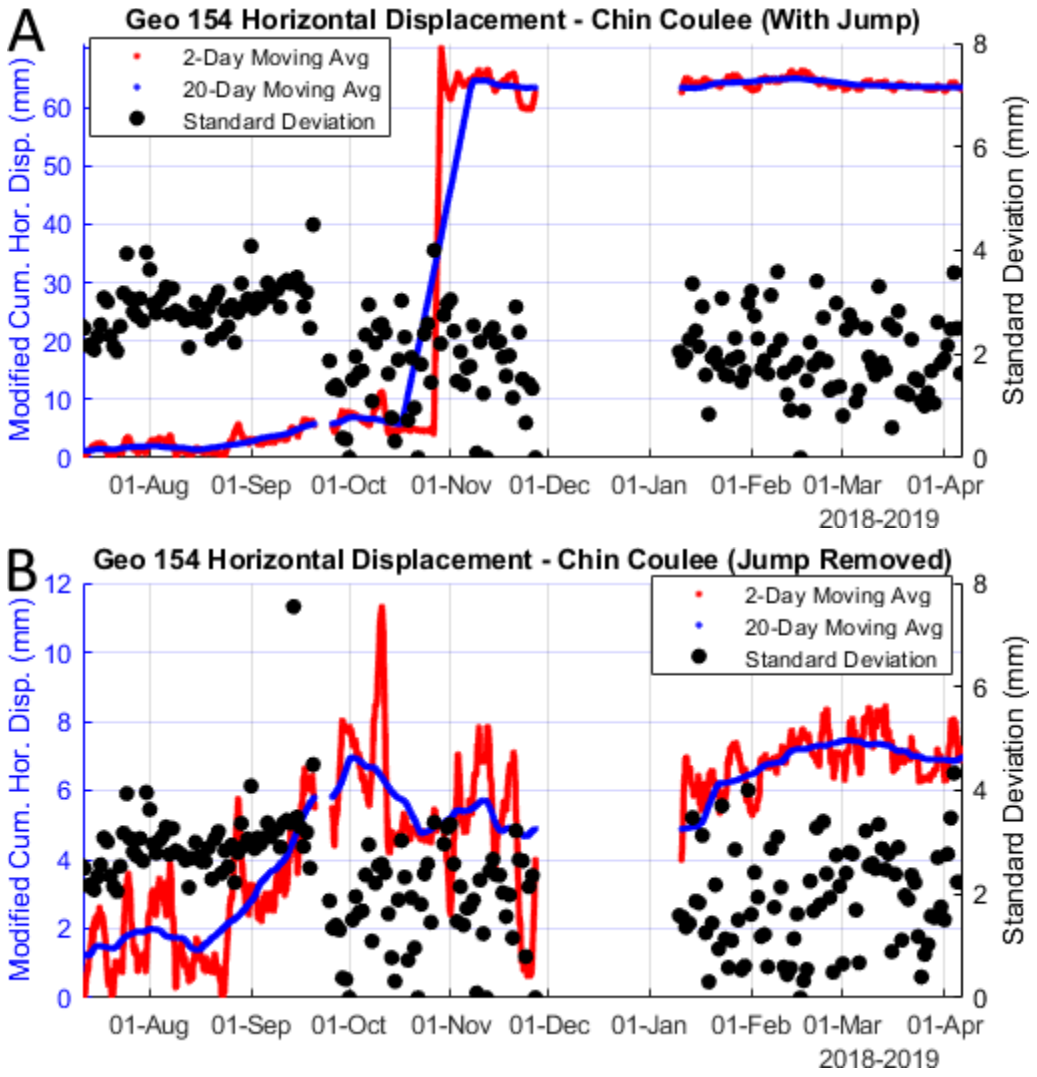

Figure 4-14: Geocube 154 on Chin Coulee before discontinuity removal (A) and after discontinuity removal (B)

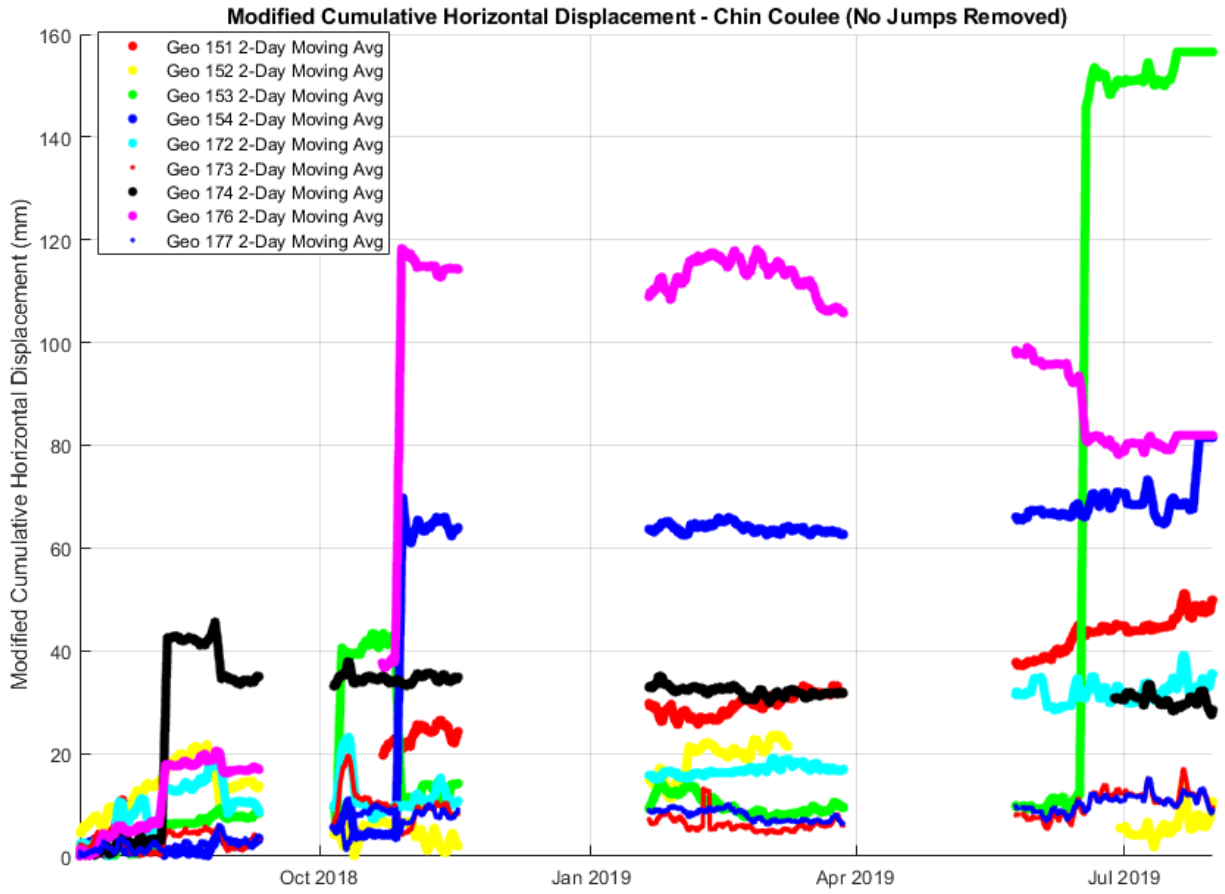

Figure 4-15: Modified cumulative horizontal displacement of Chin Coulee Geocubes without discontinuity removal (July 11, 2018 – July 30, 2019)

Prior to the removal of these discontinuities (Figure 4-16), Geocubes 153, 154, 174, and 176 show movement in unexpected directions, uphill in the case of 153, 164, and 176 (indicated by yellow and red arrows in Figure 4-16 and Figure 4-17). After discontinuity removal (Figure 4-17) Geocubes showed more realistic and consistent displacement directions and magnitudes. Geocubes 151, 152, 172, 173, and 177 experienced minimal to no vandalism and do not appear to show any signs of erroneous discontinuities or displacement directions.

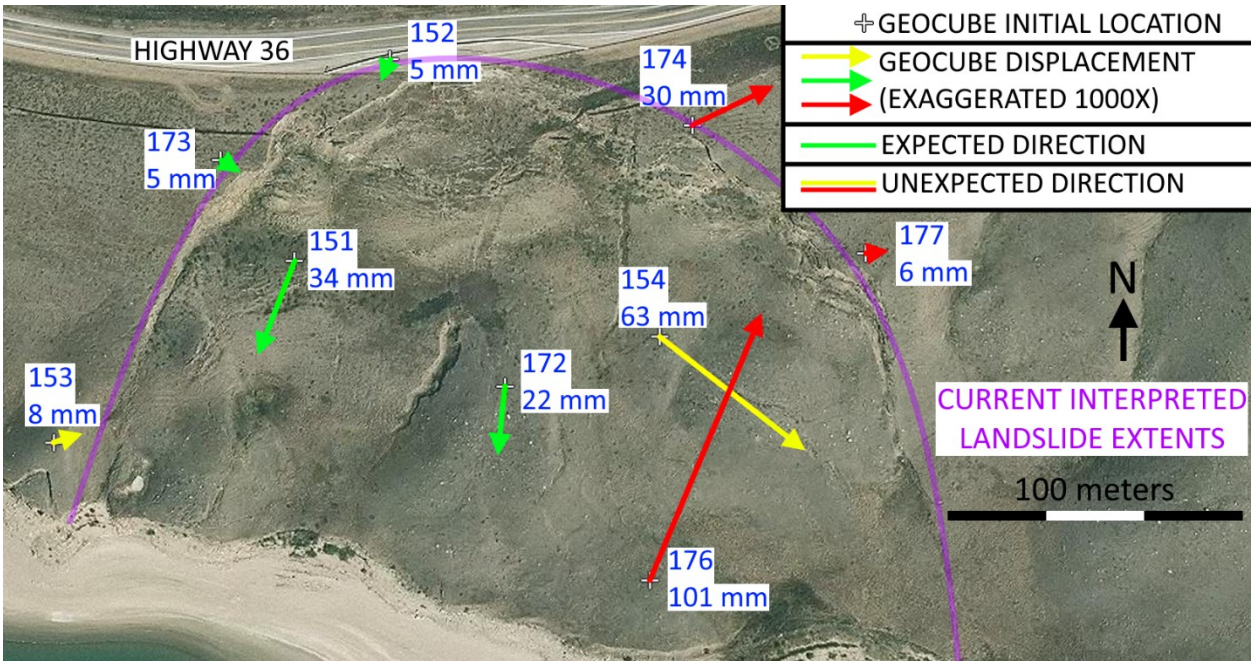

Figure 4-16: Geocube horizontal displacement vectors on Chin Coulee from July 11, 2018 to April 6, 2019 before discontinuity removal (Base imagery from ESRI, 2019)

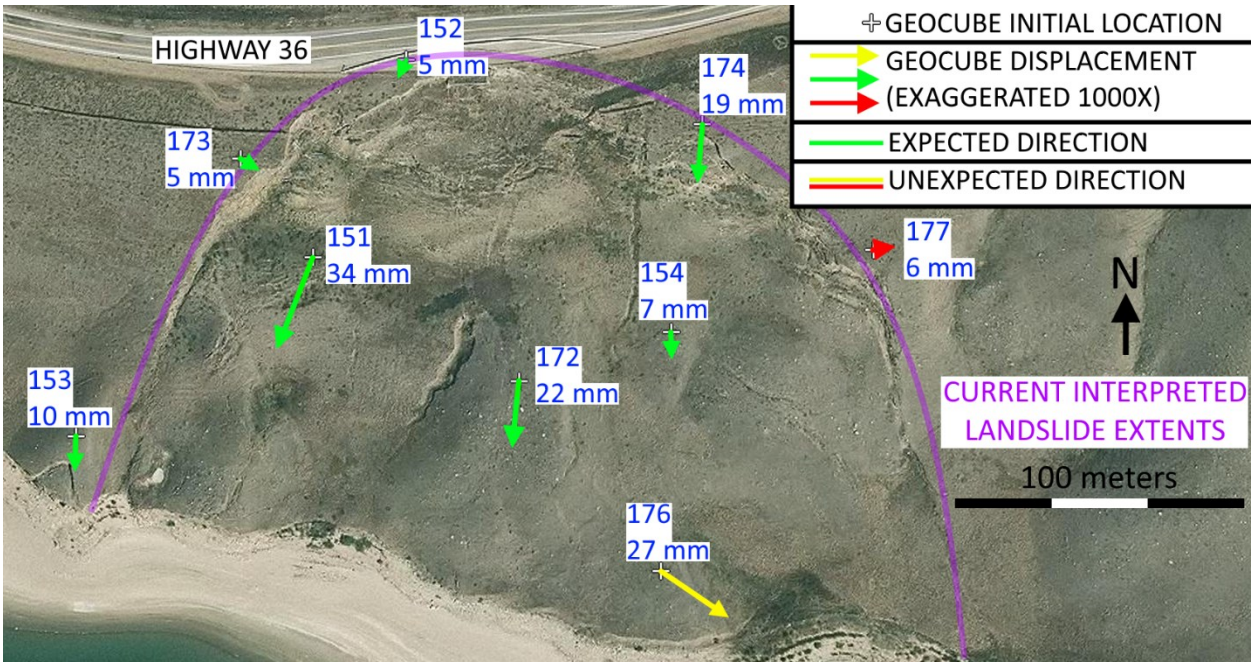

Figure 4-17: Geocube horizontal displacement vectors on Chin Coulee from July 11, 2018 to April 6, 2019 after discontinuity removal (Base imagery from ESRI, 2019)

4.4.2 Differential GPS Installation Method Observations and Recommendations

4.4.2.1 Post Height

Geocubes on Chin Coulee were installed at a height of roughly 1 meter to ensure proper radio signal between GPS units and the coordinator. Geocubes on 10-Mile slide were typically less than 50 centimeters off the ground. A low installation height allows for the GPS unit to more directly correlate with ground movement. Vegetation and multipath errors become a larger concern the lower the installation height. Figure 4-3 shows an example of vegetation growth around a Geocube on 10-Mile.

Tall installation heights lead to increased data noise due to external movement of the mounting pole. For example: A GPS unit that is installed at a height of 2 meters will record a movement of 70 mm when rotating only 2 degrees about the base of the post. As ground movement in landslide regions can often be expressed through rotation, recorded displacements may be significantly overstated, triggering warning systems. Contrarily, GPS movement may be significantly understated, leading to false reassurance regarding landslide safety.

The lowest possible installation height, while ensuring system functionality, is recommended for improving ground movement-GPS movement correlation.

4.4.2.2 Post Installation

Four major problems arose due to the hand augered post installation method employed on Chin Coulee.

- The screw would get stuck in gravel and had to be relocated. This limited the depth of installation as refusal would often arise after only 0.6 – 0.8 meters.
- Posts came in sections of 0.9 meters, limiting the ability to custom fit installation height.
- The top of each section nested into the bottom of the following section poorly. Duct tape was applied around the base of the top of each section to increase rigidity.
- Augering disturbed the soil surrounding the post base. This was alleviated by packing the surrounding soil with nearby rocks and compacting with a sledgehammer.

As installation height is often outside the user's control, improvements to installation methods should focus primarily on post rigidity. Methods which reduce ground disturbance, such as hand driving posts rather than augering would improve results. Rigid 2.5 – 5.0 cm steel round or square posts driven by hand would likely lead to improved results. A deeper embedment depth would also likely help with GPS-ground correlation.

4.4.2.3 Vandalism

Vandalism was a problem on Chin Coulee. Vandalism occurred on numerous occasions to the majority of Geocubes present on site. Some events appear to have impacted the GPS data through erroneous movement, as discussed in Section 4.4.1, while some events brought down the GPS system. Methods for preventing vandalism are often costly and not necessarily effective. 10-Mile slide is under continuous 24/7 lane control and has experienced no vandalism to the system. In contrast, Chin Coulee landslide is easily accessible from Highway 36 and is near several small communities.

4.4.2.4 Gaps in Data

Several large gaps in data are visible throughout the monitoring campaign (See Figure 4-9, Figure 4-10, Figure 4-15 for examples). The Geocube system relies on interconnectivity of the GPS units to transmit data, if the Geocube responsible for transmitting data back to the controller is damaged or disconnected, no data will be collected during that downtime.

The large gaps in September 2018, December 2018, and April 2019 did not appear to be related to vandalism. The cause for these gaps appears to be software related issues with the Geocubes, suggesting that the reliability of the system may pose an issue in future applications. The distance between the controller and the mobile GPS units may also have a factor, as significantly fewer gaps and downtimes were observed on 10-Mile slide.

4.4.3 Minimum Campaign Duration for Differential GPS

The minimum required campaign duration for monitoring with GPS is largely related to the required moving-average window for obtaining an adequate trend. An adequate trend can be defined as a trend in which a stable and consistent movement, free of displacement patterns

which are not physically possible is found. For example, positional fluctuations suggesting movement rebounding up slope repeatedly should not be present.

On Chin Coulee, movement trends can be observed with a monitoring duration of only a few months using a 20-day moving average, however there would likely be little confidence in this trend when extrapolated to longer periods of time. Movement trends vary significantly throughout the season and short-term monitoring would not fully represent annual movement trends. Geocubes located within the active landslide extents have increased movement during the fall months of August and September (54 – 162 mm/yr) and reduced movement during winter months (See Figure 4-18). This may be due to drawdown in the reservoir as well as loss of the buttressing effect due to lowering of the reservoir. The impact reservoir elevation plays in landslide stability is discussed in greater detail in Chapter 8.

To fully understand landslide movement, measurements should be obtained for longer periods of time, often in excess of 1 year, as landslide movement is often related to water conditions. Overland erosional flow, internal groundwater flow resulting in seepage along the slope, and varying reservoir elevation all have an impact on slope stability and vary throughout the year and year-to-year.

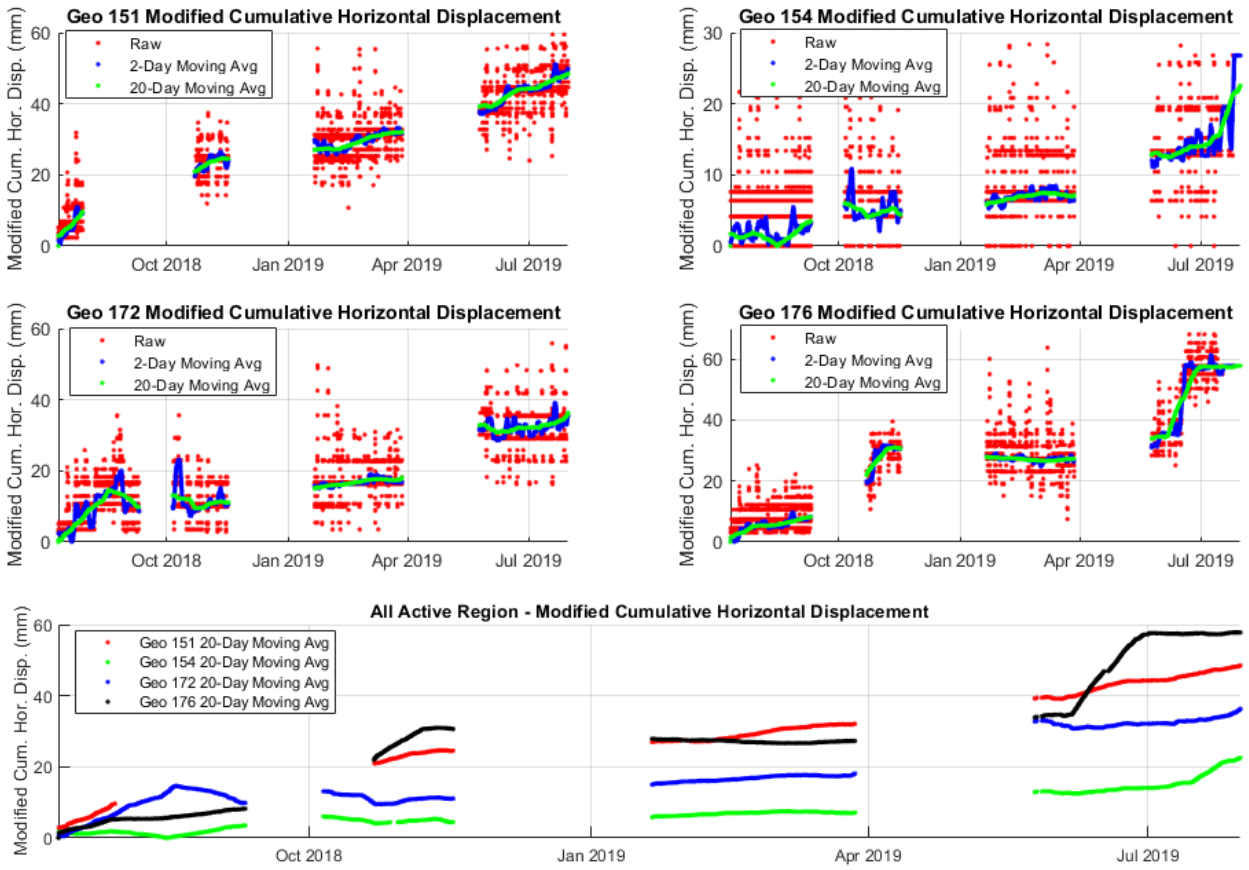

Figure 4-18: Horizontal movement of Geocubes within the active region

4.5 Differential GPS – Summary of Use on Very Slow, Vegetated Landslides

Differential GPS systems offer an affordable and powerful option for continuous monitoring compared to other downhole instrumentation methods, which often require mobilization of expensive equipment. Data can be collected in real time remotely, allowing for the development of early warning systems and remote monitoring of system health.

These benefits apply regardless of the site conditions and movement rates of the landslide, however, under Very Slow conditions, greater care must be taken during system installation. The fixed point should be close to the rest of the system to reduce system error, each GPS unit should be installed low to the ground to ensure close correlation between GPS and ground movement, and the GPS-post system should be as rigid as possible.

Movements in landslides vary throughout the year, due to rainfall, snowmelt, and external factors including reservoir buttressing. These events vary throughout the year and year-to-year. Monitoring should encompass at least one calendar year in order to account for seasonal variations. Additional years of monitoring may be required to make correlations with multiple events. It should be expected that longer durations of monitoring and larger averaging windows will be required when landslide movement levels are smaller. Slower movement means the error in the system becomes more relevant and larger averaging windows are required to observe trends of movement.

Comparing the results of the Geocubes from 10-Mile slide and Chin Coulee landslide, three important lessons were learned:

- Differential GPS installations should ensure that the fixed point is installed as close to the position of the mobile GPS units as possible. The distance to the fixed point has a large impact on the amount of error present within the data and can negatively impact the ability to interpret movements.
- Movements which seem erroneous within GPS data may or may not have an alternative explanation. Erroneous discontinuities may be associated with relocation of the fixed point or deviations in fixed point location, such as on 10-Mile, or these discontinuities may be due to vandalism, such as on Chin Coulee. Adequate justification for these alternative explanations may be difficult and may require frequent site visits.
- Monitoring of a site using only differential GPS is unadvisable, as confirmation of results or dismissal of seemingly physically impossible movement phenomena may not be possible. The limited spatial extents of GPS also limits the ability to fully understand movement mechanics.

5.0 Use of TLS LiDAR at the Chin Coulee Landslide

Terrestrial LiDAR was selected as a monitoring method for the Chin Coulee site due to the ease in which large spatial extents can be scanned at high accuracy. LiDAR complements GPS data by providing discontinuous, but spatially high-density data, while GPS provides continuous, but spatially low-density data. Comparison of GPS and LiDAR also allows for verification of movement through two different modes of measurement.

This chapter discusses the application of LiDAR to the Chin Coulee landslide, outlines the data collection and processing procedure, and makes observations regarding advantages and limitations of LiDAR on Chin Coulee and similar sites. Discussion and interpretation of results regarding landslide kinematics is performed in Chapter 8.

5.1 LiDAR System Description

All LiDAR scanning was performed with an Optech ILRIS-LR laser scanner, running in enhanced range mode. Laser specifications are as follows: laser wavelength of 1064 nm, pulse frequency of 10 kHz, and a beam divergence of 0.014324° (See Table 2-1 for manufacturer comparisons) (Teledyne Optech 2019). All scan Regions of Interest (ROI) were conducted using the last scan option in order to improve vegetation penetration and an approximate ground point spacing of 20 – 30 mm, depending on scanner mean distance to target. The typical LiDAR setup on Chin Coulee is shown in Figure 5-1.

Figure 5-1: ILRIS-LR LiDAR scanner used on Chin Coulee (Location 1)

5.2 LiDAR System Site Deployment

The first adequate LiDAR scan was performed on July 10, 2018 but featured shadows (Regions hidden to the scanner line of sight). Subsequent scans used three scan locations to alleviate this. Figure 5-2 shows the three scan locations. Figure 5-3 shows the typical LiDAR scan profile.

A second scan was performed on August 23, 2018. Change detection between the July 10, 2018 and August 23, 2018 scans determined that movement levels were too low to observe movement within a one-month timespan. The third scan was completed on October 13, 2018 but was notably impacted by high winds and change detection results showed considerable streaks throughout the data. These streaks were believed to be caused by vegetation which was blown by the wind, impacting the last reflection capabilities of the LiDAR scanner. This scan data was discarded. Later scans were completed on May 9 and July 29 of 2019.

Table 5-1 summarizes the completed LiDAR scan dates, as well as notes regarding the overall quality of the scans.

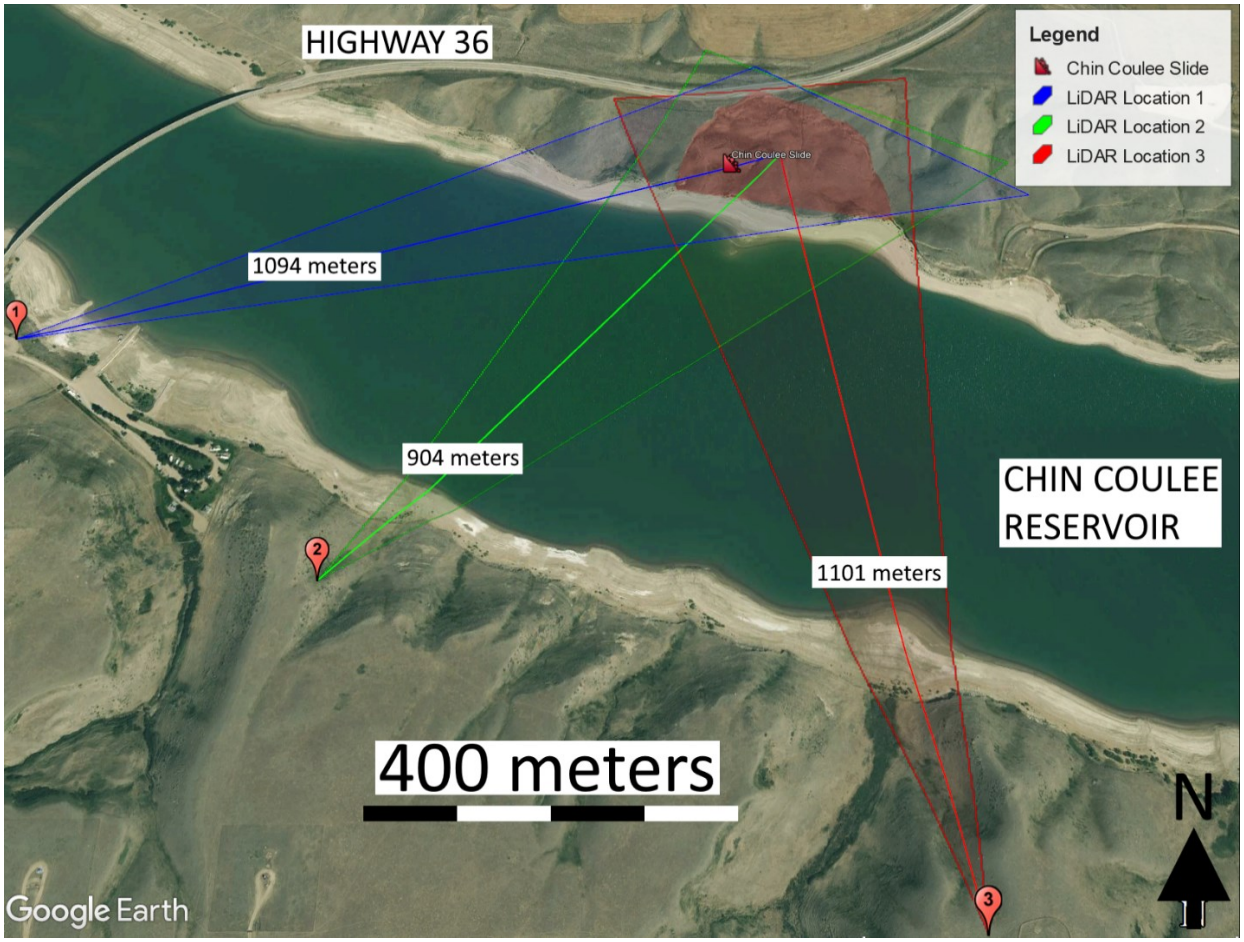

Figure 5-2: LiDAR scan locations on Chin Coulee (Deane E., 2019) (Base imagery from Google Earth 2019)

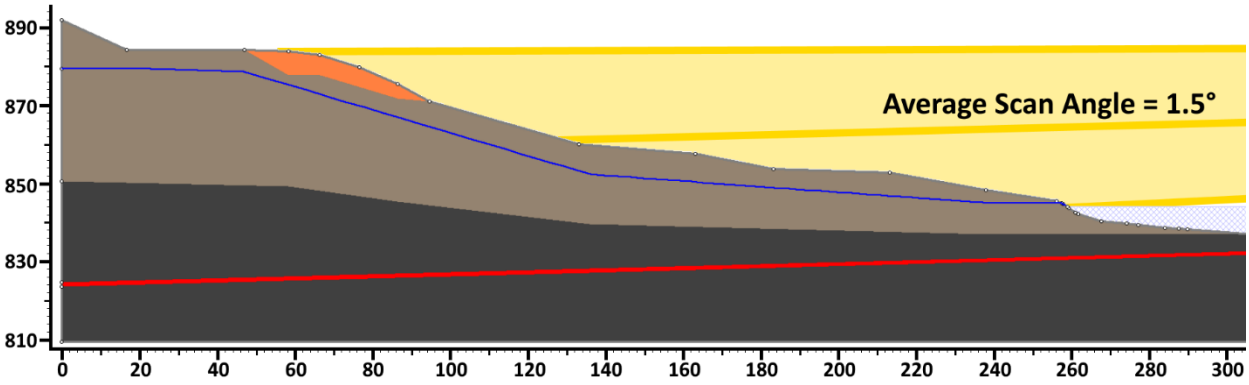

Figure 5-3: Average TLS LiDAR scanning angle profile on Chin Coulee

Table 5-1: Summary of LiDAR scans

Scan Date	Quality	Notes
June 13, 2018	Inadequate	Operator error resulted in corrupted data
July 10, 2018	Adequate	Shadows from only using scan location 1 and 2 (Figure 5-2)
August 23, 2018	Adequate	First scan with all three scan locations
October 13, 2018	Inadequate	Extreme winds (80 km/h) appear to have impacted scan results due to vegetation and movement of scanner during scanning. Banding present within scans (See Figure 5-6)
May 9, 2019	Adequate	
July 29, 2019	Adequate	Last scan performed (See Figure 5-7 and Figure 5-8)

5.3 LiDAR Data Processing

5.3.1 Methods and Software

The typical process for LiDAR scanning and change detection is as follows:

1) Scan from multiple angles/locations to ensure maximum coverage of the target and reduce shadows.
    a. The LiDAR scanner should be set up in the highest available power setting.
    b. All points within an individual ROI should be roughly the same distance away from the scanner to reduce variation between point spacing throughout the scan. ROIs should have roughly 20% overlap for ROI alignment in step 4.
2) Clean the LiDAR data. Areas far outside the area of interest can be removed. Points which appear “floating” in the air should be removed.
3) OPTIONAL: Remove/reduce vegetation for all ROIs to improve the alignment of scan data. For this research, CANUPO classification was used (Brodu and Lague 2012).
4) Align each ROI with iterative closest point (ICP) matching.
    a. To increase ICP matching accuracy, ROIs must be trimmed such that only sections which are intended to overlap remain.
5) Align each LiDAR scan location with a rough point selection alignment.

6) Trim all non-overlapping points for each LiDAR scan location. Areas which are shadows in one scan but not the other should be removed.
7) Combine each LiDAR scan location with ICP matching.
8) Combine all aligned scan location point clouds into one cloud.
9) Steps 1 through 8 should be repeated for each scan timestep for change detection.
10) Align the completed point clouds (Created in step 8) for each time step using a rough point selection alignment. As there is expected movement between the two scans, points selected for rough alignment should be within "stable" regions.
11) Trim non-overlapping points and the active landslide regions.
12) Align the roughly aligned point clouds from each time step using ICP matching.
13) Perform change detection of choice. The M3C2 algorithm was used in this research (Lague et al. 2013).
14) Determine the LOD for the M3C2 analysis.
    a. The LOD is taken as the 95th percentile of movement in a "stable" region.
15) OPTIONAL: Remove all points within the original change detection point cloud which fall below the LOD to observe only "real movements".

The software programs used for LiDAR processing consisted of: ILRIS's proprietary laser scanner controller software, ILRIS's proprietary parser to convert raw LiDAR data into an '.xyz' file, and CloudCompare V2.10, an open source point cloud software featuring the CANUPO vegetation classification tool (Girardeau-Montaut 2019) (Brodu and Lague 2012).

5.3.2 Results

The calculated LOD for the change detection from July 10 – August 23, 2018, based on the 95th percentile of movement in the stable landslide flanks (See Figure 5-5) was roughly 8 cm, indicating movements below 8 cm are too low to be positively identified as "real movement". 87% of all points within the active region of the landslide were below the LOD and removed.

There are indications of movement near the landslide right toe and headscarp. These regions are highly vegetated relative to other regions of the landslide. Vegetation classification did not fully remove vegetation and the movement detected is largely vegetation loss.

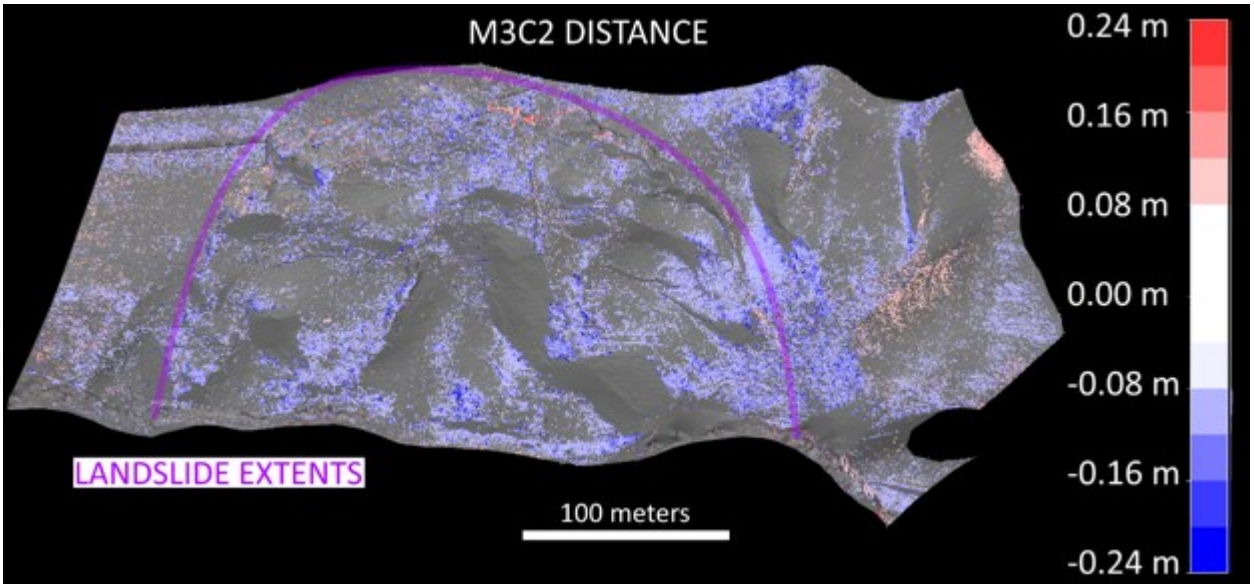

Figure 5-4: LiDAR change detection on Chin Coulee between July 10, 2018 and August 23, 2018 (Only points above the LOD)

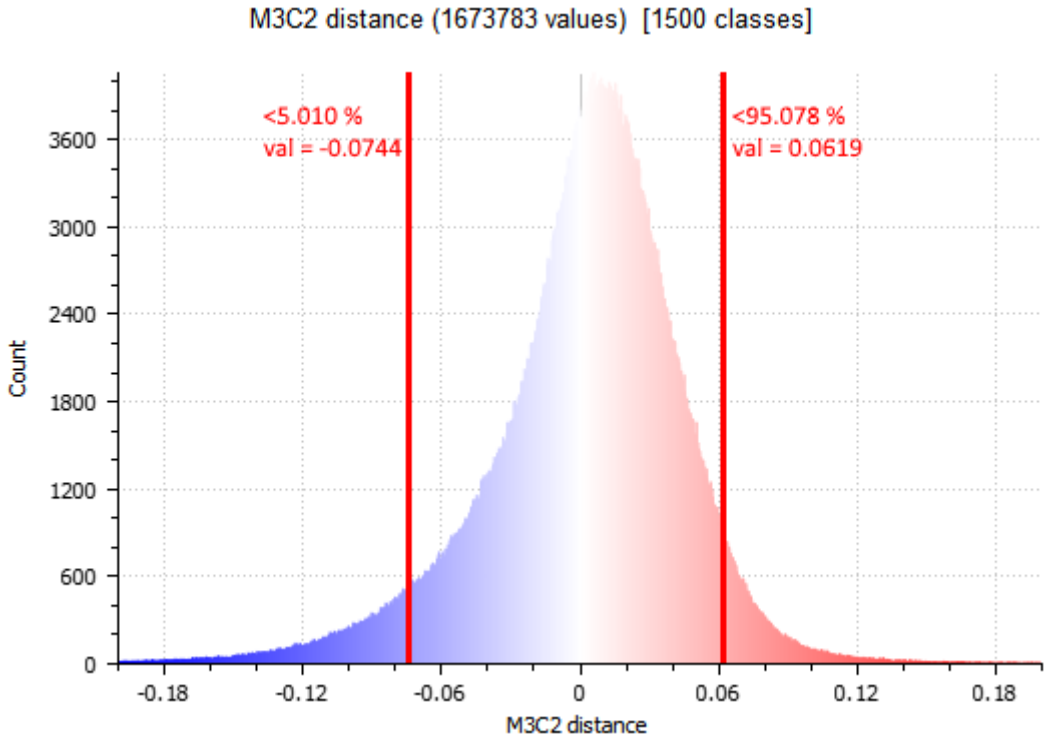

Figure 5-5: Level of detection on Chin Coulee LiDAR change detection between July 10, 2018 and August 23, 2018

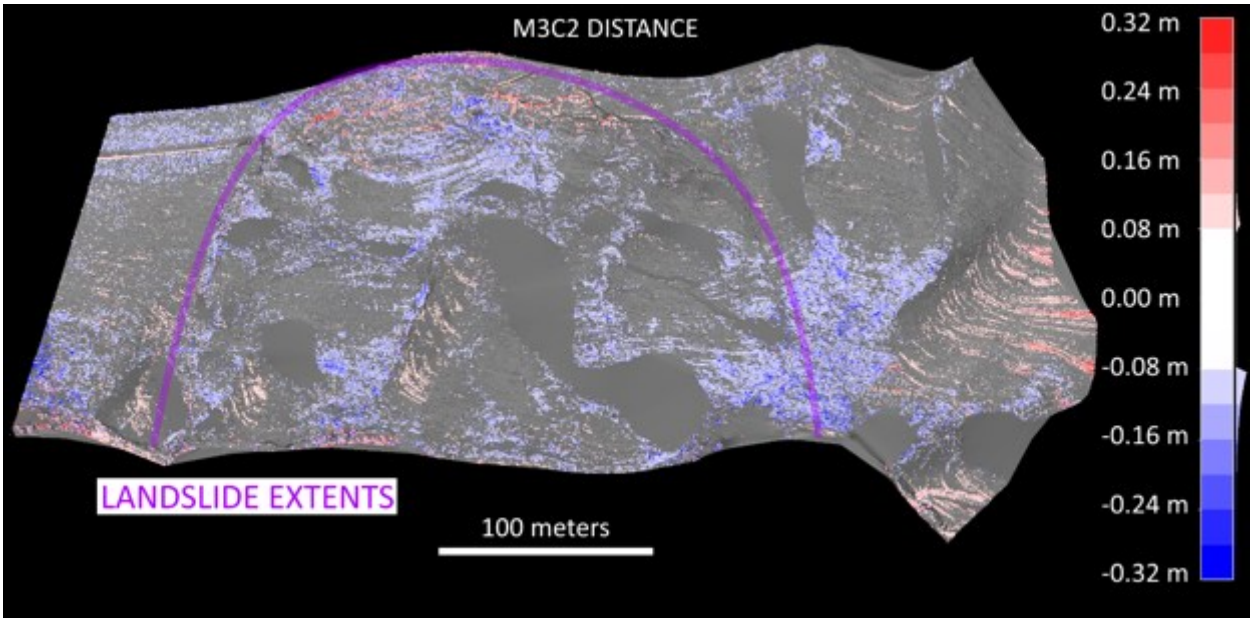

Figure 5-6: LiDAR change detection on Chin Coulee between July 10, 2018 and October 13, 2018 indicating scan issues

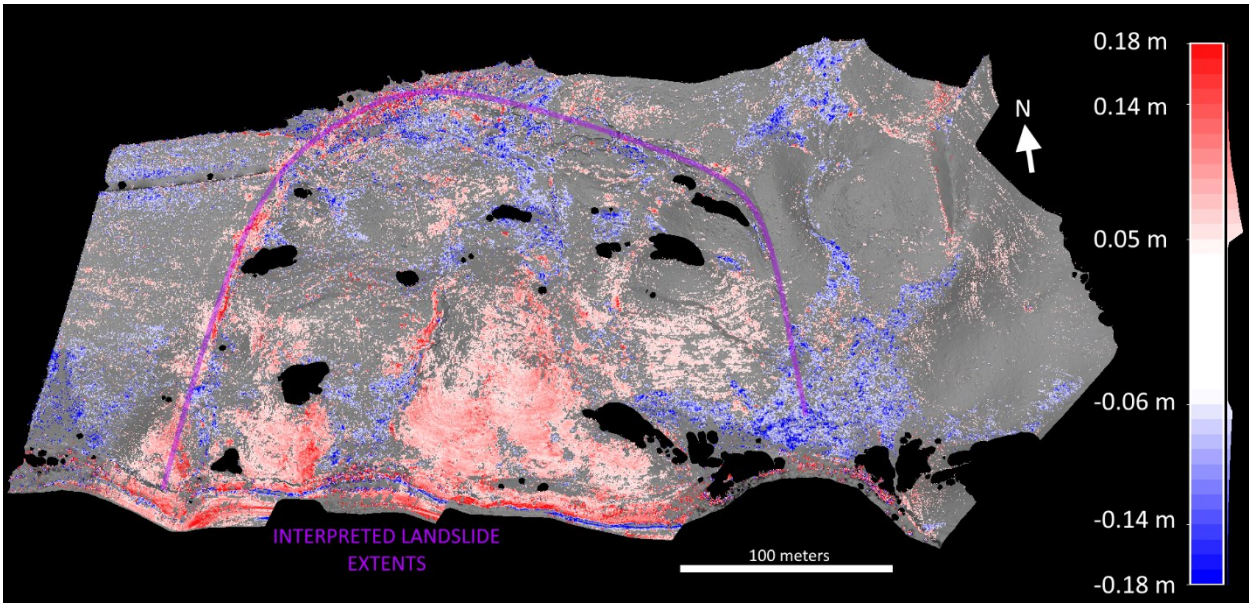

Figure 5-7: LiDAR change detection on Chin Coulee between August 23, 2018 and July 29, 2019 showing detected movement

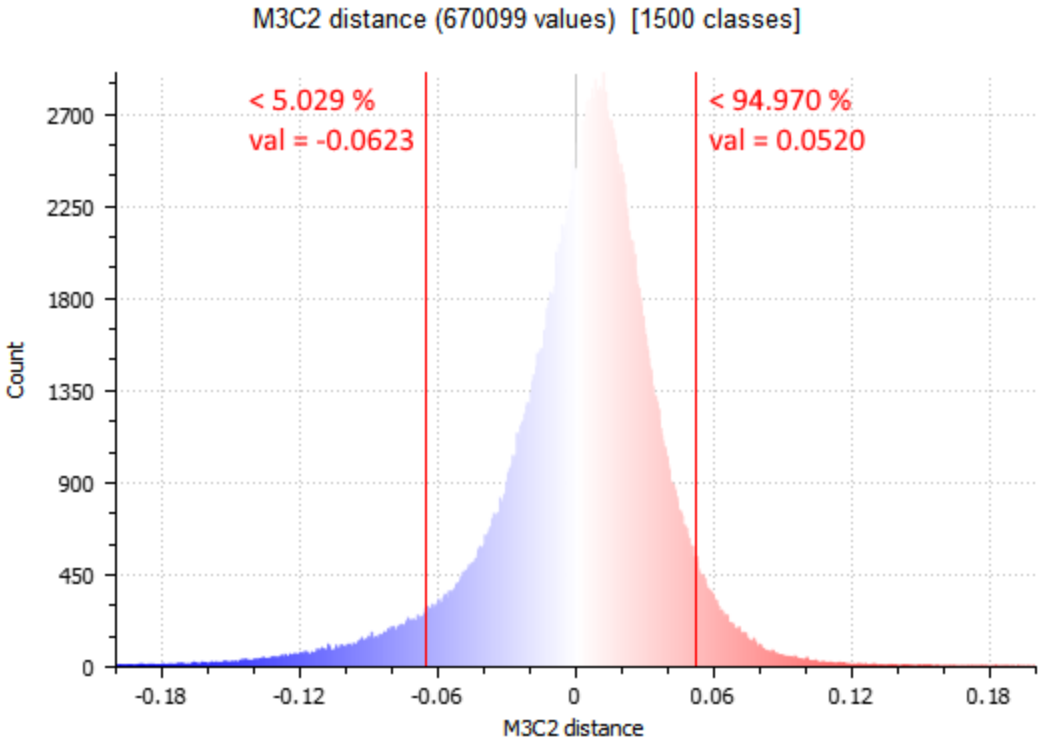

Figure 5-8: Level of detection on Chin Coulee LiDAR change detection between August 23, 2018 and July 29, 2019

5.4 TLS LiDAR Advantages and Limitations

5.4.1 LiDAR Level of Detection Issues

In theory, change detection in a non-moving area should return a displacement of zero. In practice, small variations in the data, misalignment of point clouds, and inaccuracy of the scanner result in movement being detected in non-moving areas. The level of movement observed in this non-moving region is taken as the baseline accuracy of the scan alignment and the 95th percentile is used to define the level of detection (LOD). Detected movement below these values are unreliable and cannot be treated as real movement.

Achievable LOD is impacted by site specific and hardware related limitations (Lague et al. 2013). Point cloud alignment also effects achievable LOD and can be impacted by user error, software limitations, or vegetation.

As the distance from the scanner to the target increases, the positional accuracy of the LiDAR scan decreases due to laser divergence (Fey and Wichmann 2017). Based on divergence specifications provided by the manufacturer of the LiDAR scanner used for this research (7 mm at 100 m) at the average scanning distance on Chin Coulee, a positional error of up to 70 mm is possible in some regions. In order to reduce this error, a more powerful laser must be used, or the scanner must be moved closer to the target. Reducing the angle of incidence to the target also improves the accuracy of the scan and increases the number of returns (Fey and Wichmann 2017). Reducing the angle of angle of incidence or decreasing the distance to the target may not possible, as vantage points for scanning can be limited.

These issues suggest a large advantage for aerial LiDAR scanning. The angle of incidence would be significantly smaller, and scanning would be conducted from much closer to the target.

Outside of equipment and site related limitations, point cloud alignment is primarily impacted by the iterative closest product (ICP) matching process. The ICP matching process is in large part limited by the ability to generate a bare earth model. Vegetation levels on a site can vary between scans significantly, but the ground in non-moving areas should remain relatively similar. As the bare earth model will give a more accurate description of the internal error and deviation of the scan steps to remove vegetation play a critical role in reducing LOD. Options for removing and reducing vegetation include hardware solutions such as LiDAR scanner “last return” settings, or software solutions including vegetation classification tools such as CANUPO classification. External hardware solutions including ground control points can also improve registration (Alba et al. 2006).

5.4.2 LiDAR Bare Earth Model Generation Issues in Vegetated Conditions

Minimizing the LOD in LiDAR data requires a bare earth model.

The following methods were employed on Chin Coulee to obtain close to a bare earth model:

1) The LiDAR scanner was run in “last reflection” and “enhanced range” mode to improve vegetation penetration.
2) A CANUPO classifier was used to classify and remove the remaining vegetation. The “Otira_vegetsemi” model, created by Brodu et al. was used on Chin Coulee. This

classifier is pre-trained and optimized for semi-vegetated ground conditions. Custom CANUPO classifiers were also trained on data collected from Chin Coulee but delivered worse or similar results

3) Additional methods for vegetation removal, discussed in Chapter 2 were used, but did not significantly aid in bare earth model generation. CSF (Zhang et al. 2016) appeared to overly smooth data, removing features which were identified as not being vegetation.

The removal of vegetation from Chin Coulee scans was difficult, and based on change detection results, not entirely successful. Vegetation removal was visually successful, but upon performing change detection, vegetated regions which show no indication of actual movement displayed large amounts of loss or gain.

Manual removal of the remaining vegetation was not feasible, as it would be unreasonably time consuming to manually identify what is ground and what is vegetation for each scan.

The most viable option for these conditions is to work around the heavily vegetated regions. During alignment of two timesteps, heavily vegetated regions which may not have been properly classified were cut out. This improved the alignment of the regions which were known to have not moved (or shown significant vegetation growth) between scans. Once change detection was completed, the regions which were known to be heavily vegetated were acknowledged as not being representative of the actual ground movement in that region. This required knowing which regions were heavily vegetated, observing the time of year the two scans were performed, and the state of vegetation at that time of year.

Vegetation removal and reduction processes improve the results of LiDAR based change detection, but complete reliance upon them is not advisable. These procedures should be used as an improvement method and the resulting “bare earth model” should not be taken to be perfectly representative of a bare earth DEM.

5.5 LiDAR – Summary of Use on Very Slow, Vegetated Landslides

Reduction of the LOD is integral for obtaining detectable movement. The achieved LOD of 5 – 6 cm required roughly 1 full year of monitoring on Chin Coulee in order to observe movement.

The only available option for improving LOD would be further reduction of vegetation, due to site limitations regarding scanner distance and angle of incidence. Despite great effort and time being devoted to classification and removal of vegetation, it was not completely successful.

For best LiDAR results, the following steps should be followed:

- Scans should always be performed in the highest power setting (Enhanced range mode).
- Scans should always use the “last reflection” option if available.
- Scans should only be performed in calm conditions. Wind may shift the scanner itself and may influence the ability for the laser to penetrate vegetation.
- Scanning should involve ground control points whenever possible for increased point cloud alignment.
- Scanning should be performed as close to the target as possible to reduce beam divergence and reduce positional inaccuracy.
- Scanning should be performed with as low of an incidence angle to the scanning surface as possible to reduce positional inaccuracy.
- Vegetation classification should be performed prior to point cloud alignment in order to obtain as close to a bare earth model as possible. CANUPO classification achieved the most reliable results for data collected from Chin Coulee, although other methods are available which may give better results depending on site conditions.
- An understanding of the site vegetation condition at the time of both scans is required. It is likely that change detection will leave vegetated regions partially unclassified. Knowing which regions are heavily vegetated will allow for a more informed decision regarding observed change detection magnitudes.

These steps will help in obtaining the lowest possible LOD but will not guarantee that movement will be detectable. It should not be expected to achieve an LOD lower than 50 mm. This minimum LOD estimate can be used alongside an expected displacement velocity to estimate the required campaign duration for LiDAR change detection.

6.0 Use of Historical Air Photos and UAV Photogrammetry at the Chin Coulee Landslide

UAV photogrammetry was selected as a monitoring method for the Chin Coulee site for comparison with LiDAR change detection. Comparisons of the results of both methods is useful as both employ the same methodology behind displacement computations. Historical air photo photogrammetry was used to understand the historical displacement pattern.

This chapter discusses the application of UAV and air photo photogrammetry to the Chin Coulee landslide, outlines the data collection and processing procedure, and makes observations regarding advantages and limitations of UAV photogrammetry on Chin Coulee and similar sites. Discussion and interpretation of results regarding landslide kinematics is performed in Chapter 8.

6.1 Historical Air Photo Photogrammetry

Historical air photos of the Chin Coulee landslide area are available from 1945 to 2012, roughly every 10 years (See Table 6-1). These air photos provided a means of observing the history and evolution of the landslide over the course of almost 7 decades, providing valuable insight into contributing factors for the initiation and continued movement of the Chin Coulee landslide.

In addition to visual inspection, advanced software can be used to create 3-dimensional models from these photo sets.

Table 6-1: Historical air photo year and resolution

Year	1945	1960	1970	1982	1993	1999	2012
Figure:	Figure 8-1	Figure 8-2	Figure 8-3	Figure 8-4	Figure 8-5	Figure 8-6	Figure 3-2
Resolution	1:20000	1:20000	1:30000	1:2500	1:30000	1:30000	1:30000

6.1.1 Air Photo Photogrammetry Methods and Results Sample

Air photo photogrammetry was completed using Pix4D, a photogrammetry software program that uses computer vision algorithms to convert series of 2D photos into 3D models (Pix4D 2019). The procedure for processing photographs into 3D models is explained in Section 6.2.2.

Figure 6-1 shows an example of a photogrammetry model generated from five air photos taken in 1982 of Chin Coulee, just after landslide initiation in 1978.

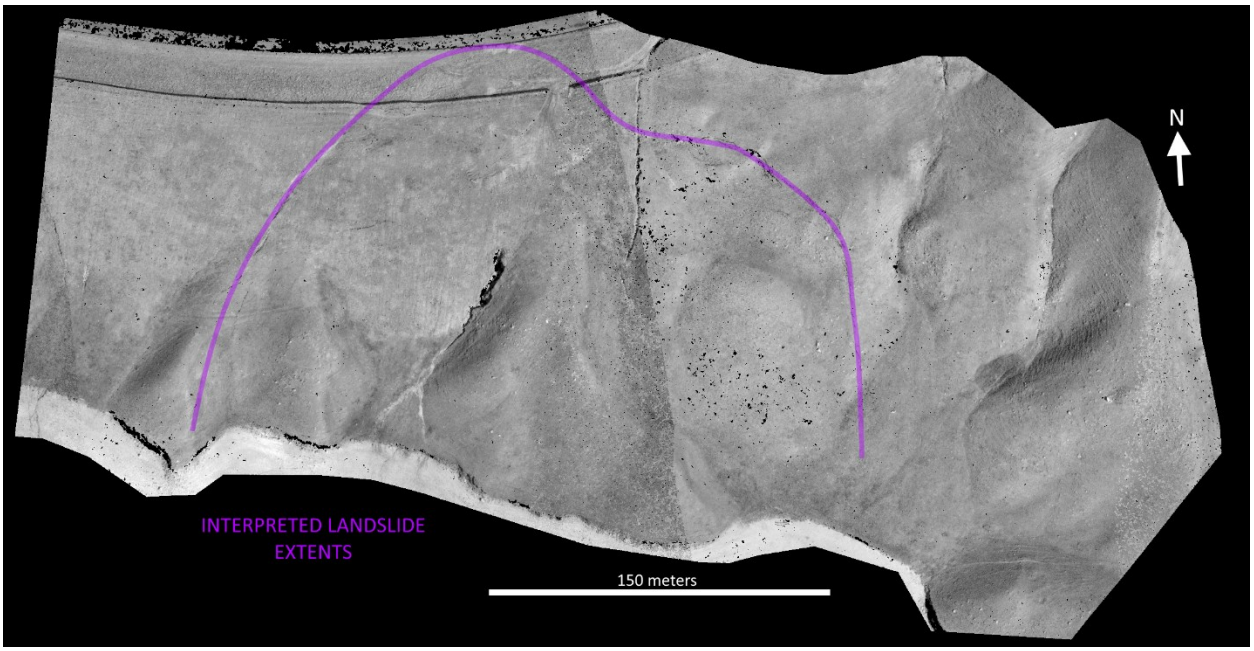

Figure 6-1: 1982 photogrammetry model generated in Pix4D (Pix4D 2019)

Photogrammetry models are fully 3-dimensional point cloud models. This provides an opportunity to complete change detection using historical ground conditions and modern LiDAR scans. Figure 6-2 shows an example of a change detection analysis completed between the 1982 photogrammetry model shown in Figure 6-1 and a LiDAR scan completed on July 29, 2019. An LOD of roughly 1 meter was observed.

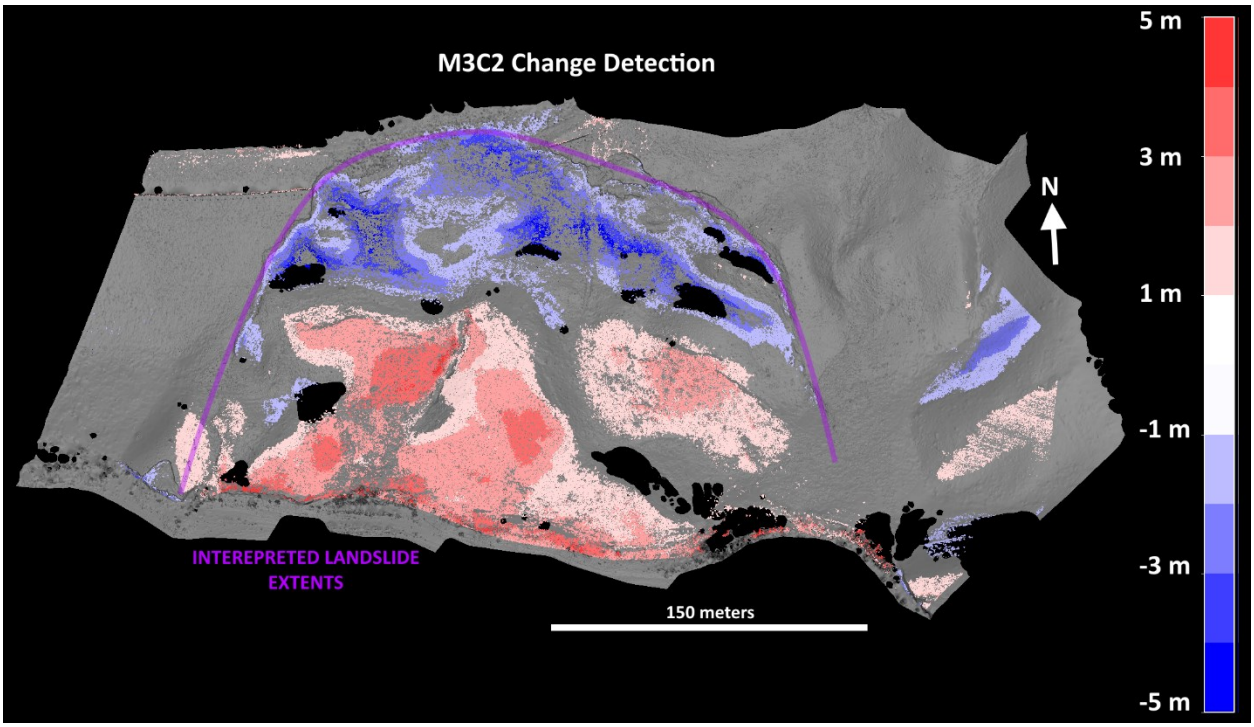

Figure 6-2: 1982 photogrammetry model – July 29, 2019 LiDAR scan M3C2 change detection

6.1.2 Air Photo Photogrammetry Advantages and Limitations

Change detection results from air photo photogrammetry should be taken as qualitative, as model accuracy from only five images is low. Regions throughout the landslide showed poor alignment including a region on the right flank (See Figure 6-2) which suggests a movement of 2-3 meters in a region that is thought and observed to be stable.

The 1:2500 scale photographs used for the 1982 model are atypically high resolution. Typical air photos are 1:30000 or 1:20000, with some photo sets being 1:60000 or more. Attempts at producing models from photo sets at even 1:20000 proved difficult. Visual inaccuracies were too large to justify change detection analysis using the generated models.

Figure 6-3 shows an example of a photogrammetry model attempted using three photos taken in 1945 at a resolution of 1:20000. The resulting photogrammetry model produced a point cloud with little to no depth and didn't accurately map the topography of the glacial valley in which the Chin Coulee reservoir is situated. It should be noted that there is no scale in this

image, as the photos are not geolocated the software has no size reference. Attempts at producing models from a 1:30000 photoset taken in 2009 resulted in a photograph error, indicating there was insufficient resolution to create a 3-dimensional model.

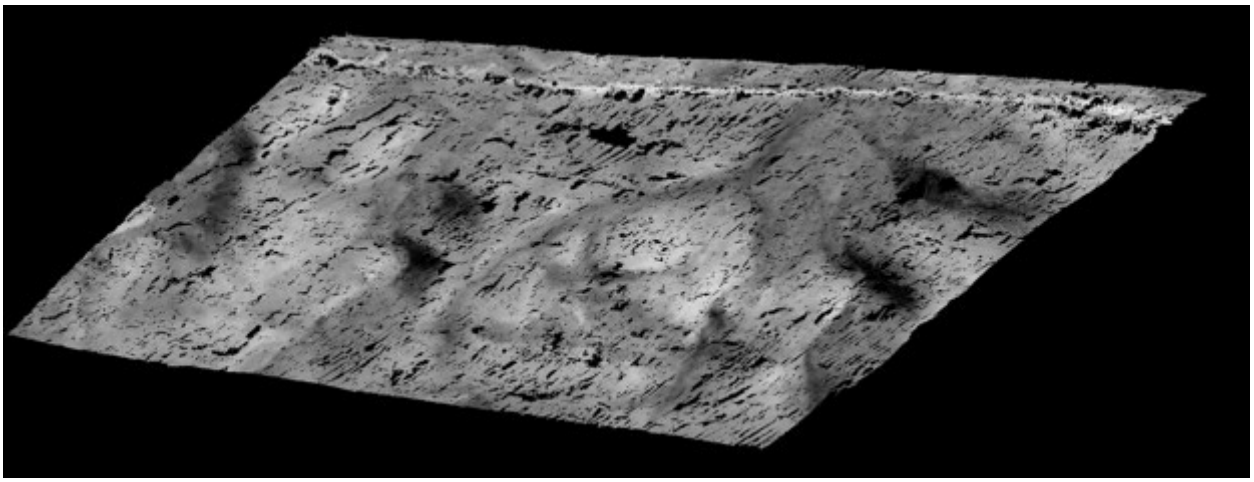

Figure 6-3: 1945 photogrammetry model generated in Pix4D showing unrealistically flat profile

Photo coverage and photo resolution are the two most important factor in air photo photogrammetry for model accuracy. Photogrammetry software requires at least three photos covering a single point to reproduce the point within the 3D model. As the scale of the photo increases, less photos are required to cover the entirety of the site, but the resolution of the photo decreases and may not be able to be processed by the software.

Historical air photo photogrammetry is limited due to the absence of GCPs. GCPs improve the accuracy of a 3D model and allow for geolocation of data. Identification of structures which could act as GCPs in historical photos is possible, however this often requires the assumption that these structures or objects have not moved in the time span between when the photo was taken and when the object was geolocated. Several large rocks identified in the 1982 photos and 2015 satellite photos were used as GCPs in the creation of the 1982 photogrammetry model shown in Figure 6-1. This was possible due to the high resolution of the 1982 photos and was not possible with lower resolution air photos.

6.1.3 Air Photo Photogrammetry Interpretation

Based on the completed 1982 3D model, four years after the initial slope failure a drop of approximately 1 meter was observed. As of 2019, the headscarp has continued to drop roughly 4 – 6 meters, depending on location. Based on visual inspection of the site, estimates of pre-existing ground conditions, and analysis of LiDAR data, a headscarp drop of roughly 5 – 6 m from original ground level would be reasonable. Analysis of the pre-failure conditions in 1945, 1960, or 1970 for comparison to the 1982 model was not possible due to the inability to generate a 3D model.

The 1982 – 2019 change detection also provides support for the proposed compound failure method. In Figure 6-2, blue loss at the headscarp depicts a horst-like wedge dropping down, resulting in red gain near the center and toe of the landslide as the graben-like structure moves laterally outwards. This horst and graben-like structure descriptor is used as a purely visual description. Horst and graben landslide structures are commonly used to describe sensitive clay failures in which extreme lateral spreading results in inverted pyramidal grabens and pyramidal horsts (Figure 6-4). The resulting shapes of the failure is less extreme on Chin Coulee, as the lateral spreading is significantly lower, but the general shape and structural formation is similar.

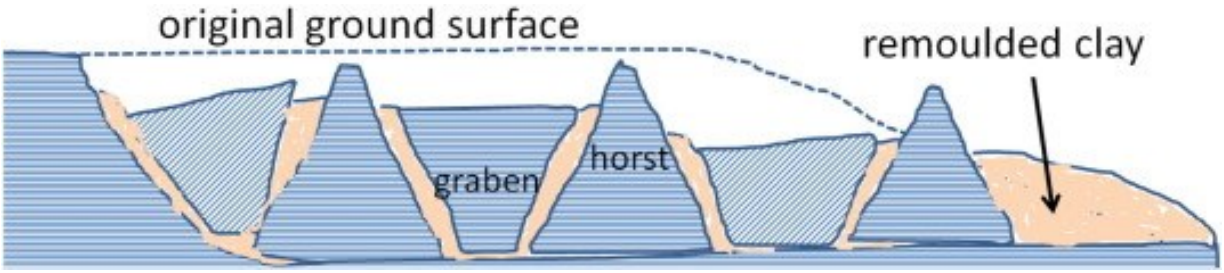

Figure 6-4: Typical horst and graben structure common within sensitive clays (Geertsema, et al. 2018 – With permission)

6.2 UAV Photogrammetry

UAV based monitoring is becoming increasingly popular in the geotechnical field for hazard monitoring. It provides a safe way of observing inaccessible regions at a fraction of the cost of

most monitoring tools. UAV photogrammetry allows for the additional creation of 3D models, which can be used for change detection (Rodriguez, Hendry and Macciotta 2018).

6.2.1 UAV System Deployment

All UAV flights were performed using a DJI Phantom 4 Pro and Pix4DCapture, a UAV flight software application (Pix4D 2019) (Figure 6-5 and Figure 6-6). An average flight altitude of 30 – 40 m was used, and a photograph overlap of 80% was selected within Pix4DCapture. This selected overlap is larger than the Pix4D recommended 75% for the type of flight performed (Pix4D). All UAV flights employed a double grid format for complete photograph coverage. Photogrammetry was completed using eight GCPs and one check point (CP) (Figure 6-7). GCPs and CPs were located evenly across the site, within 1 to 2 m of installed Geocube units. No guidelines are available regarding where GCPs should be located, only that uniform coverage of the target site ensures that GCPs are visible within several photographs. As the Geocubes locations were fixed during the research timeline, and evenly spaced across the site, placing GCPs near the Geocubes ensured relative consistency between UAV flights. GPS measurement accuracy for all GCPs and CPs was 10 cm.

Table 6-2 summarizes UAV flight dates and notes regarding the overall quality.

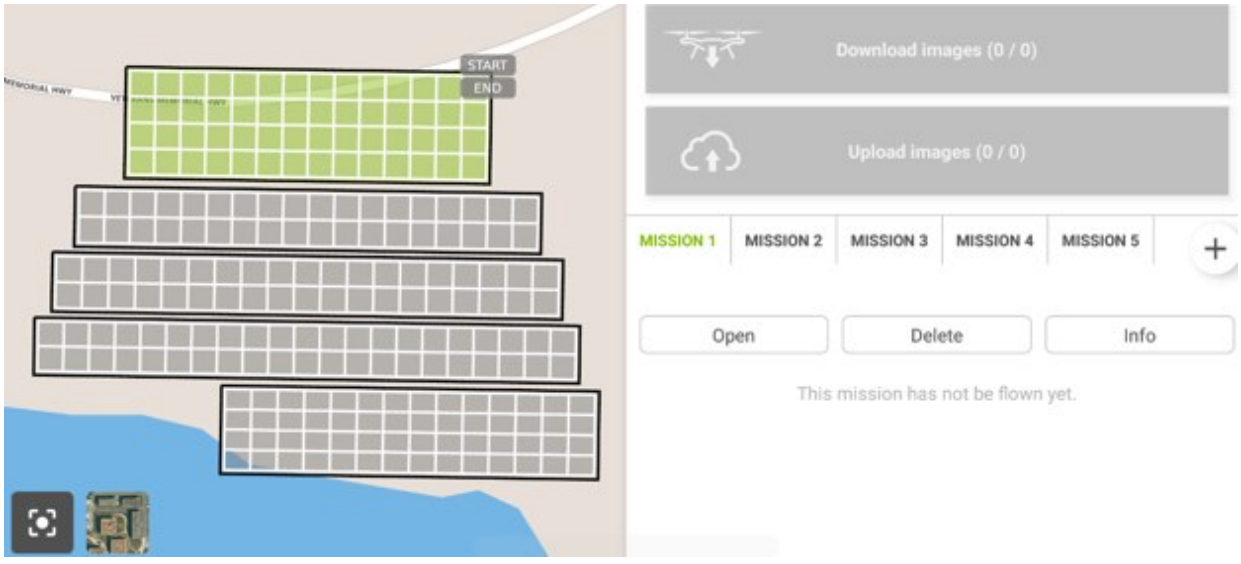

Figure 6-5: Pix4DCapture flight plan ui for Chin Coulee (Pix4D 2019)

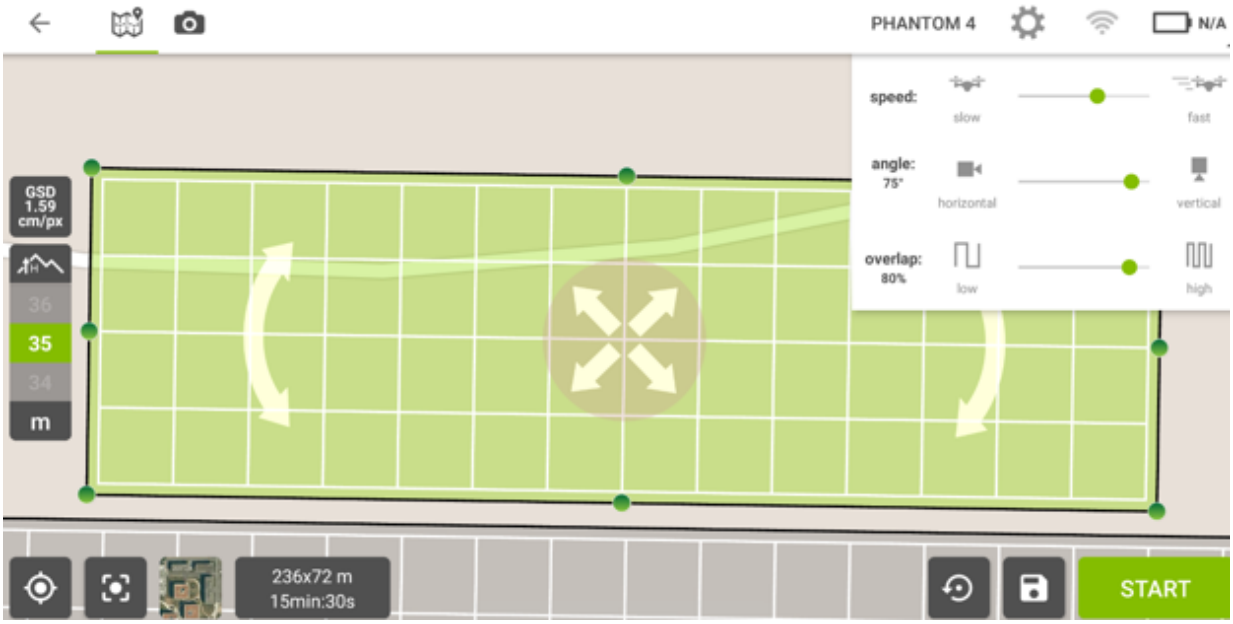

Figure 6-6: Pix4DCapture flight parameters on Chin Coulee (Pix4D 2019)

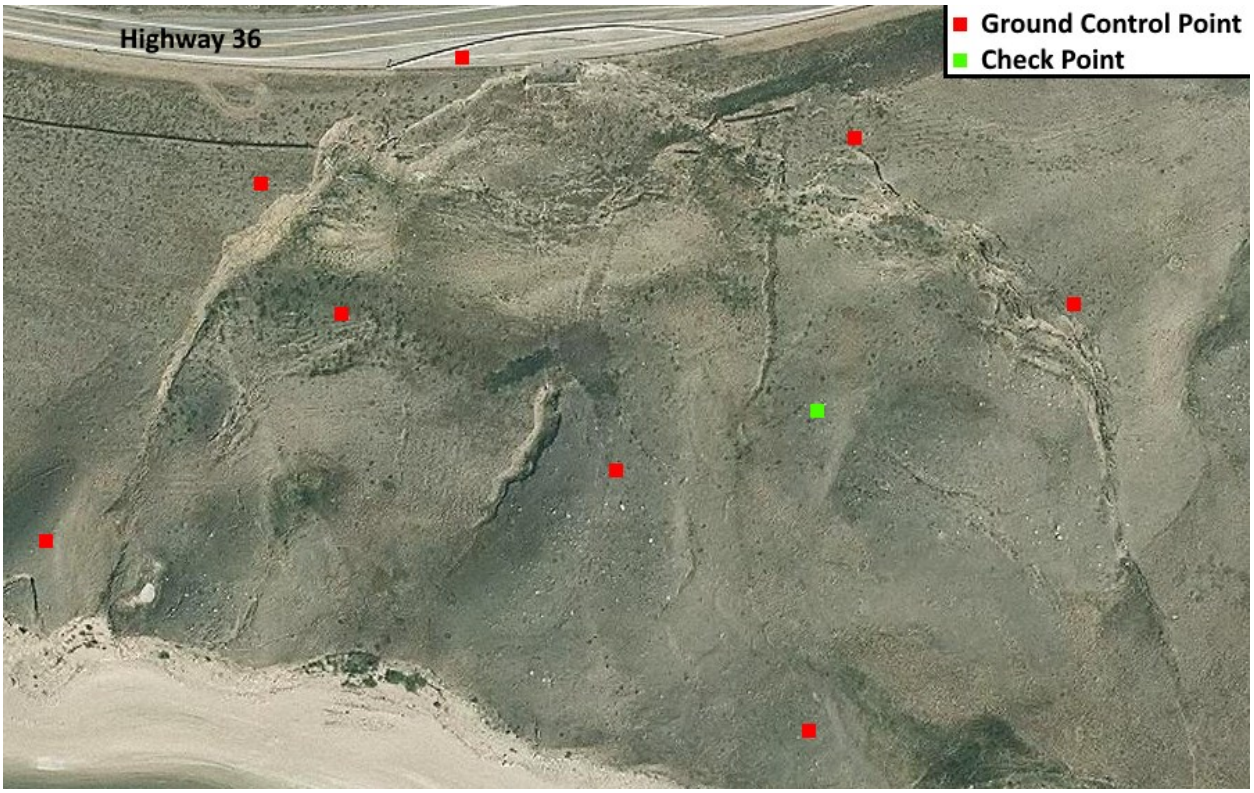

Figure 6-7: Typical ground control points and check point layout on Chin Coulee (Base imagery from ESRI 2019)

Table 6-2: Summary of UAV flights

Flight Date	**Quality**	**Notes**
August 23, 2018	Adequate	
October 13, 2018	Inadequate	Extremely high winds required the flight to be cancelled immediately after attempted takeoff.
May 9, 2019	Inadequate	The GPS subscription license was expired, as such, no GCPs were able to be established. High winds also resulted in an incomplete flight.
July 30, 2019	Adequate	Some photos were washed out due to bright sunlight during the UAV flight which may have reduced the model accuracy.

6.2.2 UAV Photogrammetry Data Processing

6.2.2.1 Methods and Software

Photographs taken from the UAV were processed using Pix4DMapper V3.0.17 to generate point clouds from the photographs (Pix4D 2019). The processing parameters used within Pix4D are shown in Table 6-3.

Table 6-3: Pix4DMapper processing options

Step	**Substep**	**Value**
Processing Option	Initial Processing Defaults	3D model
Initial Processing	Keypoint Image Scale	Custom: 2 (Double image size)
	Matching Image Pairs	Free Flight or Terrestrial
	Matching Strategy	Use Geometrically Verified Matching
	Targeted Number of Keypoints	Automatic
	Calibration Method	Standard
Point Cloud and Mesh	Image Scale	1 (Original image size, slow)
	Point Density	High (Slow)
	Minimum Number of Matches	3

The following steps within Pix4DMapper were followed:

1) Image quality control. Photographs featuring blur artifacts were removed.
2) Initial processing within Pix4DMapper. This process finds keypoints within all the images which the software believes to match other images and aligns and calibrate the images.
3) Initial processing quality control. Check for any errors within the initial model. Errors typically occur when a blurry photograph was not removed in step 1.
4) Input GCP and CP locations.
5) Locate GCPs and CPs with rayCloud Editor within Pix4DMapper. Nine images were used for locating GCPs and CPs within the rayCloud Editor.

6) Run point cloud and mesh within Pix4DMapper.

Table 6-4 and Table 6-5 summarizes the achieved model characteristics from the August 23, 2018 and July 30, 2019 flights on Chin Coulee.

Table 6-4: Quality report for Pix4DCapture generated models on August 23, 2018 Chin Coulee flight

Characteristic	**Value**
Median Number of Keypoints Identified per Image	31,977
Median Number of Matches per Image	13,743
RMS Error (X) (m)	0.059
RMS Error (Y) (m)	0.052
RMS Error (Z) (m)	0.059
Check Point RMS Average Error (m)	0.060
Point Cloud Average Density (points/m^2)	3253
Point Count	775,637,339

Table 6-5: Quality report for Pix4DCapture generated models on July 30, 2019 Chin Coulee flight

Characteristic	**Value**
Median Number of Keypoints Identified per Image	98,532
Median Number of Matches per Image	43,127
RMS Error (X) (m)	0.329
RMS Error (Y) (m)	0.210
RMS Error (Z) (m)	0.079
Check Point RMS Average Error (m)	0.147
Point Cloud Average Density (points/m^2)	4240
Point Count	730,565,122

6.2.2.2 Results Samples

Figure 6-8 and Figure 6-9 show examples of the UAV photogrammetry generated point cloud from the August 23, 2018 and July 30, 2019 flights on Chin Coulee. Random subsampling to remove 90% of points was applied due to the density of the generated point clouds and memory constraints within CloudCompare.

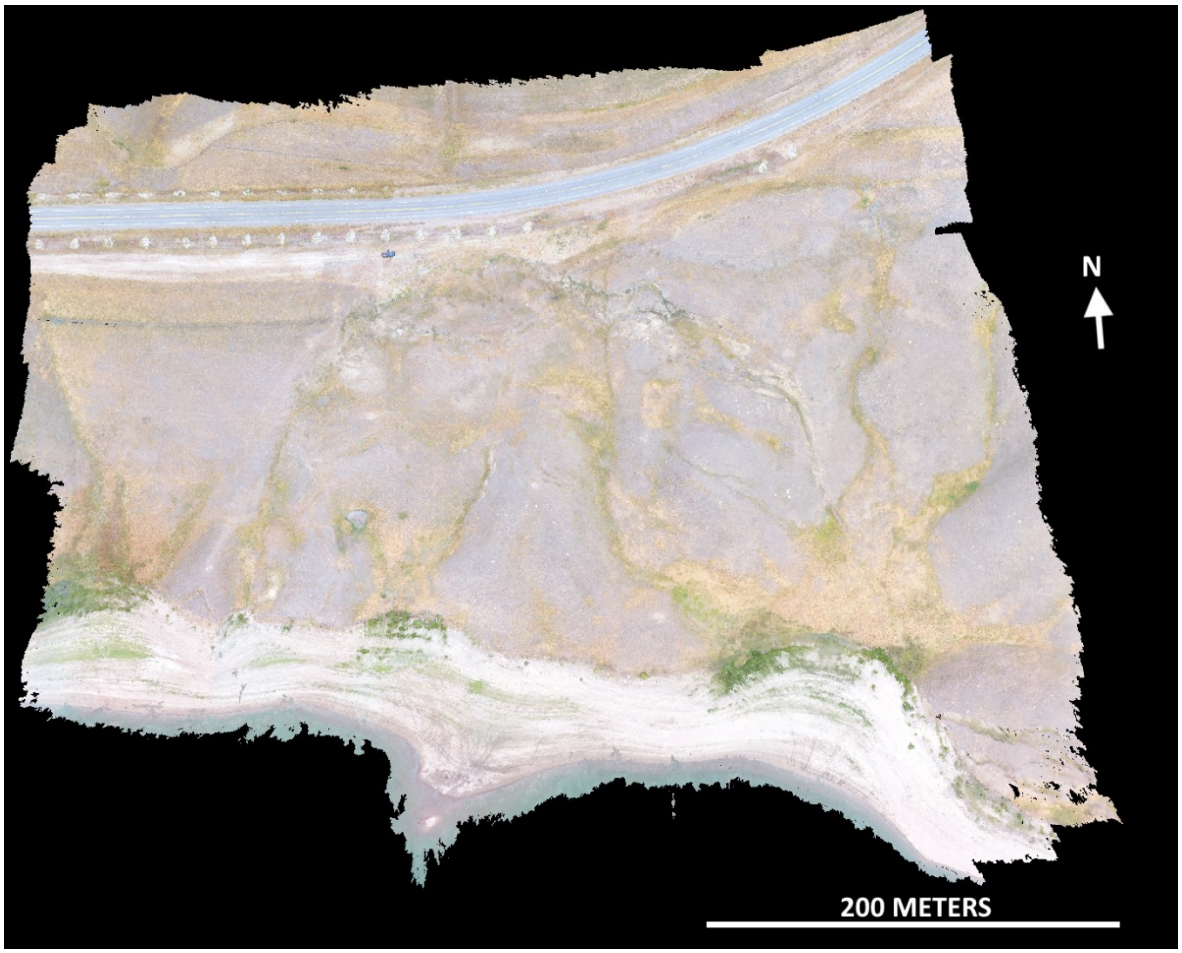

Figure 6-8: UAV photogrammetry model from August 23, 2018 flight on Chin Coulee

Figure 6-9: UAV photogrammetry model from July 30, 2019 flight on Chin Coulee

CANUPO classification was applied to the August 23, 2018 UAV flight to test vegetation classification of UAV generated DEMs. Prior to classification random subsampling was applied to reduce cloud point density by 90%. Regions around the exterior of the landslide were removed due to low photo coverage and overlap. Figure 6-10 shows the resulting point cloud after classification and removal of vegetation.

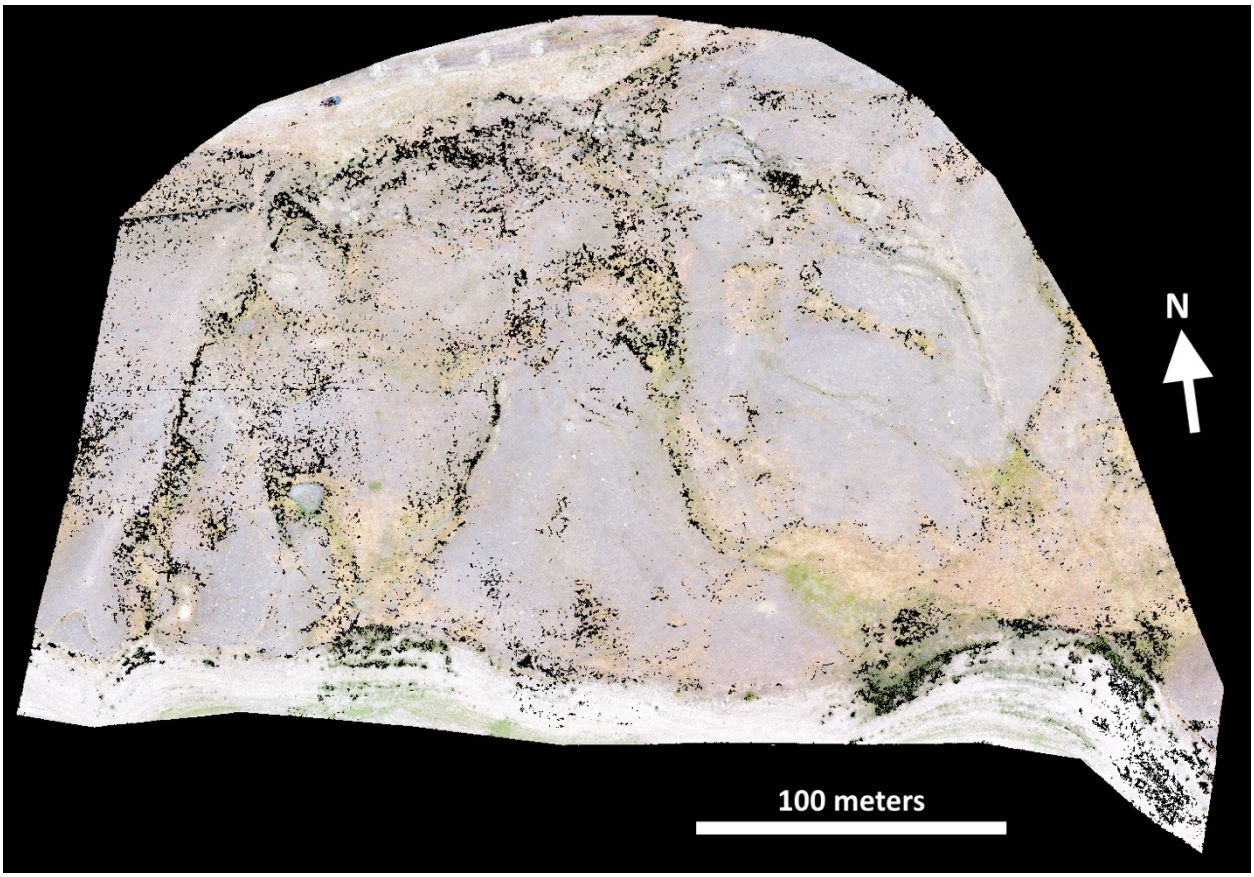

Figure 6-10: Ground classified UAV photogrammetry model from August 23, 2018 flight on Chin Coulee

Change detection was completed between the August 23, 2018 and July 30, 2019 photogrammetry models. The resulting M3C2 distance point cloud is shown in Figure 6-11A. The calculated LOD was 9 – 11 cm (See Figure 6-11B).

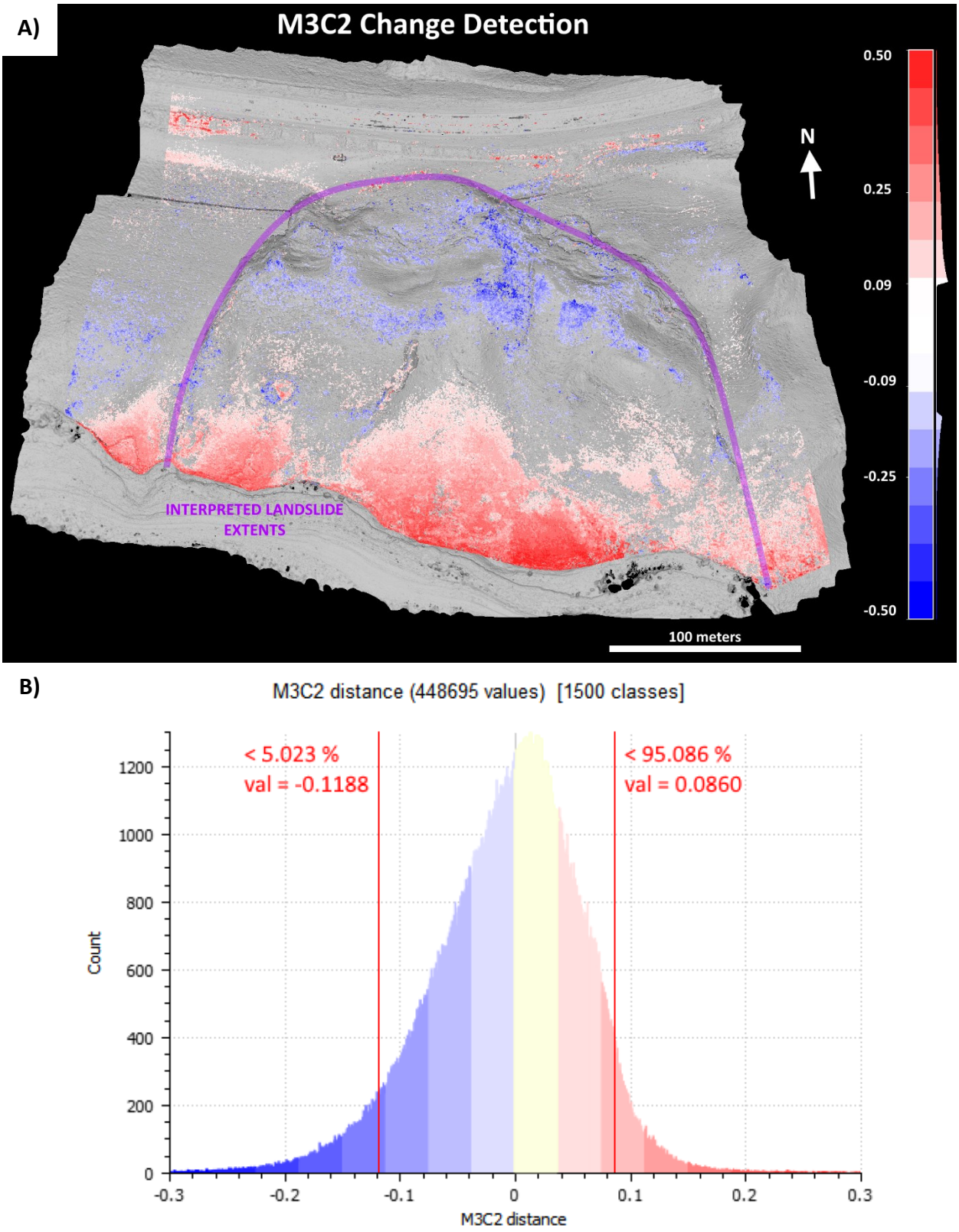

Figure 6-11: M3C2 change detection completed between August 23, 2018 and July 30, 2019 (A), level of detection (B)

Identification of erosional channels and feature tracking was performed based on the August 23, 2018 UAV photogrammetry model and the original 1998 extents produced by Golder and Associates (1998). Figure 6-12 shows a qualitative change detection performed between 1998 and 2018.

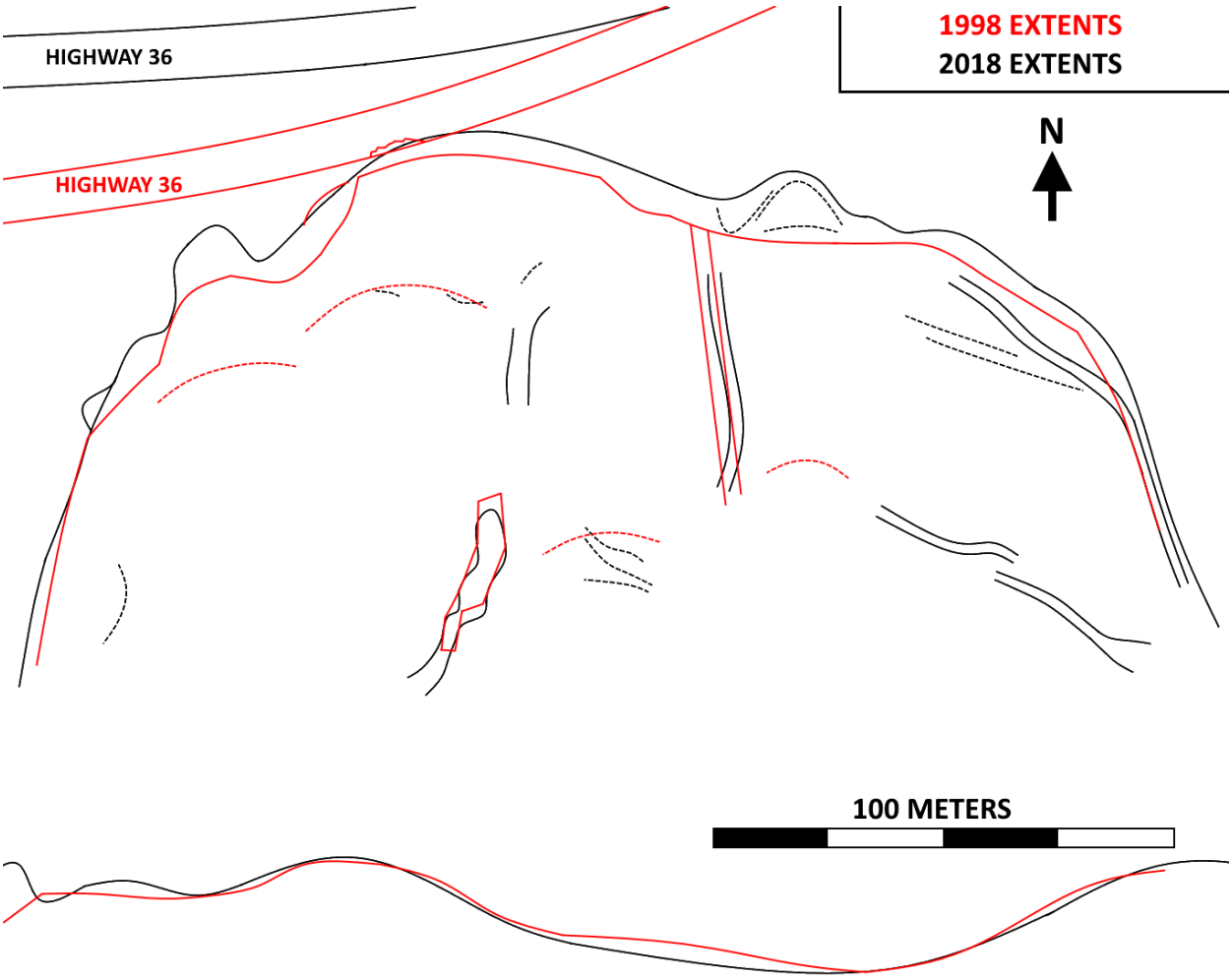

Figure 6-12: UAV-based qualitative change detection on Chin Coulee (1998 extents based on Golder and Associates 1998)

The 1998 extents shown in Figure 6-12 were created using a slightly different interpretation when defining the boundaries of a scarp region, due to the available monitoring tools at the

time. Although retrogression has occurred throughout the last 20 years, the degree of retrogression suggested by this change detection is likely exaggerated. Based on air photo observations and site investigation reports, there is little evidence that 10 – 25 m of horizontal scarp retrogression has occurred. Much of the differences between the two extents can be attributed to the versatility of UAV photogrammetry models outside of change detection. Much greater detail regarding erosional channel shape and direction as well as headscarp and sliding block formations are possible when analysis can be performed in the office with a high-resolution aerial model.

6.2.3 UAV Photogrammetry Advantages and Limitations

6.2.3.1 UAV Photogrammetry Vegetation Issues

Photographs cannot penetrate vegetation, as a side effect photogrammetry point clouds are akin to a "treetop" model rather than a true bare earth model.

To test the ability of vegetation classification on photogrammetric point clouds, a CANUPO classifier was applied to the August 23, 2018 UAV photogrammetry generated point cloud (See Figure 6-10) (Brodu and Lague 2012). Vegetation classification was visually poor. Trees and larger bushes appeared to be most effectively classified, while classification of grasses was ineffective. This is most apparent near the right toe of the landslide which features yellow shading due to grasses.

6.2.3.2 UAV Photogrammetry Level of Detection

Like LiDAR, UAV photogrammetry suffers from LOD issues when combined with Very Slow landslides. Larger periods of time are required in order to observe detectable movement.

Change detection performed between the August 23, 2018 and July 30, 2019 flights indicated an LOD of roughly 10 cm (See Figure 6-11). This is slightly higher than the 6 – 8 cm LOD achieved from typical LiDAR scanning performed on Chin Coulee (See Chapter 5).

Although only two UAV flights were completed on Chin Coulee, it is unlikely that detectable movement would have been observed if flight frequency was increased, based on the observed GPS movement and the available LOD of the UAV change detection.

Vegetation within stable regions reduces the LOD of photogrammetry, as vegetation will show increased movement between flights (Due to vegetation changes), which is then taken into the LOD calculation.

Photo quality during the July 30, 2019 flight was also degraded due to the brightness at the time of flight and subsequent high exposure of the landslide. This can be reduced using shaded lenses but is often difficult to diagnose as a potential problem prior to flight and data collection.

Photo quality is also dependent on the UAV flight parameters. The closer to the target a flight is performed, the higher quality the photographs captured will be. A balance between battery life, photo overlap, and flight altitude must be made prior to data collection. Lower flight altitudes result in longer flight times, which may exceed the battery capacity of the UAV. A flight altitude of 35 m and a photo overlap of 80% was used on Chin Coulee as this provided good quality while allowing flight times to remain under the battery limit of the UAV. This limitation can be overcome in part by splitting flights into several regions (See Figure 6-5) and completing several flights.

The accuracy of the GCPs and CPs used during photogrammetry also plays a role in point cloud accuracy. The GCPs are used to help align the model and as known reference points for photographs. In some cases, the model is geolocated entirely from the GCPs. For Chin Coulee, the GPS unit used for GCP geolocation had a horizontal point accuracy of 10 cm. With higher quality GCP measurements, model accuracy would likely also increase.

6.2.4 UAV Photogrammetry – Summary of Use on Very Slow, Vegetated Landslides

Vegetation severely limits the application of UAV photogrammetry. Without the ability to generate a true bare earth model, UAV photogrammetry-based change detection in heavily vegetated regions is not reliable. Vegetation classification tools are not effective at classification of smaller scale vegetation such as prairie grasses and smaller bushes. Even with faster moving landslides, vegetation changes throughout the year and year-to-year will exceed ground movement. Under heavier vegetation conditions, UAV photogrammetry is not recommended as a primary means of monitoring.

The effect of vegetation is compounded in Very Slow landslides. With movement levels pushing the limits of the level of detection, a bare earth model becomes essential, but vegetation often cannot be removed from the point clouds. Like LiDAR, long campaign durations become necessary in order to observe movement above the achievable LOD.

It should not be expected to achieve an LOD lower than 80 mm using UAV photogrammetry in vegetated conditions. This minimum LOD estimate can be used alongside an expected displacement velocity to estimate the required campaign duration for UAV based change detection.

7.0 Comparison of Results from Monitoring Methods

To compare the results of LiDAR, UAV, and GPS change detection, representative samples of M3C2 change detection points within a 4 m radius of each Geocube location were selected, a gaussian distribution of the scalar value of M3C2 displacement was generated, and the mean and standard deviation was recorded (See Table 7-1). M3C2 results were taken from the August 23, 2018 to July 30, 2019 scans and flights. Included GPS movements were also measured between these two dates.

Inconsistency between monitoring methods occurred at several Geocube locations. For example, sample points taken from LiDAR change detection around Geocube 151 (See Figure 4-1 for location) showed movement out of the slope 21 mm, while points taken from UAV change detection suggested movement into the slope of 59 mm. Geocube 151 GPS movement showed a vertical drop of 17 mm and a 3D displacement of 35 mm.

Some inconsistency between GPS measurements and LiDAR/UAV change detection is expected as M3C2 displacement is calculated differently from GPS displacement. GPS displacement is measured in true 3D space. In contrast, M3C2 change detection measures displacement normal to the local slope. The resulting M3C2 displacement value is only truly representative of ground movement when the ground moves completely normal to the slope (See Figure 7-1).

The significance of this difference in actual ground movement direction versus the assumed M3C2 ‘normal to the slope’ movement direction varies depending on the location within the landslide as both the ground movement pattern and slope varies across the landslide.

For example, at the headscarp, the slope is quite flat. M3C2 displacement measurements would represent a vertical displacement of the ground in this region and should overwhelmingly agree with the vertical displacement of the GPS unit alone. Conversely, on a vertical face, M3C2 displacement would represent horizontal displacement. In a sloped region, M3C2 displacement would be perpendicular to the slope angle, incorporating a vertical and horizontal component. The most accurate comparison between GPS data and M3C2 change detection would require finding the component of GPS displacement normal to the slope, based on the local slope angle.

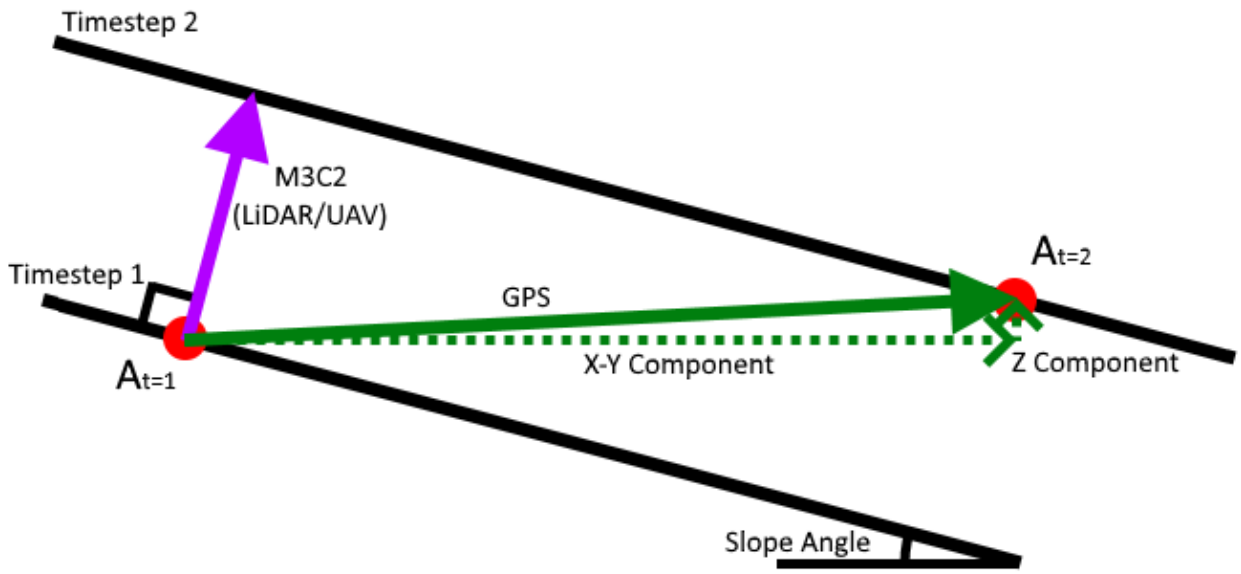

Figure 7-1: Pictorial comparison of M3C2 displacement vs GPS displacement

Assuming small levels of movement, where large surface feature movement has not exceeded the averaging distance used during M3C2 calculation (See Section 2.4), similar local slope angles and slope shapes would exist when comparing point cloud data. With larger displacements, the local slope environment may have significantly changed from one timestep to another. For example, a rolling ridge may have moved downslope significantly and the same point in space is now occupied by a valley. The ground has not sunken in this spot but translated. GPS would indicate this, but other forms of change detection would observe this as a loss of material.

At the scale of displacements observed on Chin Coulee, displacement can be simplified as a calculation of distance between two planes. The shortest distance between two planes is a line normal to one plane. In this manner, M3C2 change detection should always return lower or equal levels of displacement than GPS readings, assuming perfect point cloud alignment and data collection. In many cases (See Table 7-1), M3C2 shows larger displacements than 3D GPS readings, suggesting point cloud alignment error in some regions, possibly due to human error or technological limitations (i.e. LOD).

Table 7-1: GPS, LiDAR, and UAV change detection results comparison for movement from August 23, 2018 to July 30 2019

Geocube Location	Method		Mean Value (mm)	Standard Deviation (mm)
151	GPS	Horizontal	31	
		Vertical	-17	
		3-Dimensional	35	
	LiDAR M3C2		21	±43
	UAV M3C2		-59	±34
152	GPS	Horizontal	1	
		Vertical	-1	
		3-Dimensional	1	
	LiDAR M3C2		No Points	No Points
	UAV M3C2		0	±32
153	GPS	Horizontal	16	
		Vertical	+30	
		3-Dimensional	34	
	LiDAR M3C2		90	±24
	UAV M3C2		184	±22
154	GPS	Horizontal	20	
		Vertical	+15	
		3-Dimensional	25	
	LiDAR M3C2		28	±15
	UAV M3C2		-30	±49
172	GPS	Horizontal	20	
		Vertical	0	
		3-Dimensional	20	
	LiDAR M3C2		54	±26

	UAV M3C2		65	±37
173	GPS	Horizontal	7	
		Vertical	-5	
		3-Dimensional	9	
	LiDAR M3C2		13	±28
	UAV M3C2		-1	±37
174	GPS	Horizontal	13	
		Vertical	-3	
		3-Dimensional	13	
	LiDAR M3C2		26	±44
	UAV M3C2		3	±81
176	GPS	Horizontal	51	
		Vertical	+16	
		3-Dimensional	53	
	LiDAR M3C2		70	±17
	UAV M3C2		332	±23
177	GPS	Horizontal	8	
		Vertical	-1	
		3-Dimensional	8	
	LiDAR M3C2		13	±28
	UAV M3C2		31	±16

The entire displacement point cloud for both LiDAR and UAV was split into three regions to allow for comparison of the data in its totality: Headscarp, Upper, and Toe (See Figure 8-9 and Figure 8-10 for visual delineation of regions). The mean and standard deviation of movement for these regions is summarized in Table 7-2.

Table 7-2: LiDAR and UAV movement by region from August 23, 2018 to July 30, 2019

Data Source	Region	Mean (mm)	Standard Deviation (mm)
LiDAR	Headscarp	-84	±260
	Upper	-33	±100
	Toe	+76	±37
UAV	Headscarp	+71	±233
	Upper	-210	±84
	Toe	+226	±93

7.1 Correlation and Consistency Analysis

A correlation analysis of recorded movement was conducted to better understand the results and the magnitude of disagreement between the three measurement methods (See Figure 7-2). Each subplot shows a different correlation, with color depicting the region in which those points were taken (See Figure 8-9 and Figure 8-10 for visual delineation of regions). The black line accounts for points within all three regions, while the colored lines account for points only within their respective region. The red line symbolizes a perfect 1:1 fit between the two monitoring methods.

The correlation for each comparison is given as an R value. The R value represents how correlated the points are in a trend, however, this is not strictly relevant, as even an R value of 1.00 could still show poor consistency between measurement methods. The R value is less relevant than how the line of best fit sits in comparison to the red 1:1 perfect fit line. A line of best fit which more accurately fits with the 1:1 best fit line implies better consistency between the measured values of the two methods being compared.

To quantify this, a displacement value was calculated for each point, which is represented by the shortest distance between that point and the perfect 1:1 line of best fit (Equation 4). This value was then averaged for each region and displayed as a distance alongside the R value (Figure 7-2). A lower distance value suggests that the correlation is closer to the 1:1 line.

As only one point was available for the upper region (Geocube 151), no line of best fit for correlation was possible and an R value was not calculated.

This distance value is quantitatively representative of how much the measurement method over or undermeasures movement compared to the other measurement method.

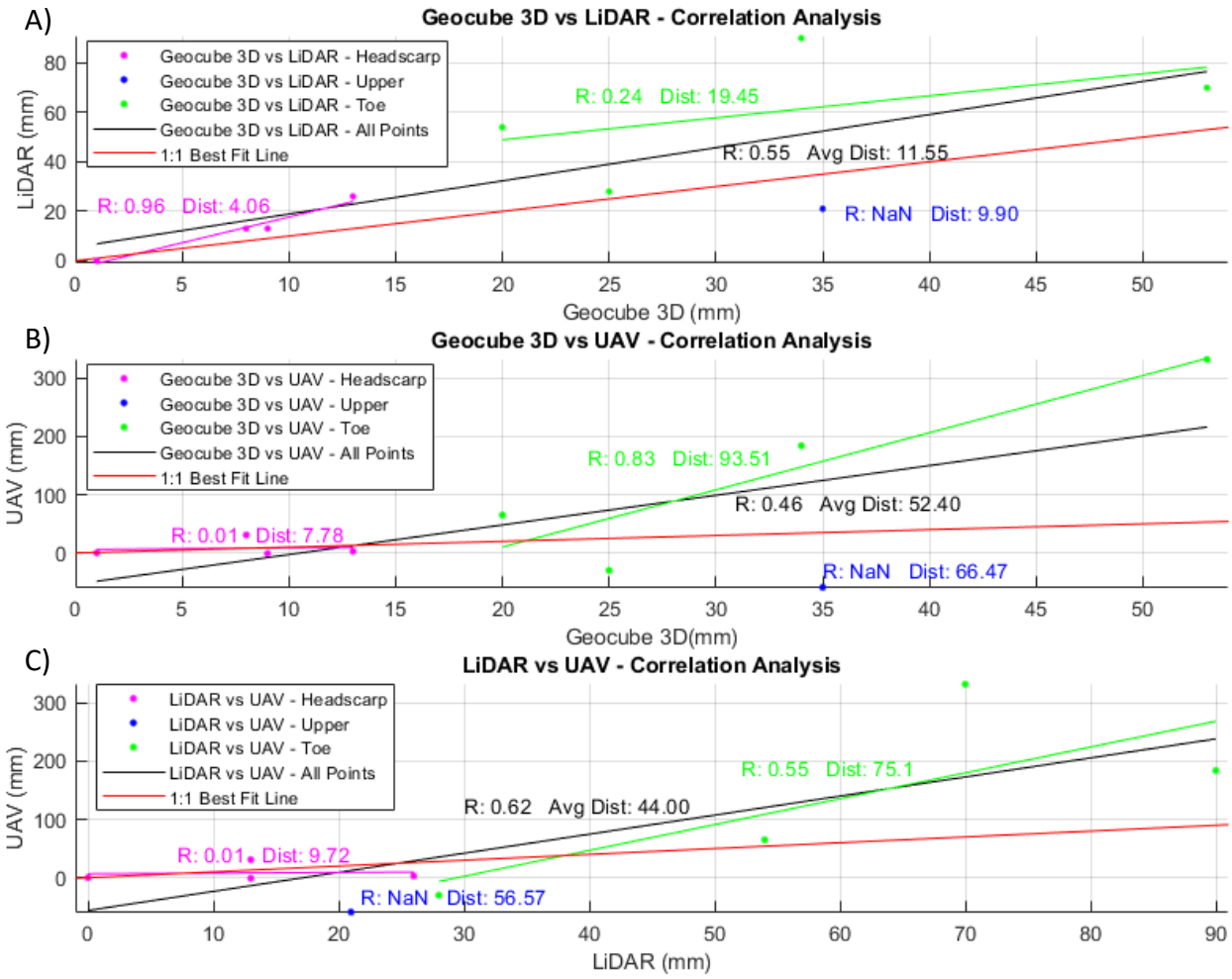

Figure 7-2: Technology results correlation and consistency analysis

Equation 4: Minimum distance between line and a point

$$Line: Ax + By + C = 0 \; and \; Point: (X_1, Y_1)$$

$$1{:}1 \; Best \; Fit \; Line: 1x - 1y + 0 = 0$$

$$Minimum \; Distance = \frac{|AX_1 + BY_1 + C|}{\sqrt{A^2 + B^2}} = \frac{|X_1 - Y_1|}{\sqrt{2}}$$

While the highest R value was found between the LiDAR vs UAV correlation analysis (Figure 7-2C), the lowest average distance (highest consistency) was found between the Geocube 3D movement vs LiDAR correlation (Figure 7-2A). LiDAR over-measured movement by 12 mm on average, compared to GPS measurements.

Measurement method consistency varies by region. Measurements in the headscarp region provide the most consistency, with an average difference of 7 mm, followed by the upper region, with an average difference of 44 mm. The toe region provides the worst consistency with an average difference of 63 mm across all three correlation analyses.

The headscarp region may provide a closer consistency because these locations are stable regions. Stable regions were used to match point clouds during point cloud alignment, and the inconsistency measured in these regions is directly correlated to the LOD of the scan match itself.

The correlation with GPS measurements would improve with better data collection, including LiDAR scanning from a closer distance or improved UAV camera resolution and photography conditions.

Consistency between measurement methods would be expected to be better in fast-moving or non-vegetated landslides or rockfalls. Vegetation reduces the effectiveness of both LiDAR and UAV photogrammetry, decreasing the accuracy of the models and decreasing the consistency when compared to GPS. Very Slow conditions, with short monitoring durations result in movement levels which are quite small. In the case of Chin Coulee, many of the point averages incorporated displacement values which were below the level of detection. While these point

values were incorporated into the average displacement, there is increased error and uncertainty in these values. With larger monitoring durations and increased movement quantities more observed points would be above the level of detection and have less associated uncertainty.

8.0 Development and Kinematics of the Chin Coulee Landslide

This chapter discusses the interpretation of collected data regarding identification of the potential reasons for landslide initiation, evidence in support of the proposed landslide failure mechanism, and discussion behind observed temporal variations in landslide movement.

8.1 Air Photo History of the Chin Coulee Region

In-depth monitoring of Chin Coulee landslide did not begin until 1998. The only source of information regarding landslide initiation derives from air photo interpretation.

The air photos used in this research were obtained from the National Air Photo Library (Government of Canada 2019). These air photos create a visual timeline of landslide evolution and allow for historical monitoring of landslide movement and identification of major movement events and their correlation with local construction works.

Prior to 1960, the only human impact on the natural slope environment of the present-day Chin Coulee landslide was a small cut near the right toe of the slope (Figure 8-1). This cut region is not within the current landslide extents, but the evolution of this cut into a failure region is visible in future air photos.

Air photos taken in 1960 show the realigned Highway 36, which was raised out of the valley floor, up the slope, and above the current landslide extents in the mid 1950's as the reservoir began to fill. Based on inspection of the 1960 air photos, this highway realignment did not require significant cuts or infilling (See Figure 8-2). No slope disturbance was visible within the landslide extents at this time. The cut region from the old highway alignment near the right toe of slope present in the 1945 air photo had developed into a small slope failure by this time.

Between 1960 and 1970, Highway 36 was realigned to create an arc to connect onto a pre-existing northbound range road. During this realignment the highway section directly above the landslide was pushed south and a portion of the current landslide region was infilled and regraded (See Figure 8-3). This major change in topography was identified by AMEC as a potential cause for slope instability due to restriction of drainage (AMEC 2000). No slope disturbance was visible within the landslide extents at this time. Based on air photo

interpretation, water levels within the Chin reservoir appear to be similar to modern day levels at this time.

In the Fall of 1978 a significant slope failure of the Chin Coulee landslide and associated undermining of the northbound shoulder was identified by Alberta Transportation (Golder and Associates 1998). Figure 8-4 shows the first air photo flight completed after the initial failure, taken in 1982. Scarp formations are visible around the periphery of the current landslide region. Movement is most significant in the upper right, with less movement along the left side of the landslide.

Landslide movement continued between 1982 and 1993 with scarp regions on the left and right of the active zone showing significant deformations (See Figure 8-5). Although the headscarp region appeared mostly stable, tension crack formation can be seen at the edge of the road and undermining of the guardrails and road structure was imminent.

In 1997 Alberta Transportation reported significant undermining of the northbound lane on Highway 36 and began continuous annual monitoring of the Chin Coulee landslide in 1998. Figure 8-6 shows a large block near the headscarp which collapsed between 1993 and 1999.

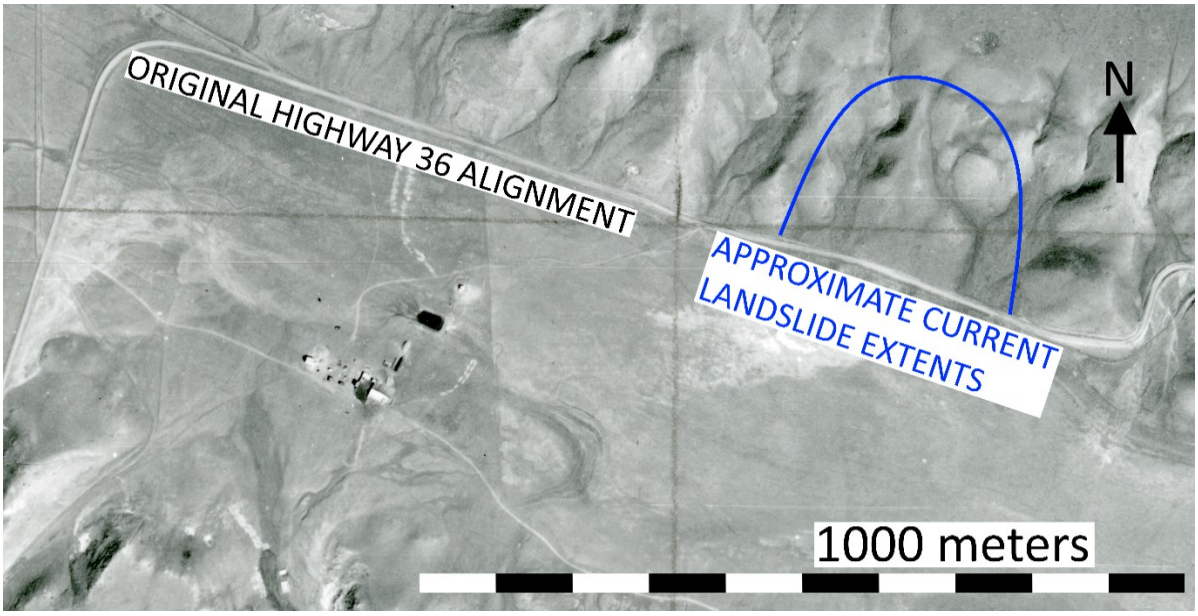

Figure 8-1: 1945 Historical air photo showing original Highway 36 alignment within the now-filled Chin Coulee reservoir (modified from Alberta Air photo Library 1945)

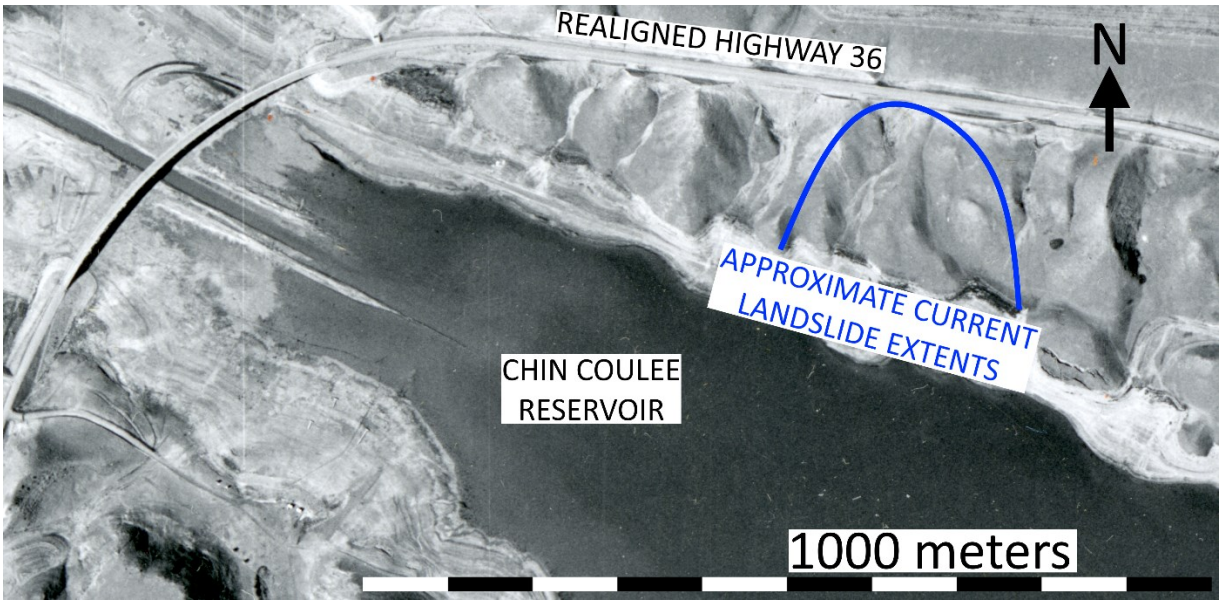

Figure 8-2: 1960 Historical air photo indicating Highway 36 realignment and slope failure near the toe(modified from Alberta Air photo Library 1960)

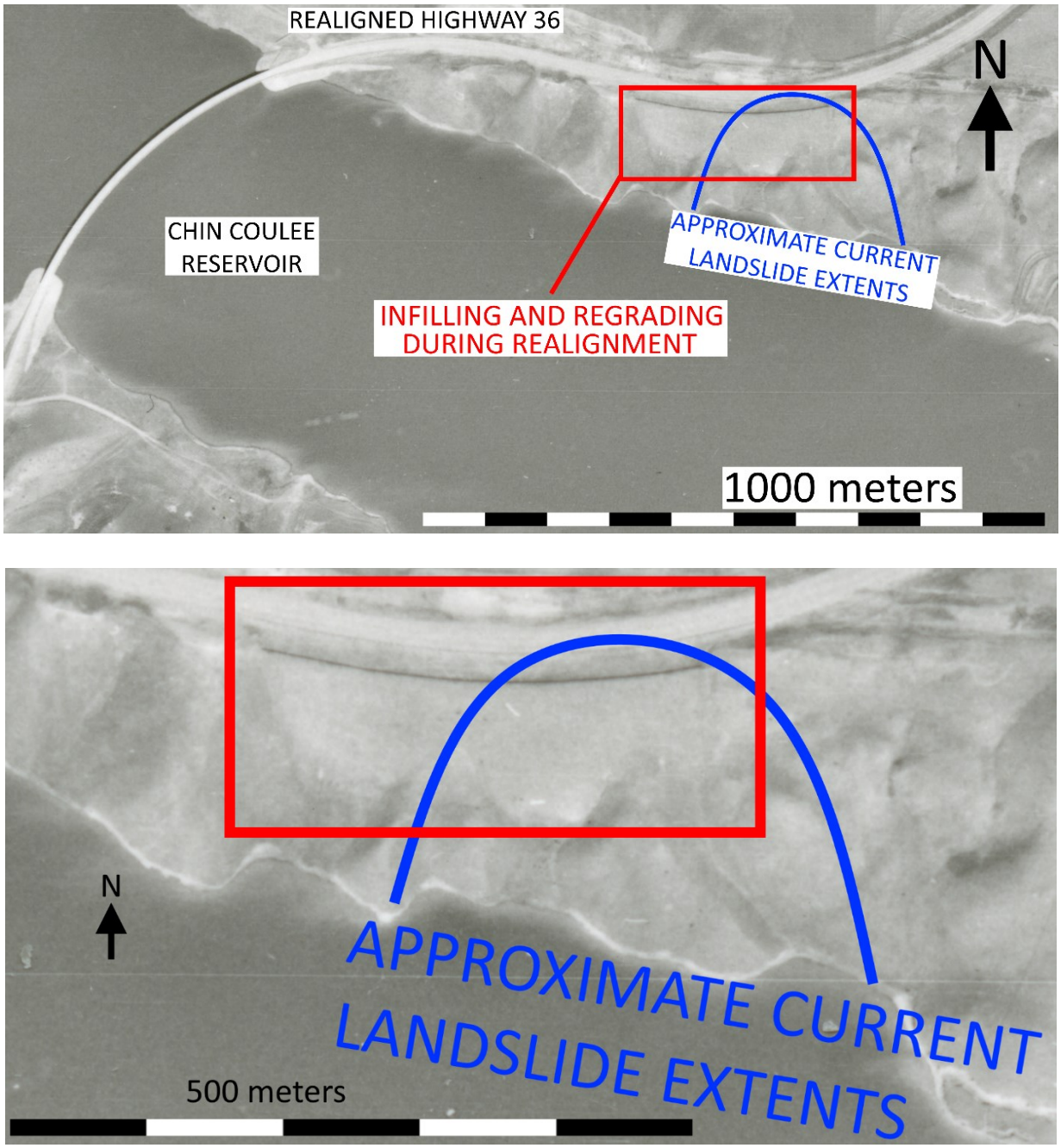

Figure 8-3: 1970 Historical air photo indicating Highway 36 realignment, regrading and potential infilling near the headscarp (modified from Alberta Air Photo Library 1970)

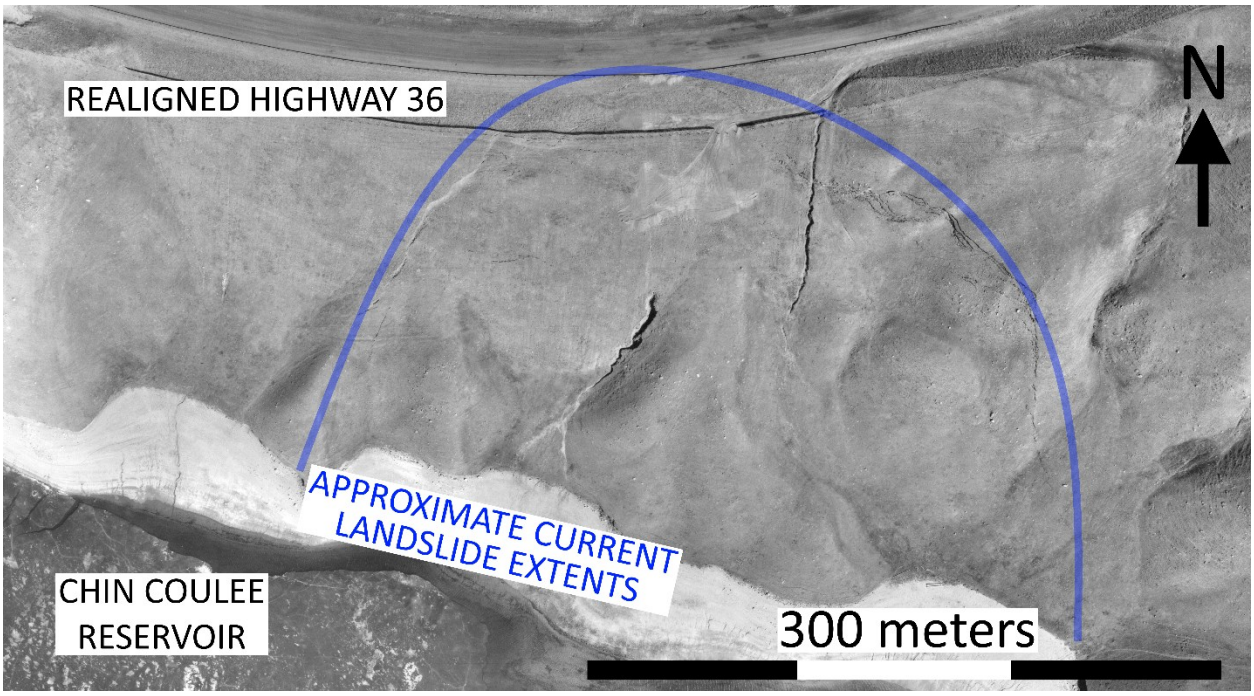

Figure 8-4: 1982 Historical air photo indicating initiation of landslide movement (modified from Alberta Air photo Library 1982)

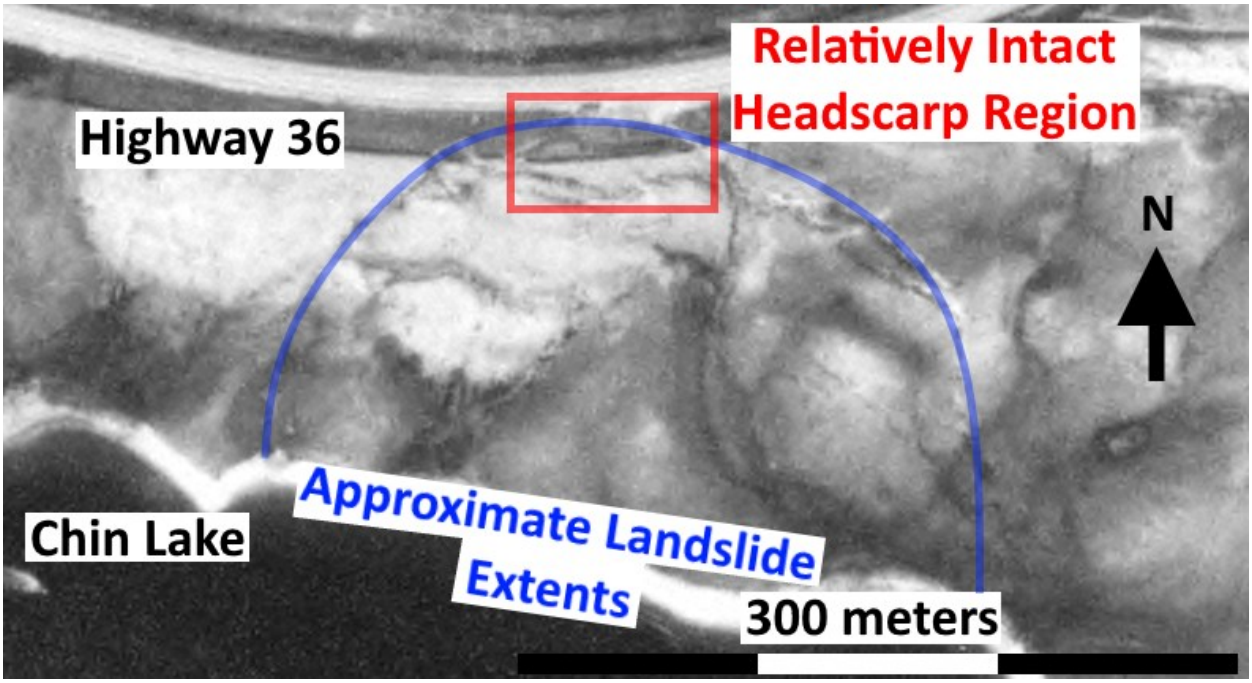

Figure 8-5: 1993 Historical air photo indicating significant advancement of landslide extents (modified from Alberta Air photo Library 1993)

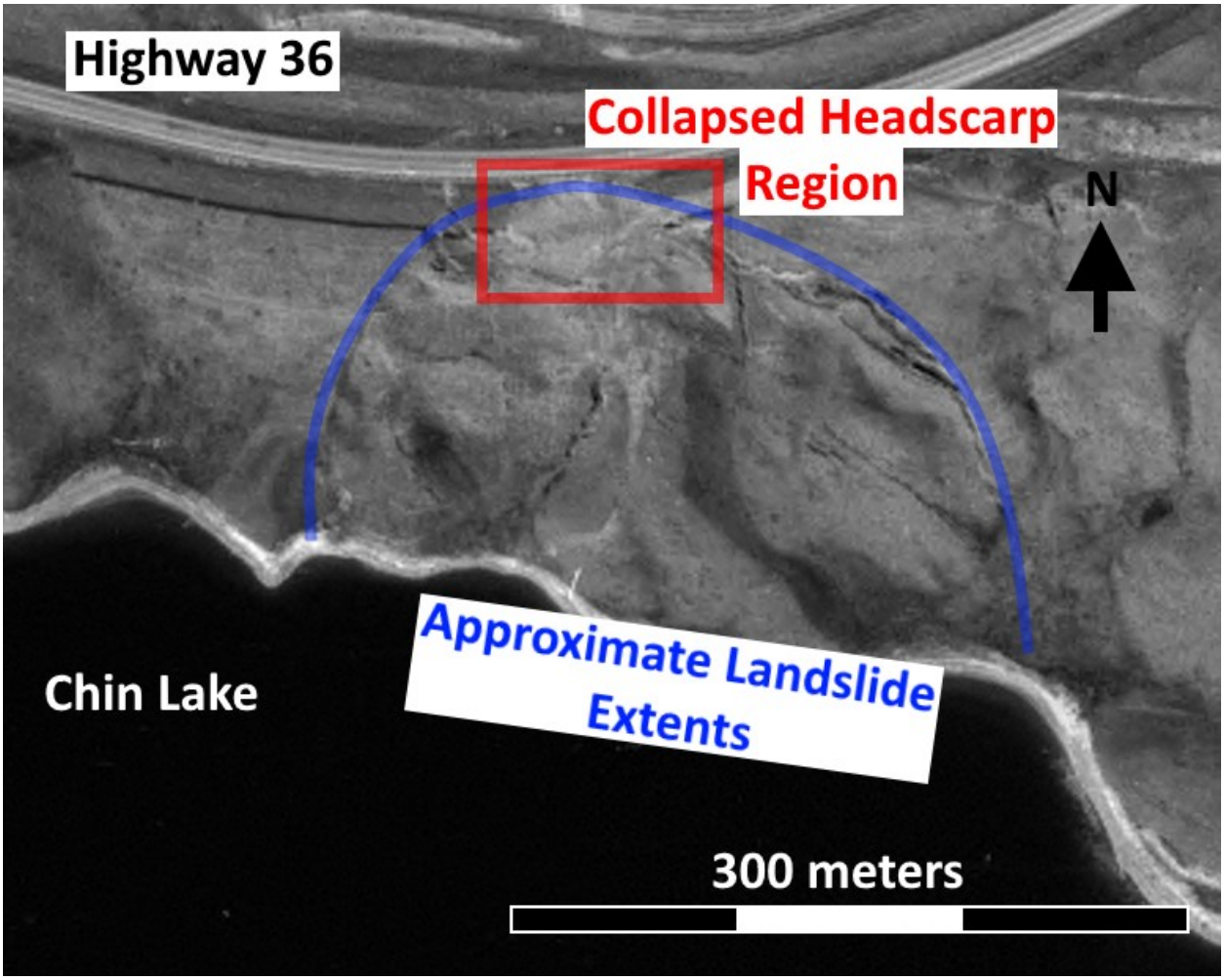

Figure 8-6: 1999 Historical air photo indicating headscarp retrogression (modified from Alberta Air photo Library 1999)

8.2 Landslide Initiation and Contributing Factors

The timeline discussed in Section 8.1 suggests three potential contributing factors for landslide initiation:

1. The initial realignment in the 1950's
2. The second realignment in the 1960's
3. Filling of the reservoir

While the 1950's realignment resulted in additional weight due to the placement of highway material above the landslide, air photo interpretation suggests there was no significant changes to the topography, no reported drainage inhibition was reported, and no damage to the road structure was identified in the following decade prior to the second realignment.

Contrarily, air photo interpretation suggests the 1960's realignment significantly changed the topography above the landslide and significant regrading and infilling was completely to create a berm for the new highway alignment. This process would have led to large amounts of additional soil weight above the landslide and impacted natural surface and groundwater flow paths.

Rising reservoir levels would have exacerbated this effect. Water erosion is prevalent near the shoreline of Chin Lake. 1 – 3 meter cliffs have formed around much of the slope toe as of 2019, although these cliffs were certainly shorter in 1978. Groundwater levels and surface runoff likely rose as the reservoir level rose and began to be used for nearby agricultural watering. Piezometer information shows saturation of soils near the toe of the slope, with high water levels due to the existence of the reservoir.

Figure 8-7 shows the site history of Chin Coulee as it is known from various air photo sets and consultant reports submitted to Alberta Transportation.

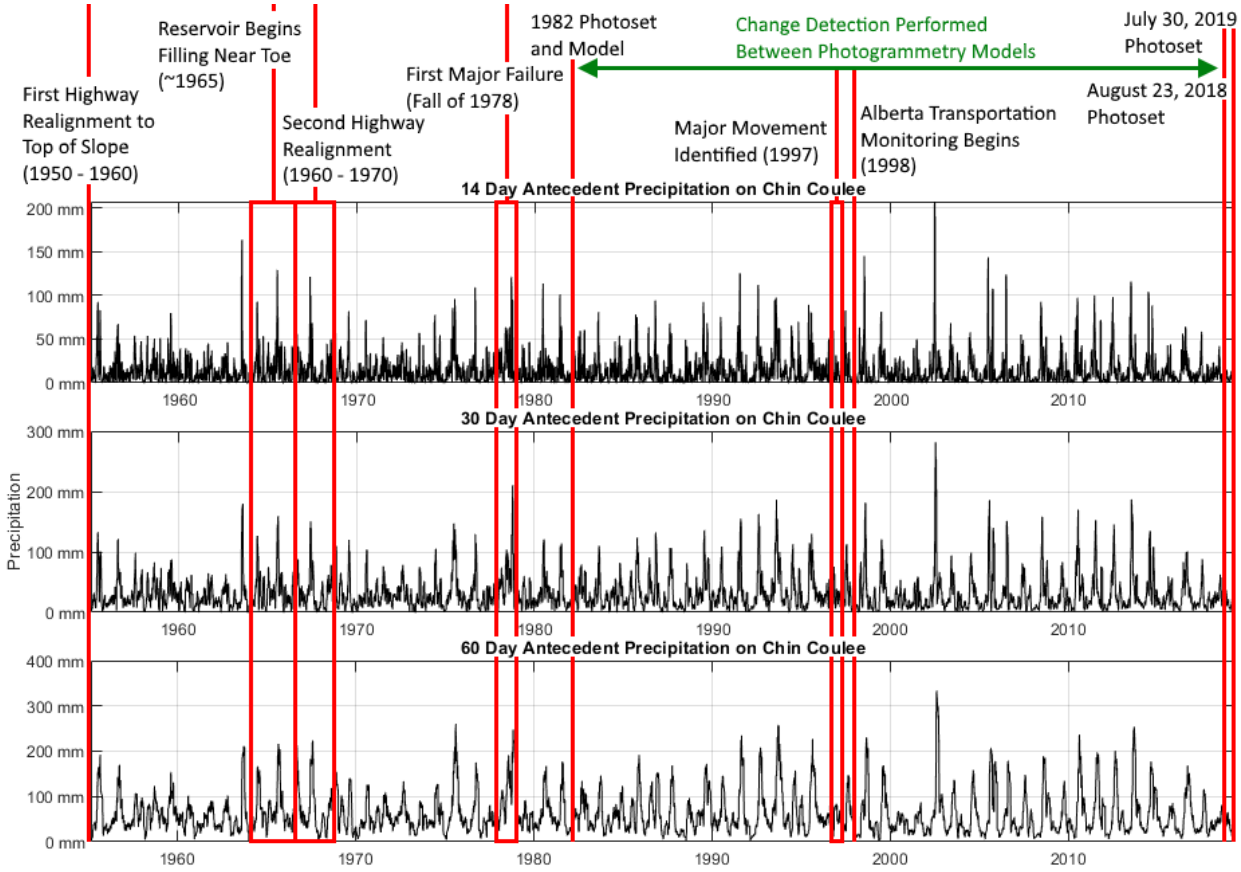

Figure 8-7: Chin Coulee site history and antecedent precipitation from 1955 through 2019

It was reported that the initiation event was likely caused by a significant amount of precipitation which had occurred earlier in the year (AMEC 2000). Historical rainfall analysis shows that the period around late October and early November of 1978 had the second largest 30 day antecedent precipitation on record since 1955 (Alberta Climate Information Service 2019). Although there is no documented specific day for slope failure, it is said to have occurred in the Fall of 1978 following significant precipitation (Golder and Associates 1998). Based on this testimony and precipitation data, landslide initiation likely occurred during the October – November 1978 time frame.

8.3 Landslide Failure Mechanism

GPS, LiDAR, UAV, and historical photogrammetry supports the hypothesized compound failure mechanism of the Chin Coulee landslide. A compound failure mechanism is one which is a combination of typical failure methods such as rotational or translational sliding, lateral spreading, or flows. This failure method is used when the expression of the landslide does not fit a single description. In the case of Chin Coulee, failure is not purely translational, as the upper region is not moving with the lower toe region. There is evidence of lateral spreading, although it is not the predominant failure mechanism. The movement is complex and is best classified as a compound mechanism.

Compound movement can be observed from GPS data by overlaying Geocube movements on a typical cross section. Figure 8-8A outlines the process in which Geocubes were translated onto the cross-section A-A shown in Figure 8-8B. Geocubes 153, 154, 174, and 177 were not included in the cross-section due to the distance in which they would need to be relocated and the redundancy in including multiple Geocubes above the headscarp which were not showing large amounts of movement.

Geocubes located above the headscarp (152 and 173) show little movement vertically or horizontally.

Based on the proposed failure mechanism, Geocube 151 would be located within a horst-like region and a downwards displacement is expected. Observed Geocube 151 movements agree with this, showing downward vertical movement along with horizontal movement likely associated with displacement along the back sliding plane (Figure 8-8).

Geocube 172 would be located in a graben-like region, and exhibits expected movement patterns with considerable horizontal displacement with some vertical uplift, due to the expected failure plane (Figure 8-8). Closer to the toe of the slope, Geocube 176 exhibits a similar movement pattern.

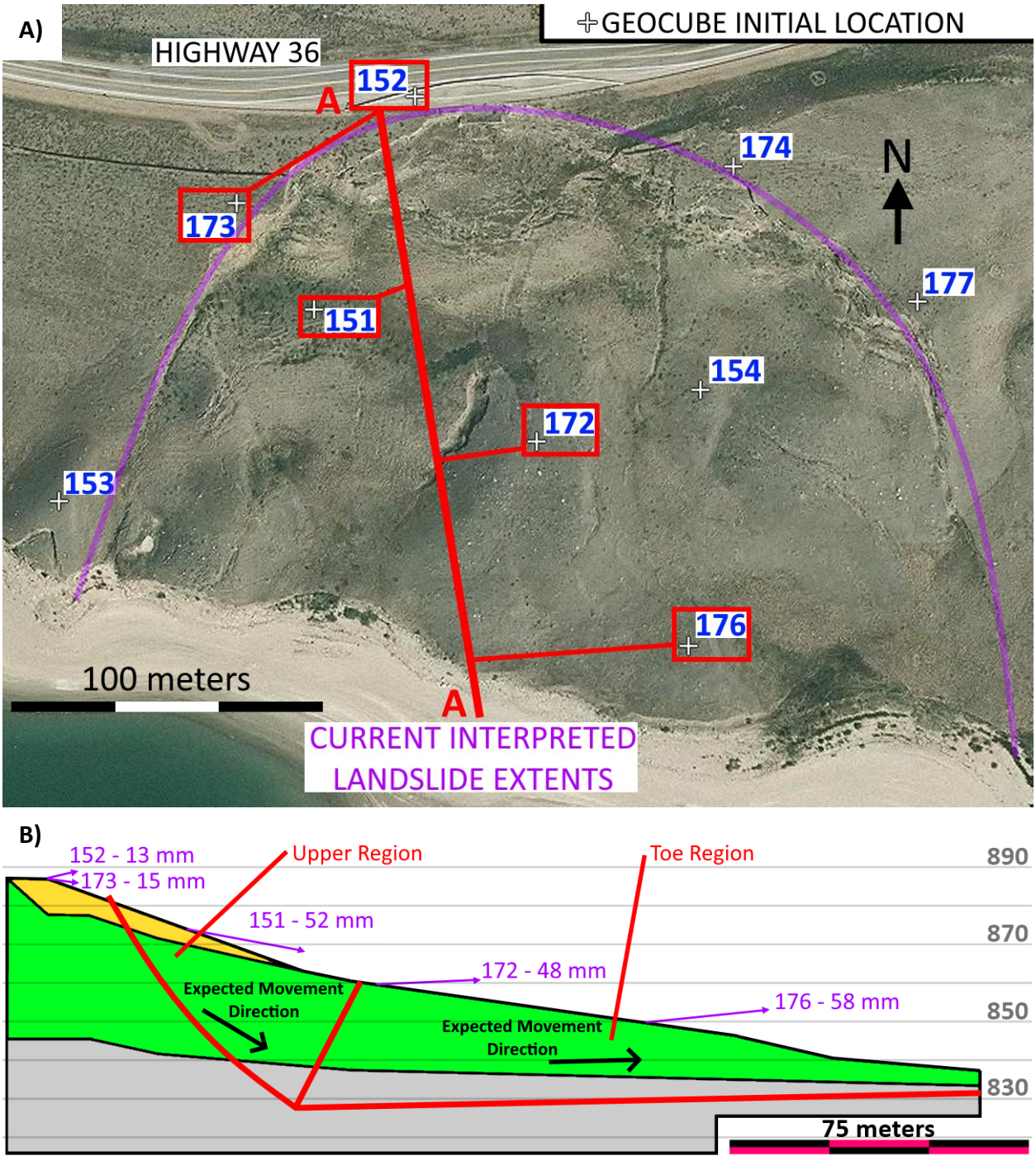

Figure 8-8: Geocube cross-sectional displacements (Base imagery from ESRI, 2019)

LiDAR and UAV data shows additional evidence of this compound failure mechanism, with distinct regions of movement being observed. These regions of movement are consistent

between LiDAR and UAV, and depict an upper region dominated by subsidence, with a toe region dominated by uplift and lateral translation. Although there is quantitative inconsistency between the three monitoring methods, as shown in Chapter 7, qualitatively, regions shown in Figure 8-9 and Figure 8-10 match Geocube observations (Figure 8-8).

Historical photogrammetry analysis (See Figure 6-2) also shows typical compound landslide movement. No discernible toe of the failure is visible within any of the monitoring methods, suggesting that the toe daylights within the reservoir.

With increased monitoring durations, more regions within LiDAR and UAV data will begin to show movement above the LOD, allowing for more accurate interpretations of displacement and displacement regions.

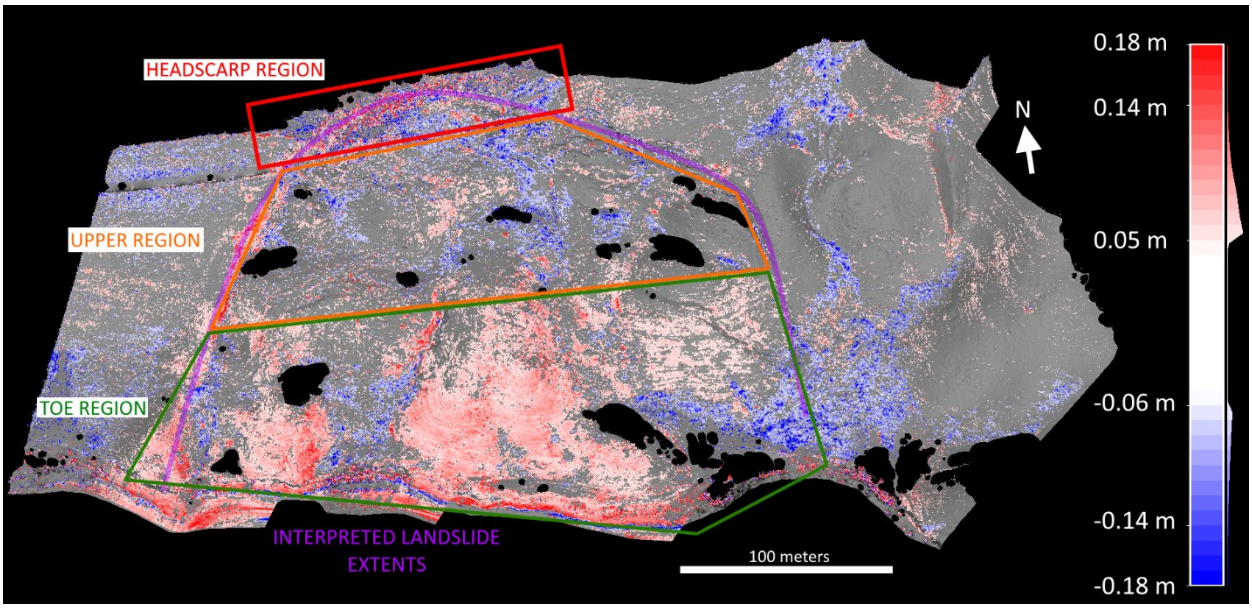

Figure 8-9: LiDAR change detection on Chin Coulee between August 23, 2018 and July 29, 2019 showing region definitions

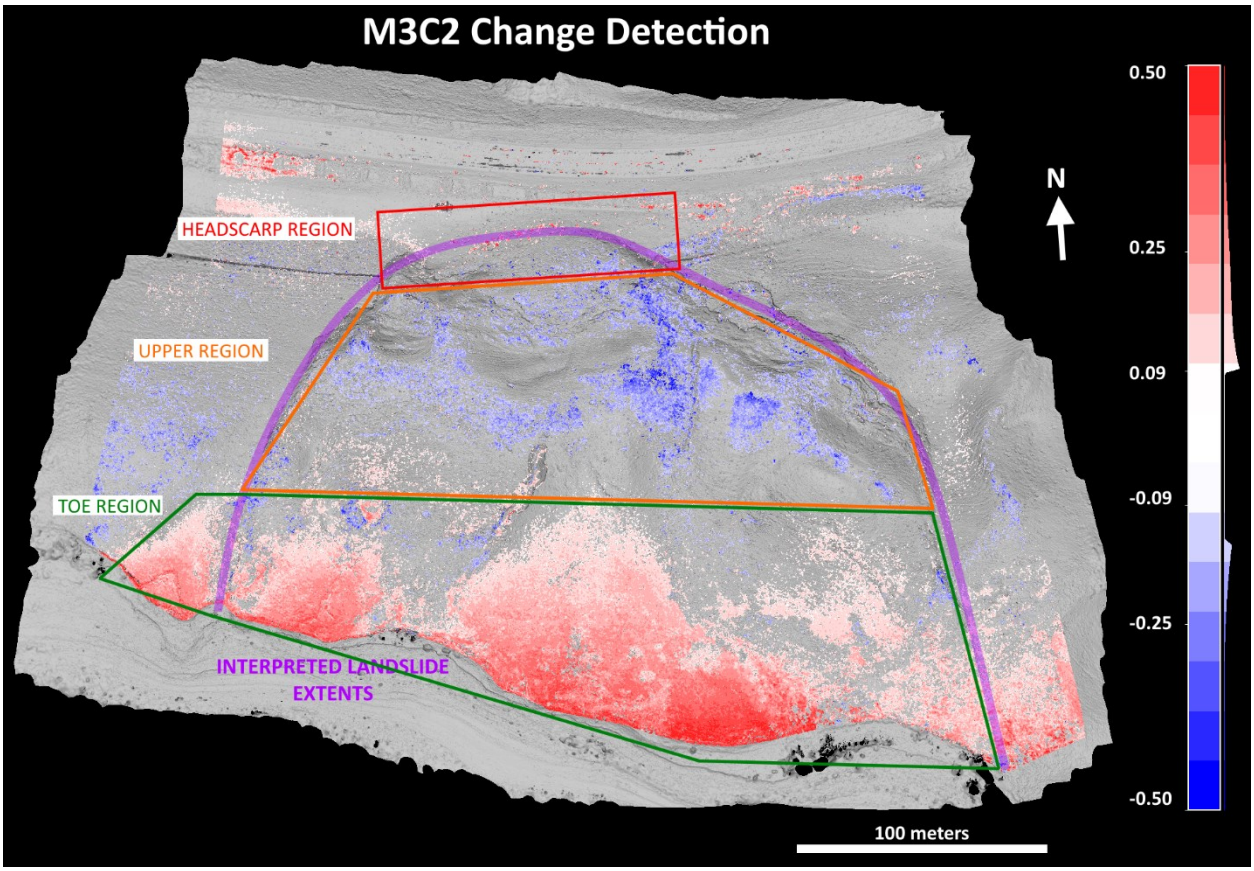

Figure 8-10: UAV change detection on Chin Coulee between August 23, 2018 and July 29, 2019 showing region definitions

8.4 Temporal Variation of Landslide Velocity

Seasonal variation in landslide velocity was observed in active zone Geocubes. This seasonal variation coincides with reservoir changes on Chin Lake. Agricultural water usage increases during the months of June, July, and August, which leads to reservoir drawdown. GPS movement is also observed to increase during these drawdown periods (Figure 8-11). Figure 8-12 shows the average reservoir level throughout the year.

In the case of Geocube 176, movement from July 11, 2018 to September 10, 2018 showed an annualized horizontal displacement of 41 mm/year. In comparison, from June 5, 2019 to July 1, 2019, (During reservoir drawdown) an annualized horizontal displacement of 322 mm/year was observed. Average yearly movement for this Geocube is 60 mm.

In October and November of 2018, after the reservoir level stabilized, increased movement was observed in Geocube 176. This movement event may be due to antecedent rainfall, as shown by persistent 30-day antecedent rainfall occurring in early October (See Figure 8-11).

With the current monitoring period, it is not certain whether the observed movement patterns are associated with the reservoir or precipitation as only one drawdown cycle has been recorded. Additional years of monitoring are required in order to provide more evidence for these hypothesized driving mechanisms.

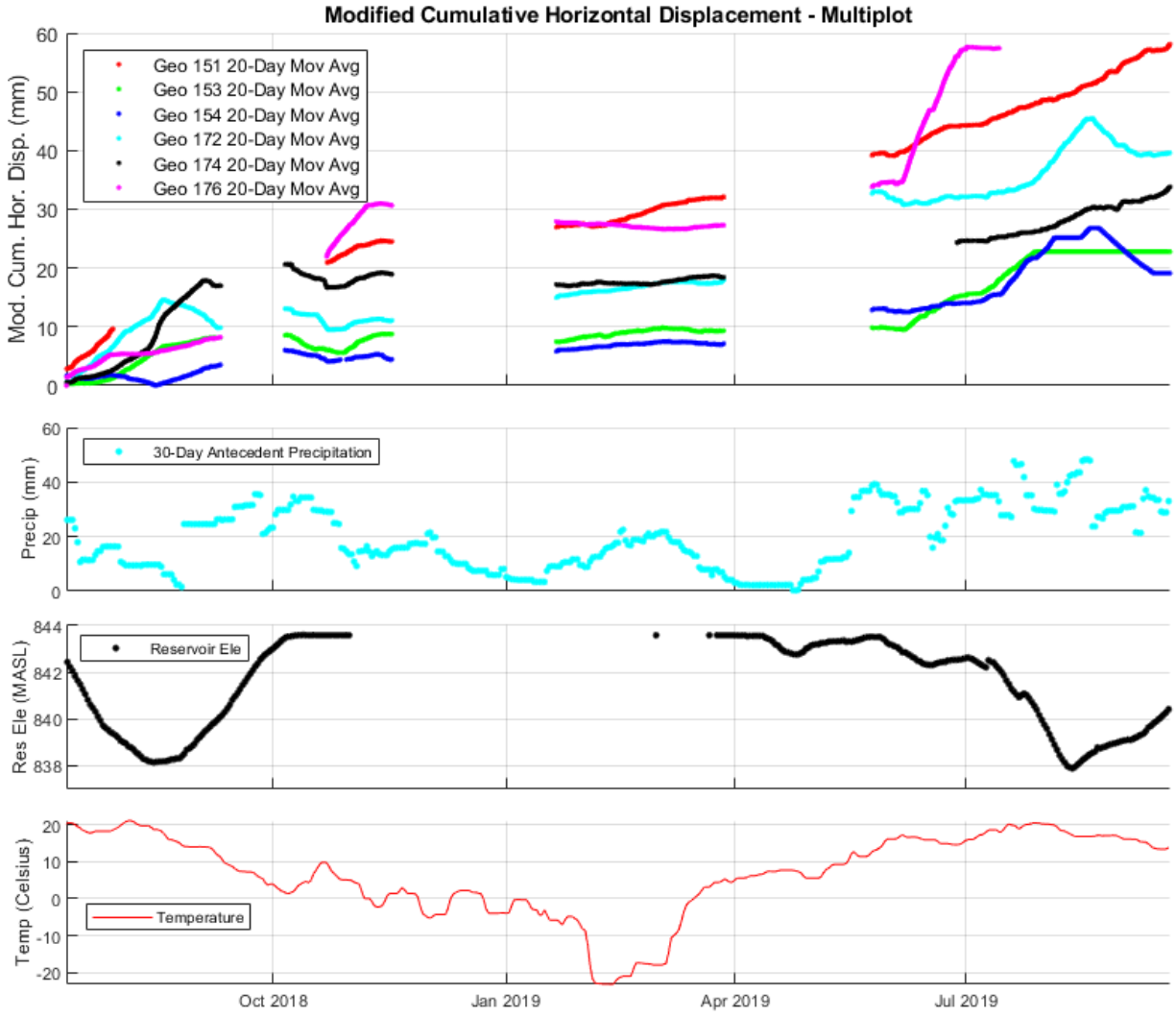

Figure 8-11: Geocube horizontal displacement in-depth analysis

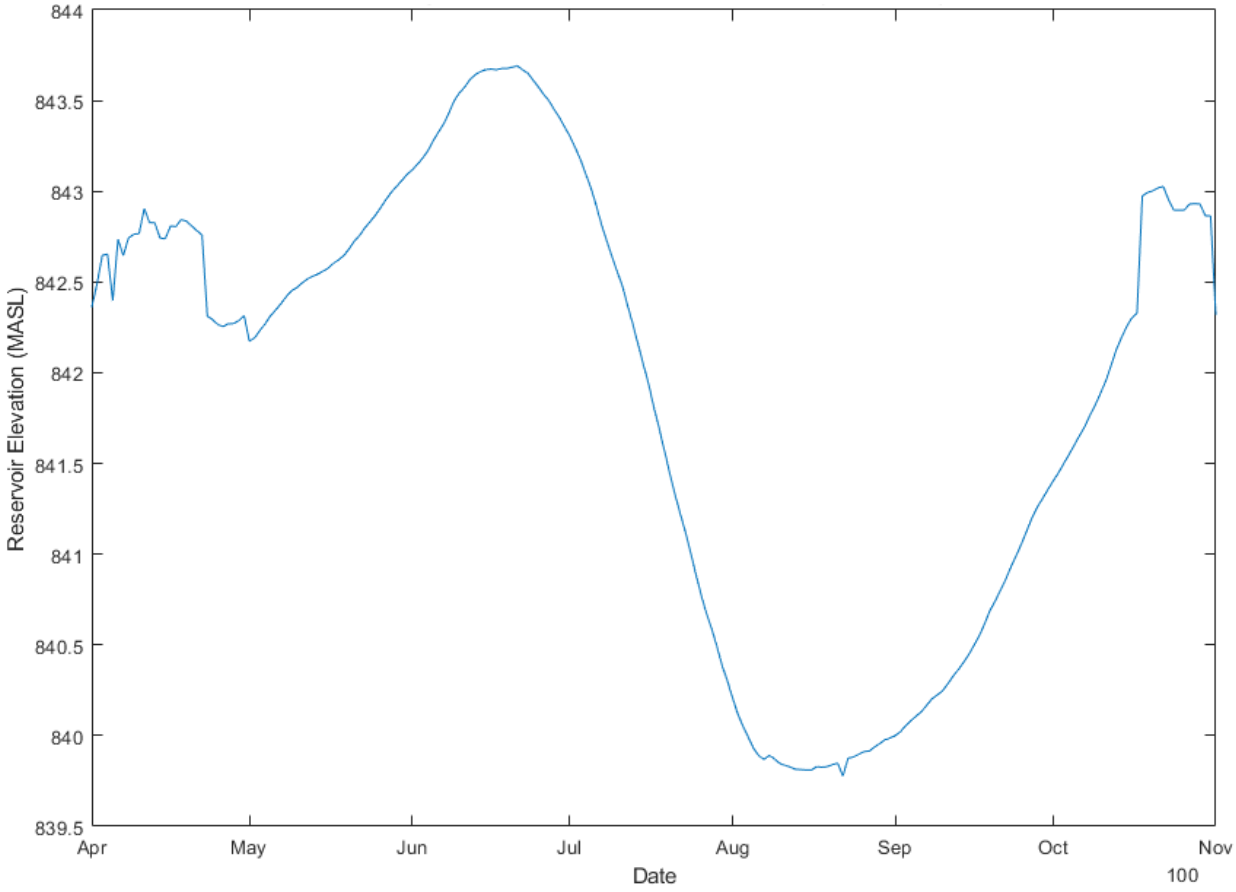

Figure 8-12: Chin Lake average reservoir elevation from 1994 to 2019 (Saint Mary's River Irrigation District 2019)

GPS unit observations provide strong support for the association of reduced reservoir levels and increased movement on Chin Coulee. Two potential mechanisms are drawdown in the water table near the toe of slope or the loss of buttressing. A better understanding of the impact these two potential mechanisms will have on stability is crucial for reducing potential instability of Chin Coulee and predicting periods of increased movement and will help inform decision making for future remediation.

8.4.1 The Use of Slide 7.0 Analysis for Assessment of Landslide Driving Processes

Variation in reservoir elevation has been shown to lead to variation in landslide velocity and factor of safety for landslides similar to Chin Coulee. In 2015, Hendry et al. used GPS displacement monitoring and water level monitoring to show that lower water levels in the

Thompson River resulted in increased rates of displacement on the adjacent Ripley Slide. Hendry et al. confirmed this using LEM analysis to show that lower reservoir elevations lead to lower factors of safety.

It is believed that a similar phenomenon is occurring on the Chin Coulee landslide and modelling analysis was employed to investigate.

8.4.1.1 Methods and Software

The software used for this research was Slide 7.0 (Rocscience Inc. 2019). The typical cross section used was based on borehole logs (See Figure 3-4), with the slope surface based on LiDAR scans performed in August 2018. Soil parameters for Clay Fill and Clay Till were based on direct shear and triaxial test results completed in 2015 by AMEC Foster Wheeler (AMEC FW 2015). Bedrock (Shale, Siltstone, and Sandstone) and weakened bedrock properties were based on three reports: The Chin Coulee stability report submitted to Alberta Transportation by AMEC FW in 2015, a report submitted to the Milk River Watershed Council of Canada during construction of a dam in Southern Alberta, 50 km south of Chin Coulee, and a report submitted to Alberta Environment from Golder and Associates for the Meridian dam 215 km north east of Chin Coulee (AMEC FW 2015; Prairie Farm Rehabilitation Administration 1986; Golder Associates 2002).

Shale properties on these sites and Chin Coulee are assumed to be similar. All shales were within the Foremost Formation, and the sites are close to Chin Coulee landslide. Permeability estimates were based on the particle grain size distribution of Clay Till material at a depth of 14.0 m in borehole 2015-01 (Table 8-1). USCS classification labels this Clay Till material as a low plasticity clay (CL). Based on gradation, expected hydraulic conductivity ranges from $1x10^{-6}$ to $1x10^{-9}$ m/s (Association of Swiss Road and Traffic Engineers 1999).

Table 8-1: Clay Till gradation from borehole 2015-01 at depth of 14.0 m (AMEC FW 2015)

Soil Group	**Percent Makeup**
Gravel	3 %
Sand	30 %
Silt	42 %
Clay	25 %

8.4.1.2 Influence of Permeability

To validate the estimated permeability range, a sensitivity analysis using permeability was performed to observe the impact of different permeabilities on the groundwater table during drawdown.

Piezometers installed in GA98-4 and GA98-5 near the toe of the slope (See Figure 3-3) suggest that the water table near the reservoir does not drastically change throughout the seasonal drawdown periods (Figure 8-13). Likewise, an appropriate permeability for modeling should show little variation in groundwater level throughout the slope during drawdown.

This sensitivity analysis was performed using Slide 7.0 transient groundwater finite element modeling (FEM) analysis (Rocscience Inc. 2019). Transient analysis was completed using a steady state groundwater scenario followed by a transient groundwater scenario to model reservoir drawdown.

The steady state groundwater table was created from piezometric information available from GA98-4, GA98-5, and BH2002-02 (See Figure 3-3). Based on average initial and final reservoir elevations, a drawdown from 844 to 839 MASL was selected. A drawdown duration of 55 days was selected based on the historical average (Figure 8-12).

The regional groundwater state was assumed to not be influenced by drawdown and was set as a constant boundary condition. Figure 8-14 shows the FEM element and boundary conditions for the steady state and final transient state.

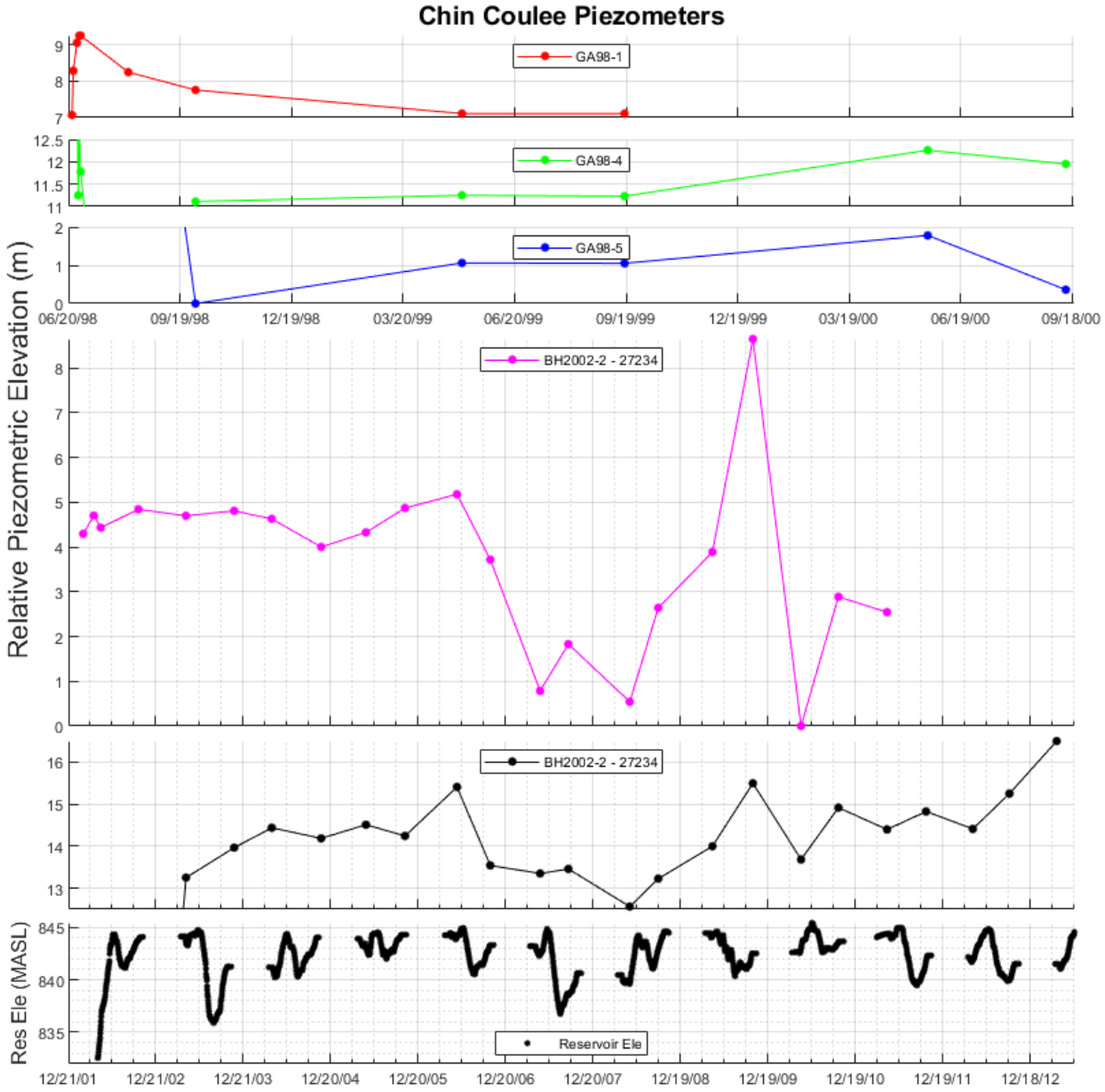

Figure 8-13: Chin Coulee piezometers and standpipes (After Golder and Associates 1998; AMEC FW 2015)

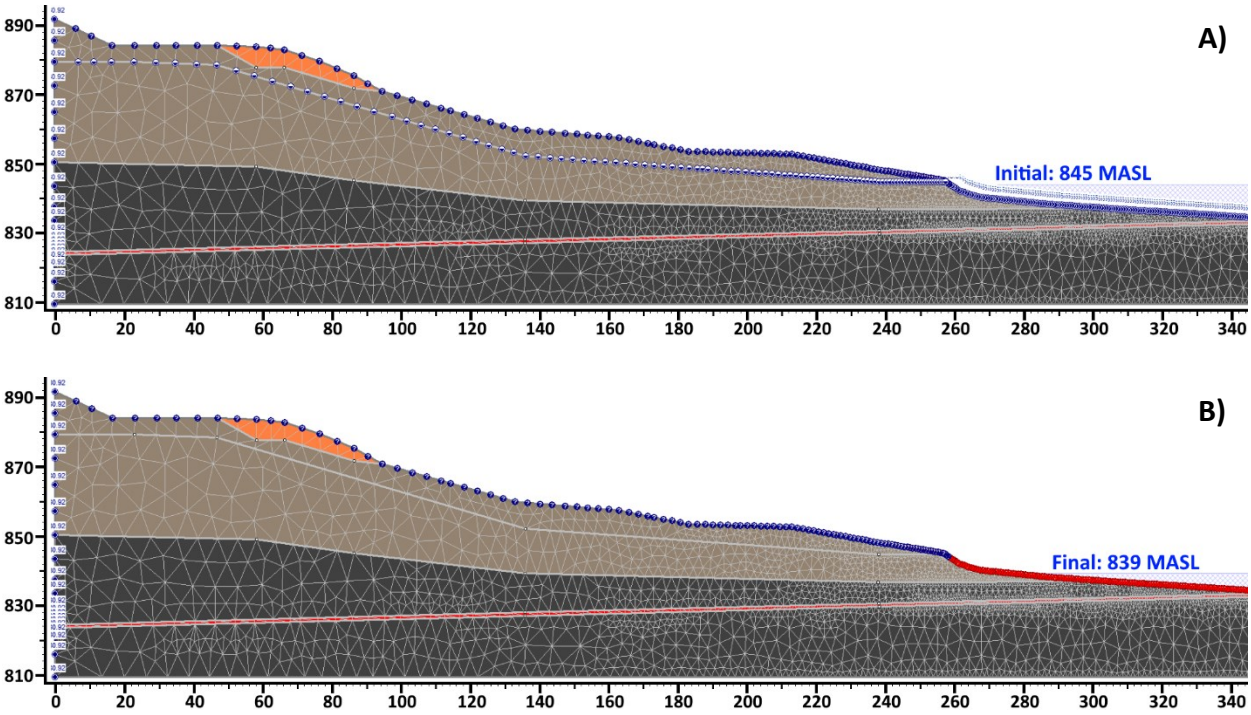

Figure 8-14: Initial (Steady State) (A) and final (Transient) (B) reservoir states for permeability sensitivity analysis

The results of this sensitivity analysis is shown in Figure 8-15.

With Clay Till permeability values above $1x10^{-7}$ m/s, the water table fluctuates considerably during drawdown. Permeability values of $1x10^{-7}$ m/s and below show little variation with time, becoming increasingly rigid to the initial steady state water table with decreasing permeability. A permeability of $1x10^{-5}$ m/s results in the groundwater table reaching the surface throughout much of the landslide. This disagrees with field observations. Similarly, with a permeability of $1x10^{-6}$ m/s, groundwater levels throughout the slope are higher than that observed at any point in time within piezometers GA98-4 and GA98-5.

Drawdown analysis suggests that permeabilities of $1x10^{-7}$, $1x10^{-8}$, and $1x10^{-9}$ m/s and below result in practically identical groundwater curves. Any permeability $1x10^{-7}$ m/s and below would sufficiently mirror observed piezometer information and the associated water table fluctuation during drawdown. A permeability of $1x10^{-7}$ m/s was selected from this narrowed range of potential permeabilities.

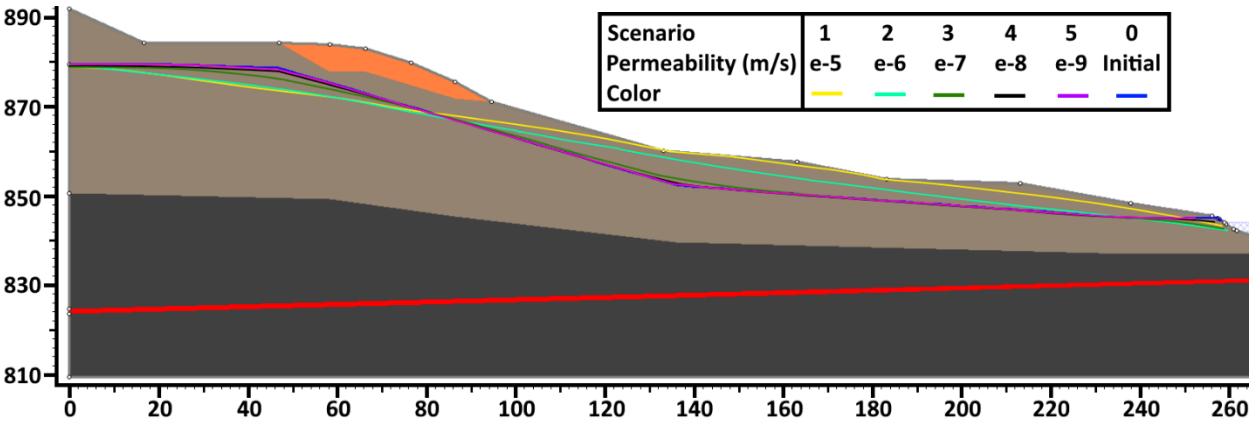

Figure 8-15: Chin Coulee Clay Till permeability sensitivity analysis (5 meter drawdown over 55 days)

Table 8-2 shows the selected soil parameters for all subsequent analysis. Unit weights and friction angles were determined from borehole investigations and testing conducted by AMEC FW in 2015, as well as reports from Prairie Farm Rehabilitation Administration and Golder and Associates (AMEC FW 2015; Prairie Farm Rehabilitation Administration 1986; Golder Associates 2002). Cohesion values of 0 kPa were selected for all materials as stability analysis is concerned with continued movement along existing shear planes.

Table 8-2: Soil properties used in subsequent Slide 7.0 analyses

Material	**Unit Weight (kN/m^3)**	**Permeability (m/s)**	**Cohesion (kPa)**	**Phi (°)**
Clay Fill	21	$1x10^{-7}$	0	27.5
Clay Till	21	$1x10^{-7}$	0	25.6
Shale/Siltstone/Sandstone	22	$1x10^{-10}$	0	30
Coal Seam/Slip Plane (Moistened Shale)	21	$1x10^{-10}$	0	11

8.4.1.3 Influence of Reservoir Drawdown

Transient drawdown analysis using data from the reservoir cycles of 2018 and 2019 was completed to investigate the influence of reservoir drawdown on landslide stability. The initial water table was determined from piezometer data and allowed to vary with time as drawdown occurred.

Drawdown in 2018 began on June 21 at a reservoir level of 844.7 MASL. Drawdown continued for 55 days until August 15 at a reservoir level of 838.1 MASL. This corresponds to an average drawdown rate of 12 cm/day. During this drawdown period an annualized horizontal displacement of 81 – 136 mm/yr was observed in active zone Geocubes (See Figure 4-18).

Drawdown in 2019 began on July 2 at a reservoir level of 842.6 MASL. Drawdown continued for 41 days until August 12 at a reservoir level of 837.9 MASL. This corresponds to an average drawdown rate of 11.5 cm/day. Movement patterns in Geocube 154 and 172 depicted acceleration as drawdown proceeded, and an annualized horizontal displacement of 54 – 162 mm/yr was observed in active zone Geocubes (See Figure 4-18).

Transient drawdown results for 2018 and 2019 drawdown cycles are shown in Figure 8-16 and Figure 8-17. Factor of Safety was calculated using the Morgenstern Price method available within Slide 7.0. The Morgenstern Price method is a method of slices in which both force equilibrium and moment equilibrium is satisfied (Morgenstern and Price 1965).

2018 drawdown results suggest a 7 % reduction in factor of safety from 1.06 to 0.99. 2019 drawdown results suggest a 6 % reduction in factor of safety from 1.06 to 1.00. This suggests that reservoir drawdown does play a role in landslide stability on Chin Coulee.

A state of drawdown was modelled using the historically largest possible drawdown rate and is shown in Figure 8-18. Parameters for this critical state were selected based on a hypothetical worst-case scenario. Drawdown begins at a reservoir elevation of 845 MASL, the historical maximum recorded water level, and continues for 50 days to a reservoir elevation of 835 MASL, the typical minimum recorded water level. This hypothetical scenario corresponds to an average drawdown rate of 20 cm/day, slightly higher than the largest historical drawdown rate

of 19 cm/day, which occurred in 2017. Critical drawdown results suggest an 8% reduction in factor of safety from 1.06 to 0.98.

Drawdown analysis results are summarized in Table 8-3.

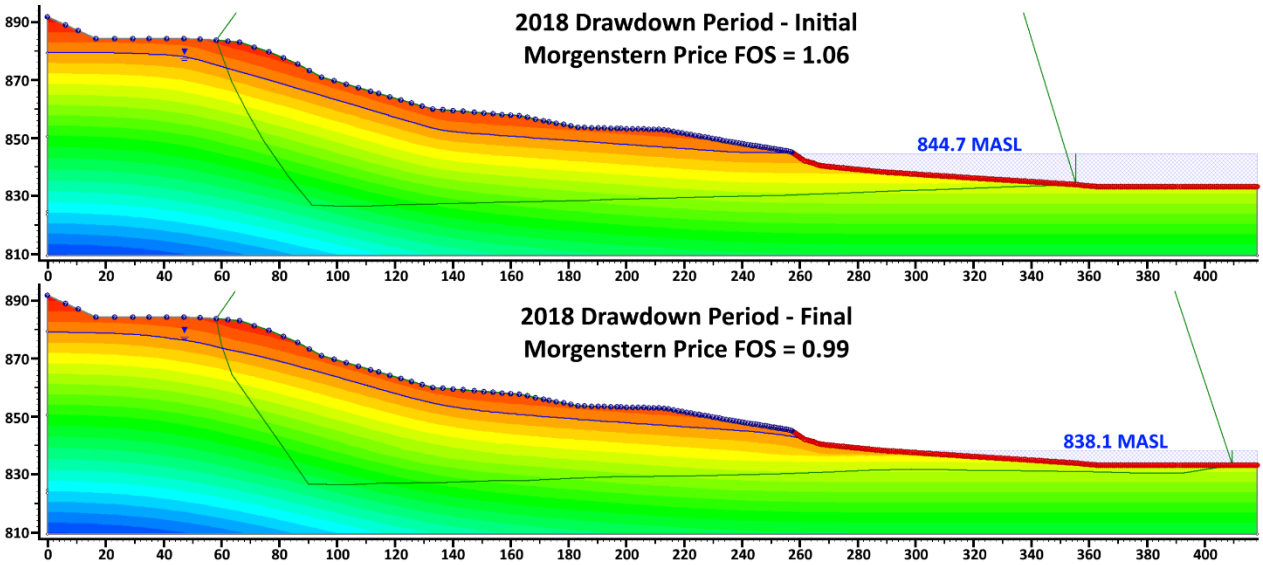

Figure 8-16: Chin Coulee 2018 drawdown stability analysis

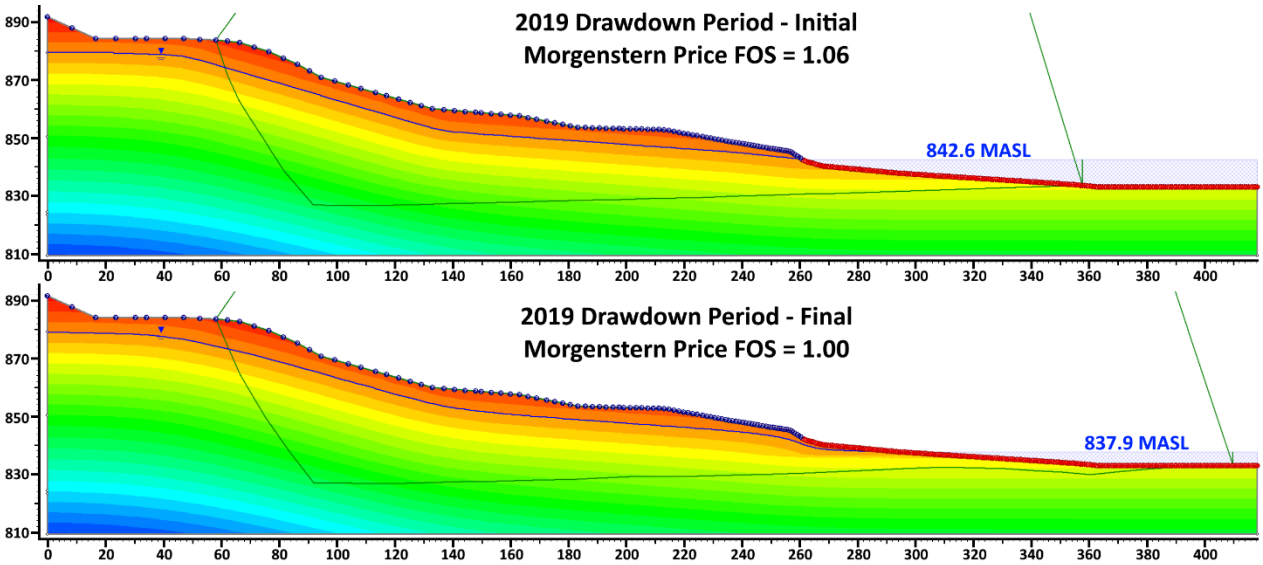

Figure 8-17: Chin Coulee 2019 drawdown stability analysis

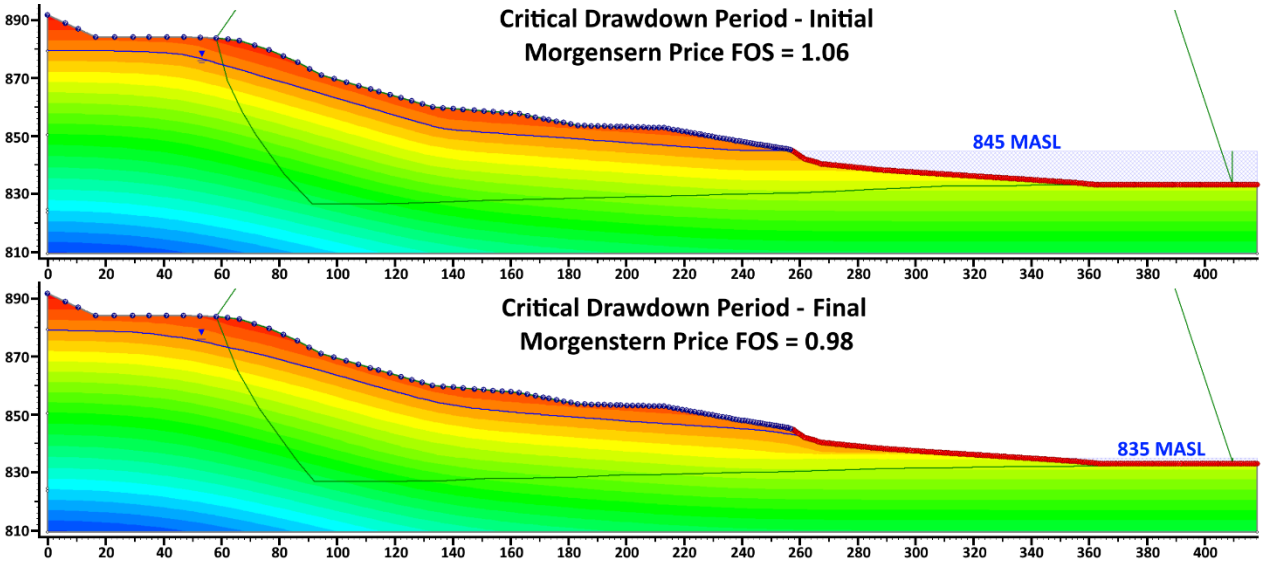

Figure 8-18: Chin Coulee critical drawdown stability analysis

Table 8-3: Chin Coulee reservoir drawdown analysis - Results summary

Scenario	Initial Res Ele (MASL)	Final Res Ele (MASL)	Duration (Days)	Drawdown Rate (cm/day)	Initial FOS	Final FOS	Reduction	GPS Velocity (mm/yr)
2018	844.7	838.1	55	12	1.06	0.99	7 %	81 – 136
2019	842.6	837.9	41	11.5	1.06	1.00	6 %	54 – 162
Critical	845.0	835.0	50	20	1.06	0.98	8 %	N/A

Drawdown analysis results suggests a 6 – 8 % reduction in factor of safety due to reservoir drawdown, from a maximum factor of safety of 1.06 to a minimum factor of safety of 0.98.

Factor of safety reduction varied from 2018 to 2019 due to changes in the drawdown duration and reservoir characteristics (initial and final elevation). The difference in final elevation of both drawdown periods is only 20 cm and is likely insignificant.

The calculated factor of safety reduction in 2018 was larger than 2019. The observed drawdown rate was also higher in 2018, suggesting that increased drawdown rate results in decreased stability. This calculated difference in factor of safety agrees with field observations of GPS movement during the respective drawdown periods, which showed increased movement during the 2018 drawdown cycle.

The critical drawdown scenario also supports these findings, showing a further reduction in factor of safety with a larger drawdown rate. As this scenario is only hypothetical there are no associated GPS velocities for comparison.

8.5 Summary of Insights

Initial landslide failure appears to be the result of the realignment of Highway 36 during the 1960's. This realignment required the creation of a berm which increased the soil load above the headscarp and blocked surficial flow paths. This occurred simultaneously with rising reservoir levels, which may have resulted in weakening of shale bedrock material, eroded parts of the slope toe, and increased soil saturation.

GPS, LiDAR, and UAV photogrammetry change detection results support the proposed compound failure mechanism, indicating the presence of a sliding wedge located in the upper region of the landslide, driving the lateral movement of the toe region. Change detection completed with a model created from 1982 air photos also supports this failure mechanism.

Continued movement appears to be correlated with reservoir elevation fluctuations, with significantly increased movement occurring during drawdown of the reservoir. For example, horizontal displacement of Geocube 176 during drawdown showed peak velocities in excess of 320 mm/yr, significantly more than the average velocity of 60 mm/yr for this Geocube. Increased movement recorded in October does not appear to be correlated with drawdown and may be related to increased precipitation. Additional monitoring is required in order to observe additional reservoir and precipitation cycles and fully understand the driving forces for continued movement.

Limit equilibrium modeling using Slide 7.0 supports the influence reservoir elevation plays in landslide stability. A reduction in factor of safety of 6 – 8 %, from 1.06 to 1.00, 0.99, and 0.98 was observed when modeling transient drawdown of the reservoir based on the 2019, 2018, and hypothetical critical drawdown periods, respectively. Corresponding horizontal GPS velocities during these drawdown periods showed 54 – 162 mm/yr in 2019 and 81 – 136 mm/yr in 2018. While the sample size is small, this suggests that movement levels during the 2018 drawdown period were larger, which agrees with the greater reduction in factor of safety from modelling results.

Additional monitoring of drawdown and recorded GPS velocities are required in order to confirm this association.

9.0 Conclusions

The purpose of this research was to understand and quantify the limitations of differential GPS, LiDAR-based change detection, and UAV-based change detection on Very Slow, vegetated landslides. This was achieved using a test site in Southern Alberta called the Chin Coulee landslide. An in-depth historical review of the initiation and continued movement of the Chin Coulee landslide was performed with the goal of increasing the understanding of landslide movement trends and mechanism. The primary observations and conclusions from this research are summarized below, by section:

9.1 Differential GPS

Differential GPS provided a means of continuous and remote data collection on Chin Coulee and allowed for the discovery of the correlation between reservoir drawdown and increased landslide movement. For example, it was observed that GPS unit 176 increased from an average displacement rate of roughly 41 mm/yr to roughly 320 mm/yr during the 2019 drawdown cycle. With additional years of monitoring, a better understanding of how reservoir drawdown leads to landslide instability would be acquired, as only one complete drawdown cycle has been observed so far.

The ability to continuously record data with high frequency also allowed for a higher precision of measurements once averaging was applied to the GPS data. When averaging is applied to GPS data, the ability to correlate short term movement trends with specific changes in the local environment is lost. In the case of Chin Coulee, the change in the reservoir took place over months, which allowed for the correlation to be observed, but short term loading events would have not been able to be correlated.

Accuracy of individual point readings on Chin Coulee was found to be 2 – 4 mm, larger than the manufacturer specified 1 – 2 mm. This may be in part due to the roughly 1 km distance between the fixed point and the mobile GPS units, which impacts GPS correction factors.

By placing GPS displacements onto the 2D typical stratigraphy, it was observed that GPS displacement patterns matched the expected movement patterns for the proposed compound

failure mechanism. GPS units in the upper region were measured moving downwards and along the back scarp failure plane and GPS units in the toe region were measured moving mostly laterally.

9.2 LiDAR Change Detection

LiDAR change detection on Very Slow, vegetated landslides face issues related to vegetation, which increases the level of detection (LOD), which in turn, makes it more difficult to detect small movements. Using all available resources to reduce and remove vegetation from LiDAR scans is critical for vegetated, Very Slow landslides.

Vegetation is often not fully removed, even when using vegetation classification tools and LiDAR scanner settings. It is important to understand where vegetation is present and what impact it has on change detection results (incorrectly identifying regions as loss or gain).

On Chin Coulee, the minimum achievable LOD using LiDAR was 6 – 8 cm. Due to the slow movement rate, this required a monitoring window of approximately 1 year. Scanning performed under similar ground and vegetation conditions will likely return similar LOD's on other sites. It is recommended that a reasonable monitoring window be determined using an estimated LOD of 6 – 8 cm before beginning a monitoring campaign. This will reduce the unnecessary frequency of scanning.

Comparison of LiDAR data and GPS data showed that LiDAR typically over measured displacements by 12 mm. While significant when displacements are low, this is quite a high consistency between measurement methods, and with larger monitoring windows in slower moving environments, LiDAR and GPS are quite comparable methods of measurement.

9.3 UAV and Air Photo Change Detection

UAV change detection on Very Slow, vegetated landslides face identical issues to LiDAR change detection, however UAV change detection is further hindered due to the inability for photographs to penetrate vegetation. UAV generated models will return a "tree-top" model not a bare earth model. This makes the resulting change detection not representative of the true ground movement in vegetated regions.

Unlike LiDAR point clouds, vegetation classification was not shown to be effective when applied to UAV generated point clouds, meaning there was no way to improve the resulting change detection process in vegetated regions.

In addition, UAV change detection is less accurate than LiDAR change detection. The minimum achievable LOD on Chin Coulee using UAV was 9 cm. This is higher than the LiDAR LOD of 6 cm, resulting in less accurate change detection results. The recorded RMS errors from UAV flights were 0.06 and 0.15 m for the August 2018 and July 2019 flights, respectively. It's possible that with a higher RMS the achievable LOD would be reduced.

The high LOD of the UAV-based change detection should have resulted in no observable movement, based on the recorded GPS displacements. However, large amounts of movement were recorded, with average movements near the toe of 22.6 cm, much higher than that recorded from LiDAR or GPS. It was shown that on average, UAV change detection over measured displacement by an average of 52 mm.

Despite the large over measuring of displacements, the resulting change detection was qualitatively similar to the LiDAR change detection model, with exaggerated movements. Both methods supported the proposed compound failure mechanism and showed expected movement patterns.

Historical air photos were used to extend the monitoring duration and observe the ground changes from before monitoring began on the site. Change detection was completed between a 1982 air photo generated model and a 2019 LiDAR scan. Although the resulting LOD was high at 1 m, the resulting change detection was shown to be quite accurate when compared to the current levels of movement observed on the site.

9.4 Kinematics of the Chin Coulee Landslide

Sensitivity analysis for the permeability of the clay till material suggested that permeability is likely $1x10^{-7}$ m/s or lower, based on the lack of piezometer fluctuations during drawdown periods and the observed changes in groundwater level at various permeabilities. This supports the expected range of permeabilities for clay tills in this region.

Transient drawdown analysis showed that drawdown within the reservoir resulted in a maximum expectable reduction in factor of safety within the landslide of 8%, based on the hypothetical maximum possible drawdown scenario. Observed drawdown scenarios in 2018 and 2019 lead to reductions in landslide factor of safety by 7 and 6% respectively. Increased movements within GPS units also showed that this reduction in factor of safety is directly correlated with increased movement on the landslide.

10.0 Recommendations

Due to the Very Slow nature of the Chin Coulee landslide, continued monitoring would be useful in order to obtain a better understanding of the landslide mechanism and movement levels. LiDAR and UAV monitoring only began to show movement levels above the level of detection after comparisons between the latest scans and flight data on July 30, 2019 and the first scans and flight data on August 23, 2018. Many regions within the LiDAR and UAV change detection showed sparse data as a result of the low level of detection. With continued monitoring, movement would increase, allowing for a better understanding of the current levels of movement throughout the slope. With further monitoring, it is possible that identification of potential block movements within the landslide mass may be possible.

The identification of possible triggers for landslide movement in precipitation and reservoir elevation provide a strong argument for continued monitoring using the GPS system on Chin Coulee. With an additional year or two of GPS monitoring a better understanding of the actual mechanism that initiates increased movement would be possible. As only one full yearly cycle of reservoir drawdown and associated movement has occurred, more confidence regarding the observed behaviors could be gained through additional monitoring.

More in-depth LEM modeling would likely require a more in-depth borehole investigation as AMEC FW's investigation did not analyze soil properties of material within the failure plane or the shale material. Due to the depth of the failure plane and the steepness of the landslide, it would be quite difficult and expensive to perform such an investigation.

If LiDAR monitoring was to continue on Chin Coulee, it would be advisable to install ground control points in stable regions to improve point cloud alignment and improve the LiDAR change detection LOD. Due to the levels of vandalism observed on the site, a method which allows for the control point to be removed when not in use would be advisable.

Monitoring of the slope that is above the road for potential instability would be beneficial for understanding whether additional highway relocation would be necessary. Based on visual inspection of the road and the slope, it appears that this location is stable, but installation of another Geocube may be beneficial to verify this.

References

Abellán, A., M. Jaboyedoff, T. Oppikofer, and J. M. Vilaplana. 2009. "Detection of millimetric deformation using a terrestrial laser scanner: Experiment and application to a rockfall event." *Natural Hazards and Earth System Science.*

Alba, Mario, Luigi Fregonese, Frederico Prandi, Marco Scaioni, and P Valgoi. 2006. "Structural monitoring of a large dam by terrestrial laser scanning." Politecnico di Milano.

Alberta Air Photo Library. 2012. "Flight Index 2012021 - 705." Alberta Environment and Parks.

—. 1950. "Flight Index 2031 - LN 4910 - 115." Alberta Environment and Parks.

—. 1945. "Flight Index A7764 - 6." Alberta Environment and Parks.

—. 1970. "Flight Index AS1052 - 24." Alberta Environment and Parks.

—. 1982. "Flight Index AS2448 - 144." Alberta Environment and Parks.

—. 1993. "Flight Index AS4404 - 85." Alberta Environment and Parks.

—. 1999. "Flight Index AS4955 - 258." Alberta Environment and Parks.

—. 2009. "Flight Index AS5482-188."

—. 1960. "Flight Index YC414 - 52." Alberta Environment and Parks.

Alberta Climate Information Service. 2019. *Current and Historical Alberta Weather Station Data Viewer.* https://agriculture.alberta.ca/acis/alberta-weather-data-viewer.jsp.

AMEC. 2004. "Alberta Transportation - Southern Region Landslide Monitoring - Annual Assessment Report." Geotechnical Risk Management Plan.

AMEC. 2000. "Alberta Transportation - Southern Region Landslide Monitoring - Spring 2000 Assessment Report." Geotechnical Risk Management Plan.

AMEC FW. 2015. "Alberta Transportation - Instrumentation Monitoring Results - Site S5: Highway 36:02 - December 2015 Report." Geotechnical Risk Management Plan.

AMEC. 2009. "South Saskatchewan River Basin in Alberta WATER SUPPLY STUDY." Alberta Agriculture and Rural Development.

—. 2014. "Southern Region Geohazard Assessment - Site S5: Highway 36:02, Chin Coulee - Spring 2014 Instrumentation Monitoring Results."

AMEC. 2011. "Southern Region Geohazard Assessment Program - Site S5 - Chin Coulee, Highway 36:02 - 2011 Annual Inspection Report." Geotechnical Risk Management Plan.

Association of Swiss Road and Traffic Engineers. 1999. "Swiss Standard SN 670 010b." Association of Swiss Road and Traffic Engineers.

Baczynski, Norbert, Neil Bar, Matjaz Mikos, Nicola Casagli, Yueping Yin, and Kyoji Sassa. 2017. "Landslide Monitoring and Management Challenges in Remote Papua New Guineas." Chap. 2 in *Advancing Culture of Living with Landslides: Volume 4 Diversity of Landslide Forms*, by Norbert Baczynski, Neil Bar, Matjaz Mikos, Nicola Casagli, Yueping Yin and Kyoji Sassa, 343-356.

Bailey, Dale A. 1958. "Application of Photogrammetry to Mapping for Highway Location Studies."

Baron, I., R. Supper, E. Winkler, K. Motschka, A. Ahl, M. Carman, and A. Kumelj. 2013. "Airborne geophysical survey of the catastrophic landslide at Stože, Log pod Mangrtom, as a test of an innovative approach for landslide mapping in steep alpine terrains." *Natural Hazards and Earth System Sciences.* Vol. 13. no. 10. 2543-2550.

Brodu, Nicloas, and Dimitri Lague. 2012. "3D terrestrial lidar data classification of complex natural scenes using a multi-scale dimensionality criterion: Applications in geomorphology." *ISPRS Journal of Photogrammetry and Remote Sensing* 68 (1): 121-134.

Cook, Kirsten. 2017. "An evaluation of the effectiveness of low-cost UAVs and structure from motion for geomorphic change detection." *Geomorphology* 278: 195-208.

Cruden, David, and David Varnes. 1996. *Landslide Types and Processes.* 1.

Danzi, Mariella, Giuseppe Di Crescenzo, Massimo Ramondini, and Antonio Santo. 2013. "Use of unmanned aerial vehicles (UAVs) for photogrammetric surveys in rockfall instability studies." *Rendiconti Online Societa Geologica Italiana* 24: 82-85.

Deane, Evan, Renato Macciotta, Michael Hendry, Chris Gräpel, and Roger Skirrow. 2019. "The Use and Limitations of Modern Technologies for Slow, Vegetated Landslide Monitoring - Chin Coulee Landslide." *Geo St. John's 2019.* St. John's, Newfoundland, Canada: Canadian Geotechnical Society.

Eker, Remzi, Abdurrahim Aydın, and Johannes Hübl. 2018. "Unmanned aerial vehicle (UAV)-based monitoring of a landslide: Gallenzerkogel landslide (Ybbs-Lower Austria) case study." *Environmental Monitoring and Assessment* (Springer International Publishing) 190 (1).

ESRI. 2018. *Alberta Base Imagery.* http://www.arcgis.com/home/item.html?id=30e5fe3149c34df1ba922e6f5bbf808f.

Federal Aviation Administration. 2017. "Global Positioning System (GPS) Standard Positioning Service (SPS) Performance Analysis Report Executive Summary." Washington, DC.

Fenton, M.M., E.J. Waters, S.M. Pawley, N. Atkinson, D.J. Utting, and K. Mckay. 2013. "Surficial Geology of Alberta." Alberta Geological Survey.

Fey, Christine, and Volker Wichmann. 2017. "Long-range terrestrial laser scanning for geomorphological change detection in alpine terrain – handling uncertainties." *Earth Surface Processes and Landforms.*

Fiani, M, and N Siani. 2005. "Comparison of terrestrial laser scanners in production of DEMs for Cetara tower." *CIPA XX International Symposium.* Torino.

Freeze, Allan, and John Cherry. 1979. *Groundwater.* 1. Prentice Hall.

Geertsema, Marten, Andrée Blais-Stevens, Eva Kwoll, Brian Menounos, Jeremy G. Venditti, Alain Grenier, and Kelsey Wiebe. 2018. "Sensitive clay landslide detection and

characterization in and around Lakelse Lake, British Columbia, Canada." *Sedimentary Geology* (Elsevier B.V.) 364: 217-227.

Girardeau-Montaut, Daniel. 2019. *CloudCompare.*

Golder and Associates. 1998. "Alberta Transportation - Geotechnical Investigation - Site S5: Highway 36:02 - November 1998 Report." Geotechnical Risk Management Plan.

—. 1999. "Alberta Transportation - Geotechnical Investigation - Site S5: Highway 36:02 - October 1999 Report."

Golder Associates. 2002. *Meridian Dam Preliminary Feasibility Study.* Golder Associates Ltd.

Google Earth. 2015. *Alberta, Canada. S. Alberta MD's and Counties.* https://earth.google.com/web/.

Government of Canada. 2019. *National Air Photo Library.* https://www.nrcan.gc.ca/maps-tools-and-publications/satellite-imagery-and-air-photos/air-photos/national-air-photo-library/9265.

Goyer, G. G., and R. Watson. 1963. "The Laser and its Application to Navigation." *BULLETIN AMERICAN METEOROLOGICAL SOCIETY* 44 (9): 564-570.

Grejner-Brzezinska, Dorota A, Charles Toth, T H Wu, and Abdul Shakoor. 2015. "Probabilistic Use of LiDAR Data to Detect and Characterize Landslides." Ohio State University.

Hendry, Michael T., Renato Macciotta, C. Derek Martin, and Benjamin Reich. 2014. "Effect of Thompson River elevation on velocity and instability of Ripley Slide." *Canadian Geotechnical Journal* (Canadian Science Publishing) 52 (3): 257-267.

Herrera, Gerardo, Juan Carlos García López-Davalillo, Jose Antonio Fernández-Merodo, Marta Béjar-Pizarro, Paolo Allasia, Piernicola Lollino, Giorgio Lollino, et al. 2017. "The Differential Slow Moving Dynamic of a Complex Landslide: Multi-sensor Monitoring." In *Advancing Culture of Living with Landslides*, by Gerardo Herrera, Juan Carlos García López-Davalillo, Jose Antonio Fernández-Merodo, Marta Béjar-Pizarro, Paolo Allasia,

Piernicola Lollino, Giorgio Lollino, et al., 219 - 225. Springer International Publishing AG 2017.

Higgins, Sean. 2004. *Time-of-Flight vs. Phase-Based Laser Scanners: Right Tool for the Job.* https://www.spar3d.com/news/related-new-technologies/time-of-flight-vs-phase-based-laser-scanners-right-tool-for-the-job/.

Hong, Hanh. 2018. "Hanh Hong."

Jaboyedoff, Michel, Thierry Oppikofer, Antonio Abellán, Marc Henri Derron, Alex Loye, Richard Metzger, and Andrea Pedrazzini. 2012. "Use of LIDAR in landslide investigations: A review." *Natural Hazards* 61 (1): 5-28.

Karney, Charles. 2017. *Geographiclib.*

KCB. 2018. "S005 Hwy 36:02 Chin Coulee Slide - Geotechnical Drilling and Instrumentation Installation Report." Geotechnical Risk Management Plan.

Kromer, Ryan A., Emily Rowe, Jean Hutchinson, Matt Lato, and Antonio Abellán. 2018. "Rockfall risk management using a pre-failure deformation database." *Landslides.*

Lague, Dimitri, Nicolas Brodu, and Jérôme Leroux. 2013. "Accurate 3D comparison of complex topography with terrestrial laser scanner : application to the Rangitikei canyon (N-Z)."

Langley, Richard B. 1998. "RTK GPS." *GPS World.* GPS World.

Langley, Richard. 1997. "GPS Receiver System Noise." *GPS World* June: 40-45.

Lato, M, M Diederichs, DJ Hutchinson, and R Harrap. 2009. "Optimization of LiDAR scanning and processing for automated structural evaluation of discontinuities in rockmasses." *nternational Journal of Rock Mechanics and Mining Sciences* 46 (1): 194-199.

Lato, Matt, Ryan A Kromer, and Sarah Gaib. 2016. "Understanding landslide movement and kinematics with airborne lidar." *GeoVancouver.* Vancouver.

Lato, Matthew J. 2010. "GEOTECHNICAL APPLICATIONS OF LIDAR PERTAINING TO GEOMECHANICAL EVALUATION AND HAZARD IDENTIFICATION."

Leica Camera AG. 2019. "Leica ScanStation P50 Specifications."

Lengyel, Bela. 1962. "Lasers: Generation of Light by Simulated Emission." John Wiley & Sons. 22 - 28.

Macciotta, Renato, Jorge Rodriguez, Michael T Hendry, Derek Martin, Tom Edwards, and Trevor Evans. 2017. "The 10-mile Slide North of Lillooet, British Columbia - History, Characteristics and Monitoring." *NASL 2017.* Roanoke, Virginia, USA. 937-948.

Macgougan, Glenn D. 2003. "High Sensitivity GPS Performance Analysis in Degraded Signal Environments." University of Calgary.

Malet, J. P., Olivier Maquaire, and Eric Calais. 2002. "The use of global positioning system techniques for the continuous monitoring of landslides: Application to the Super-Sauze earthflow (Alpes-de-Haute-Provence, France)." *Geomorphology* 43: 33 - 54.

Miles, Robert. 1953. "The Use of Aerial Photos in Engineering Planning."

Morgenstern, N. R., and V. E. Price. 1965. "The Analysis of the Stability of General Slip Surfaces." *Géotechnique* 15 (1): 79-93.

Niethammer, U, Mike James, Sabrina Rothmund, Julien Travelletti, and Manfred Joswig. 2012. "UAV-based remote sensing of the Super-Sauze landslide: Evaluation and results." *Engineering Geology* 128: 2-11.

NovAtel Inc. 2015. *An Introduction to GNSS GPS, GLONASS, BeiDou, Galileo and other Global Navigation Satellite Systems.* 2nd. Calgary: NovAtel Inc.

Office of the Press Secretary. 2000. *STATEMENT BY THE PRESIDENT REGARDING THE UNITED STATES' DECISION TO STOP DEGRADING GLOBAL POSITIONING SYSTEM ACCURACY.* https://clintonwhitehouse3.archives.gov/WH/EOP/OSTP/html/0053_2.html.

Ophelia-Sensors. 2019. April 19. https://ophelia-sensors.com/geocube.

Peppa, Maria V., Jon P. Mills, Phil Moore, Pauline E. Miller, and Jonathan E. Chambers. 2018. "Automated co-registration and calibration in SfM photogrammetry for landslide change

detection." *Earth Surface Processes and Landforms* (John Wiley and Sons Ltd) 44 (1): 287-303.

Pirasteh, Saied, and Jonathan Li. 2017. "Landslides investigations from geoinformatics perspective: quality, challenges, and recommendations." *Geomatics, Natural Hazards and Risk* (Taylor and Francis Ltd.) 8 (2): 448-465.

Pix4D. 2019. *Pix4DMapper.* Pix4D.

Prairie Farm Rehabilitation Administration. 1986. "PFRA 1986 Water Management."

Prior, G.J., B. Hathway, P.M. Glombick, D.I. Pana, C.J. Banks, D.C. Hay, C.L. Schneider, M. Grobe, R. Elgr, and J.A. Weiss. 2013. "Bedrock Geology of Alberta." Alberta Geological Survey.

RIEGL Laser Measurement Systems GmbH. 2019. "Reigl VZ-6000 Specifications."

Rocscience Inc. 2019. *Slide 7.0.* Toronto, Ontario, Canada.

Rodriguez, Jorge, Michael T Hendry, and Renato Macciotta. 2018. "Cost-effective Landslide Monitoring GPS System: Characteristics, Implementation and Results." *Geohazard 7.* Canmore.

Ruban, A. F., R.A. Patrick, and R. Skirrow. 2004. "Approach fill design of north Saskatchewan river bridge." *Geo Quebec 2004.* Quebec City: Canadian Geotechnical Society.

Saint Mary's River Irrigation District. 2019. "Chin Coulee Reservoir Elevation Data."

Sala, Zac, D. Jean Hutchinson, and Rob Harrap. 2019. "Simulation of Fragmental Rockfalls Detected Using Terrestrial Laser Scans from Rock Slopes in South-Central British Columbia, Canada." *Natural Hazards and Earth System Sciences Discussions.*

Sharma, Maneesh, Ginger B. Paige, and Scott N. Miller. 2010. "DEM development from ground-based LiDAR data: A method to remove non-surface objects." *Remote Sensing.*

Siebert, Sebastian, and Jochen Teizer. 2014. "Mobile 3D Mapping for Surveying Earthwork Using an Unmanned Aerial Vehicle (UAV)." *Automation in Construction* (International Association for Automation and Robotics in Construction (IAARC)) 41: 1-14.

Skempton, A. W. 1985. "Residual strength of clays in landslides, folded strata and the laboratory." *Geotechnique* 35 (1): 3-18.

Stantec Consulting Ltd. 2010. "Geotechnical Investigation Bow Ridge Subdivision Phase 3." Calgary, Alberta.

Su, Xueqing. 2005. "Pore Pressure Response and Shear Behavior of Shear Zones in Weak Rocks Near Fort McMurray." University of Alberta.

Sun, Xiaoli. 2013. "Space-Based Lidar Systems." *Conference on Lasers and Electro-Optics (CLEO).* San Jose: IEEE.

SZ DJI Technology Co., Ltd. 2019. "DJI Drone Specifications."

Tagliavini, F., M. Mantovani, G. Marcato, A. Pasuto, and S. Silvano. 2007. "Validation of landslide hazard assessment by means of GPS monitoring technique - A case study in the Dolomites (Eastern Alps, Italy)." *Natural Hazards and Earth System Science* (European Geosciences Union) 7 (1): 185-193.

Takasu, Tomoji, and Akio Yasuda. 2009. "Development of the low-cost RTK-GPS receiver with an open source program package RTKLIB." *International Symposium on GPS/GNSS.* Jeju: IGNSS.

Teledyne Optech. 2019. *ILRIS-LR Terrestrial Laser Scanner Summary Specification Sheet.* http://info.teledyneoptech.com/acton/attachment/19958/f-02ea/1/-/-/-/-/ILRIS-LR-Spec-Sheet_LR.pdf.

—. 2019. "Teledyne Optech Polaris LR Specifications."

Teza, G, A Galgaro, N Zaltron, and R Genevois. 2007. "Terrestrial laser scanner to detect landslide displacement fields: a new approach." *International Journal of Remote Sensing* 28 (16): 3425–3446.

The MathWorks Inc. 2019. *MATLAB.*

United States Department of Agriculture. 2019. *USDA Soil Texture Calculator.* https://www.nrcs.usda.gov/wps/portal/nrcs/detail/soils/survey/?cid=nrcs142p2_054167.

Updike, Randall. 1983. "SURVEY-MONITORING SYSTEM, PILLAR MOUNTAIN LANDSLIDE AREA, KODIAK, ALASKA." 1.

Wang, Guoquan. 2011. "GPS Landslide Monitoring: Single Base vs. Network Solutions — A case study based on the Puerto Rico and Virgin Islands Permanent GPS Network." *Journal of Geodetic Science* (Walter de Gruyter GmbH) 1 (3).

Xiong, Lin, Guoquan Wang, Yan Bao, Xin Zhou, Xiaohan Sun, and Ruibin Zhao. 2018. "Detectability of Repeated Airborne Laser Scanning for Mountain Landslide Monitoring." *Geosciences* (MDPI AG) 8 (12): 469.

Yuneec International. 2019. "Yuneec Drone Specifications."

Zhang, Wuming, Jianbo Qi, Peng Wan, Hongtao Wang, Donghui Xie, Xiaoyan Wang, and Guangjian Yan. 2016. "An easy-to-use airborne LiDAR data filtering method based on cloth simulation." *Remote Sensing* (MDPI AG) 8 (6).